

Journal of Visualized Experiments

Quantifying Intermembrane Distances with Serial Image Dilations in Matlab

--Manuscript Draft--

Article Type:	Methods Article - JoVE Produced Video
Manuscript Number:	JoVE58311R2
Full Title:	Quantifying Intermembrane Distances with Serial Image Dilations in Matlab
Keywords:	Matlab, perinexus; image processing; intermembrane space; Atrial Fibrillation; ephaptic coupling
Corresponding Author:	Steven Poelzing Virginia Tech Roanoke, VA UNITED STATES
Corresponding Author's Institution:	Virginia Tech
Corresponding Author E-Mail:	poelzing@vtc.vt.edu
Order of Authors:	Tristan Raisch Momina Khan Steven Poelzing
Additional Information:	
Question	Response
Please indicate whether this article will be Standard Access or Open Access.	Standard Access (US\$2,400)
Please indicate the city, state/province, and country where this article will be filmed . Please do not use abbreviations.	2 Riverside Circle Roanoke, VA 24016

TITLE:**Quantifying Intermembrane Distances with Serial Image Dilations****AUTHORS & AFFILIATIONS:**

Tristan Raisch^{1,2}, Momina Khan¹, Steve Poelzing^{1,2}

¹Virginia Tech Carilion Research Institute, Virginia Tech, Blacksburg, Virginia, United States

²Translational Biology, Medicine and Health, Virginia Tech, Blacksburg, Virginia, United States

CORRESPONDING AUTHOR:

Steve Poelzing (poelzing@vtc.vt.edu)

EMAIL ADDRESSES OF CO-AUTHORS:

Tristan Raisch (tristanr@vt.edu)

Momina Khan (momina1@vt.edu)

KEYWORDS:

Perinexus, image processing, intermembrane space, atrial fibrillation, ephaptic coupling, serial image dilation, pathfinding

SUMMARY:

The purpose of this algorithm is to continuously measure the distance between two 2-dimensional edges using serial image dilations and pathfinding. This algorithm can be applied to a variety of fields such as cardiac structural biology, vascular biology, and civil engineering.

ABSTRACT:

A recently-described extracellular nanodomain, termed the perinexus, has been implicated in ephaptic coupling, which is an alternative mechanism for electrical conduction between cardiomyocytes. The current method for quantifying this space by manual segmentation is slow and has low spatial resolution. We developed an algorithm that uses serial image dilations of a binary outline to count the number of pixels between two opposing 2 dimensional edges. This algorithm requires fewer man hours and has a higher spatial resolution than the manual method while preserving the reproducibility of the manual process. In fact, experienced and novice investigators were able to recapitulate the results of a previous study with this new algorithm. The algorithm is limited by the human input needed to manually outline the perinexus and computational power mainly encumbered by a pre-existing pathfinding algorithm. However, the algorithm's high-throughput capabilities, high spatial resolution and reproducibility make it a versatile and robust measurement tool for use across a variety of applications requiring the measurement of the distance between any 2-dimensional (2D) edges.

INTRODUCTION:

The following algorithm was developed to measure the intermembrane distance between two structurally coupled cardiomyocytes at the point they separate from each other at the edge of a gap junction plaque in a nanodomain called the perinexus¹, which has been implicated in ephaptic coupling²⁻⁵. In the process of analyzing hundreds of transmission electron microscopy

(TEM) images of perinexi using a manual segmentation method in a previous study⁶, the need was identified for a higher-throughput method that sampled perinexal width in higher spatial resolution while preserving the accuracy of the previous manual segmentation process. During manual segmentation, lines are drawn at 15 nm intervals, approximately orthogonal to the centerline, in order to measure perinexal width. The new algorithm takes a one pixel thick binary outline of two parallel lines and uses serial image dilations to count the number of pixels between the two membranes. While image dilations have commonly been used in a myriad of image processing applications, including contour or edge detection^{7,8}, this algorithm uses dilations as a counting mechanism. The centerline is then isolated using a pathfinding algorithm⁹ and perinexal width is then measured at a resolution along the length of perinexus equal to the resolution of the image. The difference in resolution in this case is 1 measurement per 15 nm for manual segmentation and 1 measurement per 0.34 nm with the new algorithm, a 44-fold increase in spatial sampling frequency. Furthermore, this increased sampling frequency is accomplished in approximately 1/5th the time needed for manual segmentation.

This algorithm will be used in its current form to measure perinexal width at the conventional 0-150 nm from the edge of a gap junction plaque⁵ (GJ) as well as within a specified region of interest, where the perinexus plateaus between 30 and 105 nm^{2,3,10}. The increased sampling frequency reduces the variability in individual perinexus measurements compared to manual segmentation and significantly shortens analysis time, allowing for efficient processing of large data sets. However, this program is not limited to nanoscale TEM images of cardiac intercalated disks. The same approach could be used to quantify vascular diameter, ventricular ejection fraction, or even non-biological phenomena such as river erosion or flooding. This algorithm is appropriate for quantifying the distance between any two quasi-parallel edges.

PROTOCOL:

Note: Software required are ImageJ (or similar image-modifying software) and Matlab R2015. The user may encounter compatibility issues with other versions of Matlab.

1. Pre-Processing Images

1.1. For any grayscale image, ensure the maximum intensity value of any given pixel is <255. This is typically done by subtracting a value of 1 from the image in the custom Matlab program "ImageSub.m", included in supplemental file S1.

2. Outlining the Perinexus

2.1. Outline the perinexus in ImageJ or other image-processing software.

2.2. Ensure that the outline is one pixel thick and is set to the highest intensity value in an image (255 in a grayscale image from 0 to 255).

2.3. Identify the GJ by its pentalaminar structure^{11,12}, and define the beginning of the perinexus

as the point at which the two opposing cell membrane bilayers diverge, as shown in **Figure 1A**. Begin ~200 nm from the edge of the GJ, tracing along the inner membrane of the first cell and back along the inner membrane of the second cell. In ImageJ, release the pen to automatically close the outline. This artificial closing will be cropped out later.

Note: It is crucial to outline the perinexus with great care at as high a magnification as possible, as even small mis-applications of the outline can result in several nanometers of error in the final measurement.

3. Setting up Algorithm and Selecting Perinexus of Interest

Note: The pathfinding algorithm requires the AutoGraph, Edge, Graph, Node , and Pathfinding functions⁹ to be in the same directory as the MembraneSepDist m-file. All files can be found in supplemental file S1.

3.1. Select save locations for data and figures. These are currently hard-coded into the m-file.

Note: The first line of the program is a function to clear all variables, close all windows and clear the command window. Save any desired variables or figures before running the m-file.

Note: Software screenshots are included in supplemental file S2 for all hard-coded values.

3.2. Run the program “MembraneSepDist.m”.

3.3. Set Parameters.

Note: A GUI will pop up with default parameters for the gradient threshold, scale, region of interest, and manual start. The default values can be changed in the m-file, or they can be changed for each individual image.

3.3.1. Set spatial derivative gradient threshold.

Note: Higher values result in more points selected in centerline isolation. Values that are too high or too low (outside of a range of approximately 3.0-7.9) may result in computational inefficiency or an imprecise selection of centerline points yielding imprecise centerline isolation (See **Figure 2A-C**).

3.3.2. Set scale in pixels/scale units.

3.3.3. Set the spatial lower and upper limits for the region of interest.

Note: By our laboratory’s convention, the defined region of interest is between 30 and 105 nm from the edge of the GJ^{2,3,10}.

3.3.4. Set automatic/manual start. In the majority of cases, the algorithm accurately detects the starting point where the gap junction ends and perinexus begins. However, in some cases of irregularly-shaped perinexi, the user must identify the start point manually. Set this value to 0 for automatic, 1 for manual.

3.4. Select desired image.

Note: The file select folder can be changed in the m-file.

3.5. Crop the image to select the perinexus of interest.

3.5.1. When the image comes up, the cursor will automatically change to a crosshair. Crop the image by dragging a box around the perinexus of interest (See **Figure 3**). The crop box can be adjusted by using the squares on the corners and sides to make it larger or smaller.

3.5.2. When cropping, ensure the “open” end of the perinexus (furthest from the GJ, see **Figure 3**) is cropped so that the two membrane outlines reach the edge of the cropped image.

Note: It is recommended to make the image full-screen to more easily see the perinexus of interest and crop appropriately.

3.6. Select the final crop by double-clicking with the cursor in between the opposing edges to be measured.

Note: It is critical that the double-click be performed inside the perinexus. If the program fails to identify a centerline, restart the program and make sure the click occurs within the perinexus.

3.7. Observe the final centerline after all dilations and erosions pop up for a final user evaluation of the program’s efficacy.

Note: A dialog box will appear on the screen while the program is running to inform the user that Matlab will be unable to process any additional commands until the program has finished. How long this process takes depends on array (image) size and computer processing power.

3.8. If manual start point is enabled, observe the image of the centerline pop up over the original anatomical image, along with a cross-hair cursor (see **Figure 2E**). Select a point outside of the perinexus near the desired start point.

Note: The program will find the centerline point closest to the selected pixel and use that as the start point.

3.9. Record data.

Note: Once the program has finished, the program will return a mapped centerline, plot of

perinexal width as a function of distance from the edge of the GJ. Additionally, the program will return the average perinexal width up to 150 nm from the edge of the GJ as well as the average from within the defined region of interest at the Matlab command line. W_p values and distances from the GJ are stored in the variable “WpList” or the user can manually record them separately.

4. Algorithm Troubleshooting

4.1. If the centerline is not properly identified (**Figure 2A**), open the figure “Gmag” and use the Index to identify an appropriate gradient threshold (**Figure 2C**).

4.2. If the start point is not properly identified, set the start point manually (See Protocol 3.8).

REPRESENTATIVE RESULTS:

Statistical Methods: Comparisons were made between experimental groups using Student’s t-tests. A p-value < 0.05 is considered significant and all values are represented as mean \pm standard deviation.

Manual Segmentation. The quantification of the GJ-adjacent perinexus nanodomain width (W_p) is typically accomplished by manual segmentation. This manual segmentation process is demonstrated in **Figure 1A** and was described previously⁶. The observer identifies the edge of the GJ (**Figure 1**, red dot), measures 5nm along the center of the perinexus, and measures the distance between the membranes at that point. The process is then repeated at 10, 15, 30, and every 15 nm up to 150 nm. This technique, while effective, has limitations of time and spatial under-sampling along the length of the perinexus.

Mean W_p measurements from previous studies can vary from approximately 10 to 20 nm^{2,3,10}, and 3 nm appears to be the mean difference needed to detect statistical significance, which is well above the spatial Nyquist frequency of 0.7 nm per measurement based on an interpixel resolution of 0.34 nm. Therefore, while manual segmentation is time consuming, the method is sufficient to measure differences in W_p associated with an intervention or disease state.

Serial Image Dilations. In order to measure the perinexus in a faster, reproducible manner with appropriate spatial resolution, we developed a program based on serial image dilations to count the pixels between two manually-traced membranes, which can be seen in **Figure 1B**.

The serial dilation process is illustrated in **Figure 4**. As the binary image is dilated (**Figures 4A-4D**), that dilation is then inverted and added to a working image – the non-binary form of the original outline (**Figures 4E-4H**). The process is repeated until the outline is entirely filled in (**Figure 4D**). At this point, the final working image (**Figure 4H**) is a count of the number of times a particular pixel has remained un-dilated. As such, the values near the outline of the cell membranes are very low, while the values at the center are highest. By counting the number of dilations to fill the area at each point, the distance between the membrane edges can be calculated. The next challenge is to identify and isolate the centerline in order to quantify perinexal width as a function of distance from the GJ, which is done by first applying a spatial derivative to the final working

image (**Figure 2**-last image, and **Figure 5A**). A second example of a more irregularly-shaped perinexus can be found in supplemental file S3.

Centerline Identification. The gradient of the final working image can be quantified by a spatial derivative, as dilation count values from edge to edge change from high to low to high again (**Figure 5A** left to right). Considering only the magnitude of the spatial derivative (**Figure 5B**), the outline and centerline, highlighted with white arrows, are immediately identifiable as areas of discontinuity. At these locations, the gradient direction changes from increasing to decreasing or vice versa. Applying a threshold (**Figure 5C**) produces a binary image of the centerline and outline, and subtracting the original outline yields the isolated centerline (**Figure 5D**). While this method of isolating the centerline is computationally efficient, the threshold applied to the spatial derivative creates gaps in the resulting centerline. These gaps (**Figure 5D**, insert) must be filled to provide an accurate measurement of the distance from the GJ and to ensure the perinexus is measured in its entirety. First, the centerline is dilated to fill in any gaps (**Figure 5E**), followed by an erosion (**Figure 5F**) and a “bwmorph” function (operation = ‘skel’, n = inf) to eliminate as many points as possible while leaving a continuous centerline, thereby increasing the computational efficiency of a subsequent pathfinding algorithm developed by Wasit Limprasert and available on MATLAB Central⁹. This dilation-erosion function produces the completed centerline, which is combined with the final working image (**Figure 5G**). However, this centerline is often more than one pixel thick and therefore is not a precise isolation of the centerline.

The Wasit Limprasert pathfinding algorithm is used to determine the perinexus centerline. The pathfinding algorithm is able to track the highest values – in this case the values closest to the center which remained un-dilated through the most iterations along the centerline (**Figure 5G**, insert). The result is an automatic trace of the centerline, as shown in **Figure 6**. By isolating the centerline, perinexal width can be presented as a function of distance from the end of the GJ, as shown in **Figure 6B** (top), or as the average width of a specified region of interest.

Kernel Analysis. It is important to note that digitized images are based on square arrays and dilation kernels are likewise based on square matrices. This means that dilation distance across a diagonal is greater than orthogonal. Therefore, we next sought to determine whether the kernel affected the results of the algorithm. In order to quantify kernel-specific variability, five different kernel shapes were analyzed: “Plus” (the shape used in the above analyses), “X”, “Box”, and “Line”, as described in **Figure 7A**. The kernel is applied at each non-zero point of a binary image. The star in each kernel of **Figure 7A** represents the center, where white is a value of 1, and black is a value of 0 for the dilation kernel.

Each kernel’s influence on the mean W_p measurement of a single approximately horizontal perinexal image (**Figure 7B**, top), quantified by an experienced user, was determined by rotating the image with Matlab’s “imrotate” command and computing W_p in steps of 10° . The W_p measurement values (**Figure 7B**, bottom) fluctuate with image orientation in a rectified sinusoidal fashion with a Plus shaped kernel. The lowest values occur when a relatively straight perinexus is oriented vertically or horizontally. Neither the X, Box, nor Line kernels provided any advantage over the plus-shaped kernel. The X and Box kernels produced identical results, but the

values of mean W_p were out of phase with the *Plus* kernel by 45°. The *Line* kernel failed to fully dilate the image at certain angles as can be seen by the absence of data in the green trace for images rotated less than 30 or more than 145°. Thus, the orthogonal *Plus* dilation kernel overestimated membrane separation when dilating a perinexus with an axis oriented diagonally for example at approximately 45°, and the *X* and *Box* kernels underestimated mean W_p when the long axis of the perinexus was also at 45°. Based on this analysis, we developed a correction factor applied to the values generated from dilating with the plus-shaped kernel. To account for the overestimation of membrane separation associated with image orientation, this correction factor multiplied by the measured width value depending on the orientation of the image (Equation 1).

If $\theta < 45^\circ$

$$W_{p \text{ corrected}} = \cos(\theta) * W_{p \text{ measured}}$$

If $\theta \geq 45^\circ$

$$W_{p \text{ corrected}} = \sin(\theta) * W_{p \text{ measured}} \quad (\text{Equation 1})$$

In this equation, W_p measured is the original W_p value generated by the above algorithm and θ is the calculated angle from horizontal, in degrees. θ is calculated by taking the inverse tangent of the total change in the horizontal direction divided by the total change in the vertical direction of the perinexal centerline. The above correction approximates the average angle, relative to horizontal, of the perinexus (**Figure 8A**, left-top) and results in a measurement as if obtained from a horizontal perinexus (**Figure 8A**, left-bottom). The rationale behind this equation comes from the fact that the plus-shaped kernel (**Figure 7A**) is essentially two line-shaped kernels arranged orthogonally to each other. As such, below 45° (closer to horizontal), the dilations occur vertically and therefore multiplying by the cosine of the angle gives the correct measurement. Conversely, for angles above 45° (closer to vertical), dilations occur horizontally and the sine is used to determine the correct measurement. At precisely 45°, the sine and cosine are equal. Supplemental file S4 provides a depiction of this concept. Note that this correction is based on the average angle and caution should be used when analyzing substantially non-linear shapes. This process was repeated on 20 randomly-selected perinexi and the corrected measurements correlated strongly with measurements obtained by manually rotating and re-analyzing the images (**Figure 8A**, right). To confirm the accurate correction for image orientation, two sets of phantom edges were generated (**Figure 8B**, left) and rotated 180°. With the trigonometric correction, the algorithm accurately returned the correct value at each orientation, regardless of spatial resolution or image size (**Figure 8B**, right).

Analytical Application and Reproducibility with Orientation Correction. Recalling that previous studies using manual segmentation report statistically significant mean W_p differences greater than or equal to 3 nm, it was important to determine whether the algorithm could be used to recapitulate previous findings using a complete dataset. Using the new algorithm, two observers – one experienced and one unexperienced with perinexal analysis (Obs. 1 and Obs.2, respectively) – analyzed the same images from a previous study⁶ that included 12 patients who were diagnosed with atrial fibrillation (AF) prior to tissue collection and 29 patients that did not have pre-existing AF (No-AF). The experienced user found that W_p was significantly wider in patients with AF than without AF (21.9±2.5 and 18.4±2.0 nm, respectively, **Figure 9A**). These

values with the correction factor applied are similar to those reported previously (24.4 ± 2.2 nm and 20.7 ± 2.4 nm, respectively)⁶. Importantly, the inexperienced user found the same significant difference (22.1 ± 2.8 nm and 20.1 ± 2.6 nm, respectively) between disease states with the automated program. Additionally, the standard deviation of the W_p values did not change with the correction factor, indicating the standard deviation of 2-3 nm is not an artifact of the algorithm but of the structure itself and tissue processing. These results demonstrate that the proposed automated method is capable of recapitulating the results of previous studies.

Importantly, the perinexus is a recently-defined structure and no consensus has been reached on the range of absolute values of membrane separation adjacent to the GJ^{2,3}. Since outer-membrane-to-outer-membrane GJ width has been previously estimated at 20 nm¹³, we sought to determine the algorithm's efficacy by also measuring GJ width. Both observers found no significant difference between gap junction widths (GJW) of patients with or without pre-existing AF (**Figure 9B**). Absolute GJW values for AF and non-AF patients were 20.5 ± 2.5 nm and 20.3 ± 1.9 nm, respectively, for the experienced observer and 21.0 ± 3.1 nm and 20.0 ± 2.2 nm for the inexperienced observer, similar to what has been reported previously.

To determine whether the automated algorithm required less time to analyze data than manual segmentation, both the experienced and inexperienced user recorded the time needed to quantify a 10-image training set (Supplemental file S5). **Table 1** demonstrates that the experienced and inexperienced user decreased analysis time by 4.7- and 8.3-fold respectively using the automated algorithm relative to the manual segmentation approach, with an approximately 43-fold increase in spatial resolution along the perinexus.

Algorithm Troubleshooting. The most common error when running the algorithm occurs when the final centerline does not end at the edge of the image. In such cases, not enough points were selected from the spatial derivative map, causing the program to fail and produce an error message advising the user to select a larger crop area or increase the spatial derivative threshold. Drawing a larger crop box will improve the reliability of the program in some cases as the spatial derivative changes drastically near the edges of the figure, which can disrupt the pathfinding or edge detection algorithms.

It is also possible for the pathfinding algorithm to fail to properly identify the centerline, even if the centerline reaches the edge of the image, particularly if the gradient threshold is too low (**Figure 2A**). If the gradient threshold is set too high, there will be more unnecessary points incorporated into the pathfinding algorithm (**Figure 2B**), decreasing computational efficiency. If the user is unable to determine an appropriate threshold, the image array "*GMag*" (**Figure 2C**), which is generated by the program and can be found in the Workspace, can help the user determine the threshold. Find points along the centerline and set the threshold slightly above their Index value to ensure these points are selected. In the given example, an appropriate threshold would be above ~ 5.1 (**Figure 2C**, insert).

The start point may also fail to reach the beginning of the perinexus (**Figure 2D**). In this case, re-run the program and set the *Manual Start* value to 1. After the centerline has been isolated, the

user selects a point outside the perinexus and the centerline point closest to the selected pixel (Figure 2E, red square) will be set as the start point. The result is the full centerline (Figure 2F).

FIGURE AND TABLE LEGENDS:

Figure 1: TEM images with quantification processes. The manual segmentation process (A) requires the user to perform 12 individual intermembrane measurements while estimating the centerline. The automatic process (B) requires a manual, continuous trace of the outline of the perinexus. The red dot in each image represents the user-identified end of the GJ and the beginning of the perinexus.

Figure 2: Centerline troubleshooting. Two primary modes of failure for the centerline identification and their solutions: Each image is labelled with the array name in Matlab. If the gradient threshold is too low (A, threshold 0.2) the centerline algorithm can fail. Setting the threshold too high (B, threshold 70) can reduce the computational efficiency of the pathfinding algorithm. An appropriate gradient threshold can be determined from the GMag array (C, insert). If the centerline fails to reach the beginning edge of the perinexus (D), the user can opt to manually select the start point. After the “Start Point” option is set to 1 in the opening GUI, the user then selects a point *outside* the perinexus of interest (E). The end result should be a centerline that accurately depicts the entirety of the perinexus (F). All labels in quotations (A-F) correspond to the variable names in Matlab.

Figure 3: Perinexus Selection. To crop the perinexus, click-and-hold to drag a box around it (the crop tool is selected automatically) as shown by the blue arrow. This box can be adjusted by using the squares on the sides and corners to make it larger or smaller. The green arrow represents the end of the perinexus, which the user should ensure remains “open.”

Figure 4: Serial image dilations. The binary outline is repeatedly dilated in one-pixel increments (A-D) and added to the working image (the non-binary form of the image, E-H) after each dilation.

Figure 5: Centerline isolation and pathfinding. A spatial derivative is calculated from the final working image (A) and the magnitude of that spatial derivative (B) is used to isolate the outline and centerline (white arrows). A user-defined threshold identifies the outline and centerline and subtracting the original outline yields the centerline (D). However, gaps appear in the centerline as a result of the threshold (D – insert). In order to produce a continuous centerline, a secondary dilation is performed on the isolated centerline (E), followed by a secondary erosion to increase the computational efficiency of a subsequent pathfinding algorithm. This eroded image (F) is then combined with the final working image, allowing for the identification of a continuous, one-pixel-thick centerline (G – insert).

Figure 6: Final data presentation. The program outputs the final outline on top of the original TEM image (A). The line is color-coded green for 0-150 nm, blue for the user-defined region of interest and red for the area beyond 150 nm. Additionally, the program outputs a similarly color-coded chart representing W_p as a function of distance from the start of the perinexus and for the region of interest (B), as well as the average W_p (inset in respective graph).

Figure 7: Dilation kernel shape analysis. Shapes for dilation kernels (A): the star in the middle represents the dilated pixels. White boxes are pixels affected by the dilation, in the shape of a plus, X, box or line. An approximately horizontal perinexus (B, top, with a red line indicating 0°) was rotated clockwise from 0 to 180° in steps of 10° and repeatedly dilated using the different kernel shapes (B, bottom). Plus- and line-shaped kernels produce similar results, although the line kernel fails at certain orientations, while the box- and X-shaped kernels are out of phase by 45°.

Figure 8: Image Orientation Correction. To correct for the orientation of the image, the average angle of the perinexus is calculated from the positions of the start- and end-points (A, left, beginning and end of black line). The inverse tangent of the change in the y-direction (A, left, green line) divided by the change in the x-direction (A, left, red line) yields the correction angle, θ (A, left, yellow). The goal is to then correct the average W_p value to give the minimum distance between the edges, as if the perinexus had been imaged approximately horizontally (A, left below). The application of the correction factor described by Equation 1 was compared to manually rotating each of 15 randomly-selected images by the calculated θ before analysis. The corrected values strongly correlated with the rotated-image values ($R^2 = 0.991$, A, Right), indicating Equation 1 is a valid correction factor for image orientation. To confirm the correction factor is appropriate, two phantoms were generated of perfectly-parallel edges with a known distance between them (B, Left). Phantom 1 and Phantom 2 have spatial resolutions of 2.833 pixels/mm. and 71.6 pixels/in., respectively. As shown by the blue diamonds and red squares in B, Right, the algorithm accurately calculates their widths across 180 degrees of image rotation.

Figure 9: Algorithm reproducibility. Using the automatic process with image orientation correction, both an experienced and inexperienced observer found significant differences between AF and No-AF groups (A), consistent with a previous study, detecting a minimum difference of 2.6 nm. Additionally, neither observer found a significant difference in GJW (B).

Table 1: Comparison of manual and automatic processes. Both observers required less time per image to trace the outline than to perform the manual segmentation process for a 10-image training set. Additionally, the automatic process has a higher sampling frequency, recording 3.45 measurements per nm, compared to an average of 1 measurement every 12.5 nm for the manual process. The training set images can be found in Supplemental File S5, along with outlines and measurements as performed by an experienced user.

DISCUSSION:

The algorithm uses serial image dilations to count the number of pixels between two opposing 2D edges in a binary image, which in this case is the inter-membrane separation of the perinexus^{2,3,14}. A spatial derivative and a pathfinding algorithm are then used to isolate the centerline, followed by a secondary dilation and erosion sequence to fill gaps in the centerline, similar to what has been done before¹⁵. The centerline is then combined with the final dilation-count image to represent perinexal width as a function of distance from the beginning of edge separation, in this case the end of the GJ and the beginning of the perinexus¹⁶.

Four primary parameters are user-defined in a GUI at the start of the program:

1. Gradient threshold
2. Scale
3. Region of interest range
4. Start point selection method (automatic or manual)

The most common mechanism of failure for the algorithm is the failure of the centerline to reach the edge of the image, which is how the endpoint is determined for the pathfinding algorithm. In order to fix such an issue, the user can increase the gradient threshold described in step 3.3.1, which will cause the program to select more points out of the spatial derivative image, which will increase the computation time required by the pathfinding algorithm. Therefore, this algorithm requires a compromise between computation speed and centerline integrity. It is important to note that so long as all the points of the centerline are identified from the spatial derivative, along with an appropriate start point, the spatial derivative threshold will have no effect on the edge separation measurement.

Image orientation appears to affect dilation values, because the kernel dilates in 90 degree steps, which can introduce an error if the majority of the region of interest is at an angle 45° to the axes of dilation matrices. Therefore, the dilation count may not always be an accurate representation of the space between the edges. This limitation has been addressed by a trigonometric correction factor, but could potentially be ignored if all images in a dataset are aligned at the same orientation. Furthermore, caution should be used in interpreting results, as it is possible that section planes are not perfectly perpendicular to the two membranes. In **Figure 9B**, we use GJW to suggest that our perinexus images were in-plane. Still, it is imperative that sample sizes be sufficiently large to account for any sectioning variations between images. Additionally, our perinexal width measurements should not be interpreted to reflect *in vivo* spaces, but this approach is used to measure mean differences in perinexal width relative to some intervention or disease state.

The current algorithm also requires a manually-traced outline of the edges as an input. It is important to note that so long as the scale is set correctly, spatial resolution has no effect on the algorithm's measurements, as demonstrated by the varying resolutions of images in **Figure 6** and an additional low-resolution image in supplemental file S6. The next step in improving the algorithm is removing human intervention from outline generation along with a tool that can select the area of interest. These features would likely enhance the precision of the measurement and reduce user bias.

This computationally efficient algorithm provides a faster method, requiring approximately one fifth the man-hours, of quantifying the perinexus with no detectable penalty to reproducibility when compared to the manual segmentation process. Additionally, the manual segmentation process utilizes one measurement every 15 nanometers to quantify perinexal width, which can lead to under sampling as the membrane separation of the perinexus can change substantially within that 15 nm range. In contrast, the automated program has a spatial resolution equal to

that of the imaging modality, in this case 2.9 pixels per nanometer along the length of the perinexus, therefore delivering a more finely resolved average of perinexal width.

While the applications in the field of cardiac structural biology are promising and exciting, this algorithm's uses are not confined to TEM images. Any field requiring a precise, high-resolution measurement of two quasi-parallel 2D edges can make use of this algorithm. The algorithm could be used to track anything from riverbank erosion and flood patterns from satellite images to vascular development with brightfield or fluorescent microscopy. One of the most promising potential applications is in the field of cardiology and measuring ventricular ejection fraction (EF) with point-of-care cardiac echocardiography. Currently, the standard technique is the biplane method of disks¹⁷, though a newer algorithm, AutoEF, is currently the cutting edge EF-quantifying method^{18,19}. For biplane method of disks, the chamber in question is manually traced and quantified using a modified Simpson's method, whereby overall volume is automatically calculated by the summation of stacked elliptical disks. The main limitation with this method is that it can only return the total cross-sectional area of the desired chamber, with no resolution to identify specific regions of interest, and also requires substantial human input and expertise. The newer method, AutoEF, identifies and outlines the edge of the ventricle using a 2D speckling algorithm and then computes the ventricular cross-sectional area. This process, while precise and efficient for measuring gross ventricular area, also has a similar inherent limitation of only measuring total cross-sectional area. This primary drawback limits clinicians' diagnostic and treatment abilities. In contrast, the algorithm presented in this manuscript can identify a midline and has a resolution equal to the resolution of the imaging modality to pinpoint specific regions of interest. This is important because ultrasound scanners with micrometer spatial resolution are commercially available^{20,21}, implying that this algorithm could detect localized wall motion abnormalities at the resolution of micrometers instead of centimeters. While this application needs to be experimentally validated, it is one of the most immediately promising applications of this algorithm. In fact, it could easily be combined with the speckle tracking capabilities of AutoEF or the manual traces utilized in manual planimetry to provide higher-resolution information in parallel with conventional EF data.

As versatile and applicable as the current algorithm is, it was developed for 2D images. However, as imaging technologies continue to improve, there is an increasing demand for 3 and 4D quantification technologies. Therefore, the next iteration of the algorithm is to adapt the same approach, serially dilating a binary image, to a 3-dimensional object, where automatically defining a centerline is currently beyond the capabilities of current imaging programs. Such an algorithm would have wide applications both clinically and experimentally in the cardiac field alone, including 3D cardiac echocardiograms^{22,23}, 3D electron microscopy²⁴⁻²⁶, and 3D magnetic resonance imaging²⁷⁻²⁹.

ACKNOWLEDGMENTS:

The authors would like to thank Kathy Lowe at the Virginia-Maryland College of Veterinary Medicine for processing and staining TEM samples.

Funding:

National Institutes of Health R01-HL102298

National Institutes of Health F31-HL140873-01

DISCLOSURES:

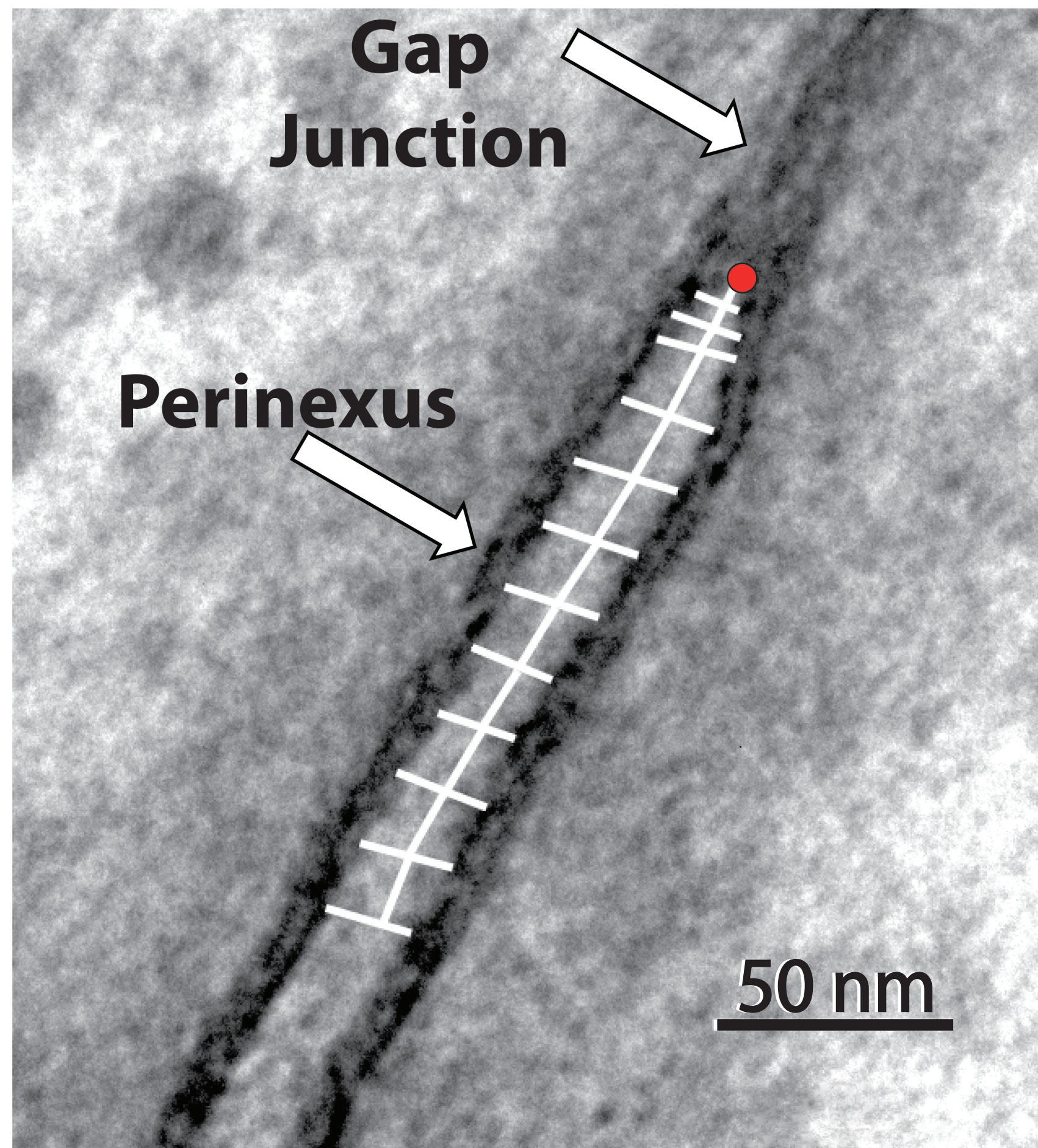
The authors have nothing to disclose.

REFERENCES:

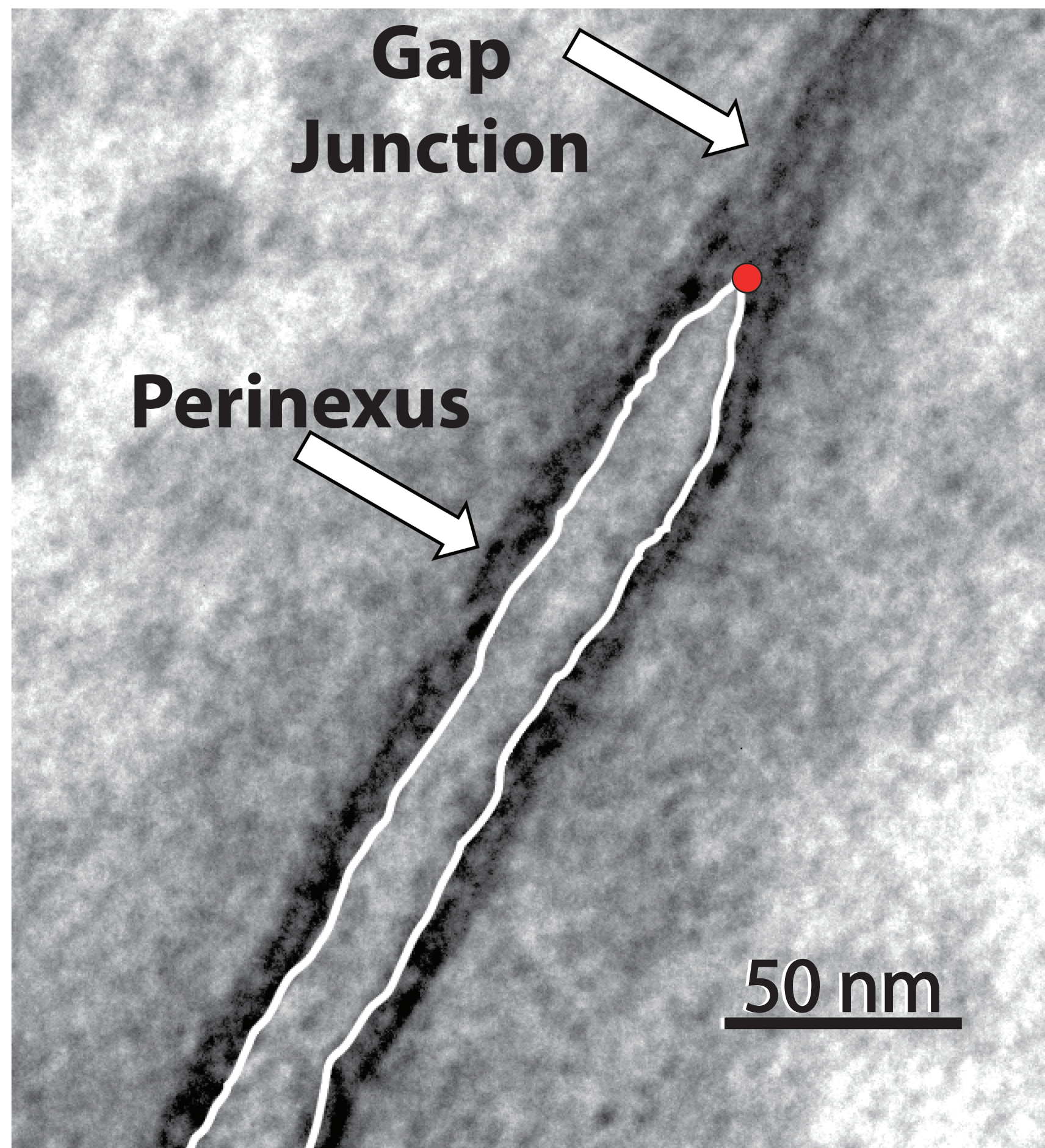
1. Rhett, J.M. and R.G. Gourdie, The perinexus: a new feature of Cx43 gap junction organization. *Heart Rhythm* **9** (4), 619-23 (2012).
2. Veeraghavan, R., *et al.* Sodium channels in the Cx43 gap junction perinexus may constitute a cardiac ephapse: an experimental and modeling study. *Pflugers Archiv: European Journal of Physiology* (2015).
3. George, S.A., *et al.* Extracellular sodium dependence of the conduction velocity-calcium relationship: evidence of ephaptic self-attenuation. *American Journal of Physiology - Heart and Circulatory Physiology* **310** (9), H1129-39 (2016).
4. Veeraghavan, R., *et al.* Potassium channels in the Cx43 gap junction perinexus modulate ephaptic coupling: an experimental and modeling study. *Pflugers Archiv: European Journal of Physiology* (2016).
5. Rhett, J.M., *et al.* Cx43 associates with Na(v)1.5 in the cardiomyocyte perinexus. *Journal of Membrane Biology* **245** (7), 411-22 (2012).
6. Raisch, T.B., *et al.* Intercalated Disc Extracellular Nanodomain Expansion in Patients with Atrial Fibrillation. *Frontiers in Physiology* (2018).
7. Yan, J., *et al.* Novel methods of automated quantification of gap junction distribution and interstitial collagen quantity from animal and human atrial tissue sections. *PLoS One* **9** (8), e104357 (2014).
8. Papari, G. and N. Petkov, Adaptive pseudo dilation for gestalt edge grouping and contour detection. *IEEE Transactions on Image Processing* **17** (10), 1950-62 (2008).
9. Limprasert, W. PathFinding; Available from: www.mathworks.com/matlabcentral/fileexchange/34966-pathfinding (2012).
10. George, S.A., *et al.* Extracellular sodium and potassium levels modulate cardiac conduction in mice heterozygous null for the Connexin43 gene. *Pflugers Archiv: European Journal of Physiology* (2015).
11. Revel, J.P. and M.J. Karnovsky, Hexagonal array of subunits in intercellular junctions of the mouse heart and liver. *Journal of Cell Biology* **33** (3), C7-C12 (1967).
12. Huttner, I., M. Boutet, and R.H. More, Gap junctions in arterial endothelium. *Journal of Cell Biology* **57** (1), 247-52 (1973).
13. Makowski, L., *et al.* Gap junction structures. II. Analysis of the x-ray diffraction data. *Journal of Cell Biology* **74** (2), 629-45 (1977).
14. Entz, M., 2nd, *et al.* Heart Rate and Extracellular Sodium and Potassium Modulation of Gap Junction Mediated Conduction in Guinea Pigs. *Frontiers in Physiology* **7**, 16 (2016).
15. Sild, M., R.P. Chatelain, and E.S. Ruthazer, Improved method for the quantification of motility in glia and other morphologically complex cells. *Neural Plasticity* **2013**, 853727 (2013).
16. Rhett, J.M., *et al.* The perinexus: Sign-post on the path to a new model of cardiac conduction? *Trends in Cardiovascular Medicine* (2013).

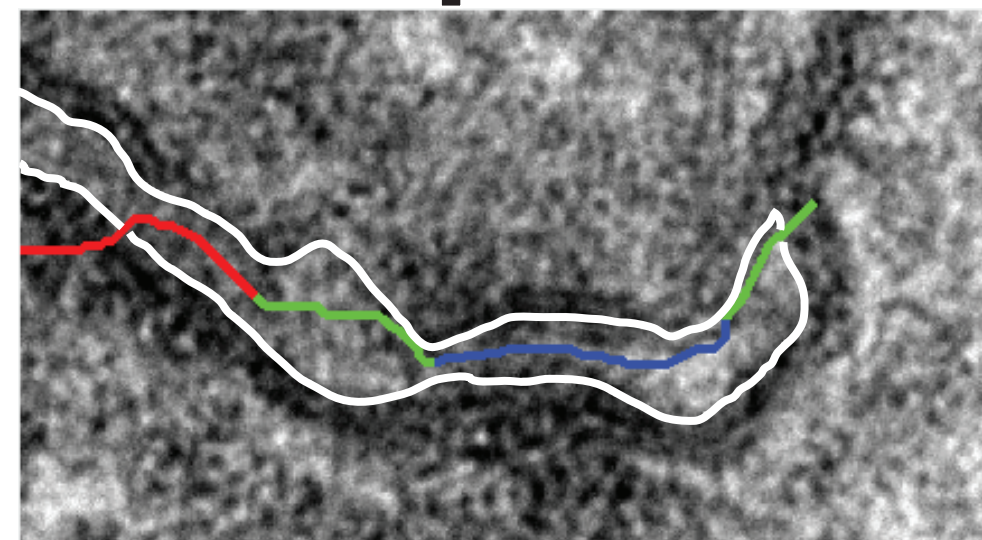
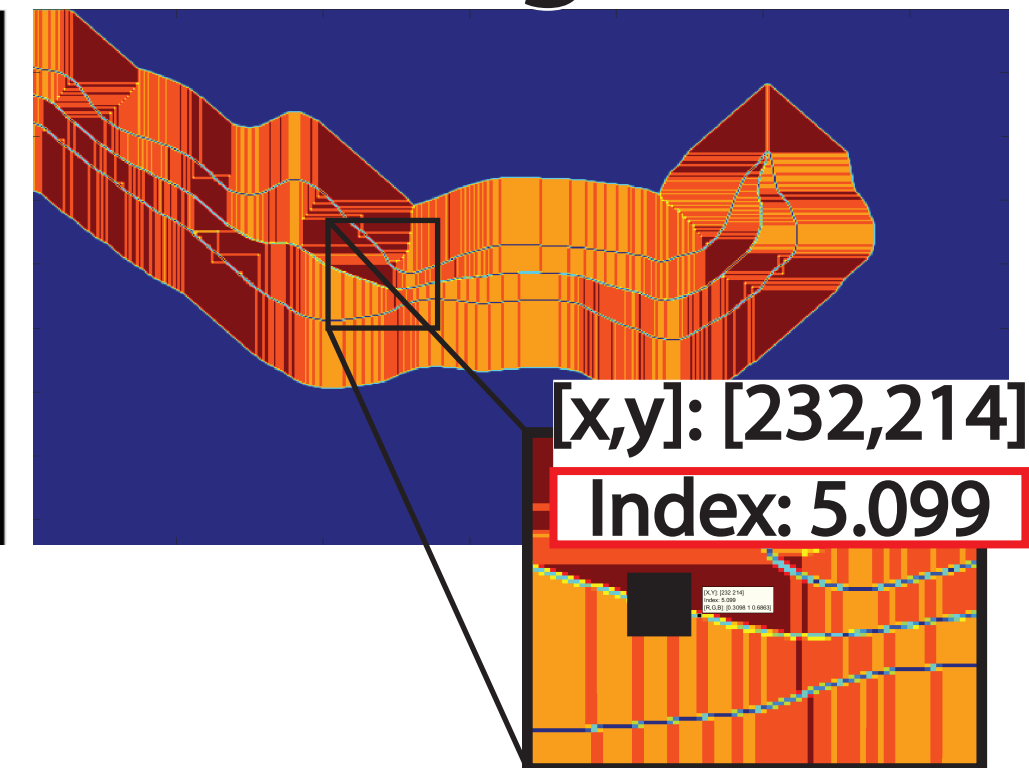
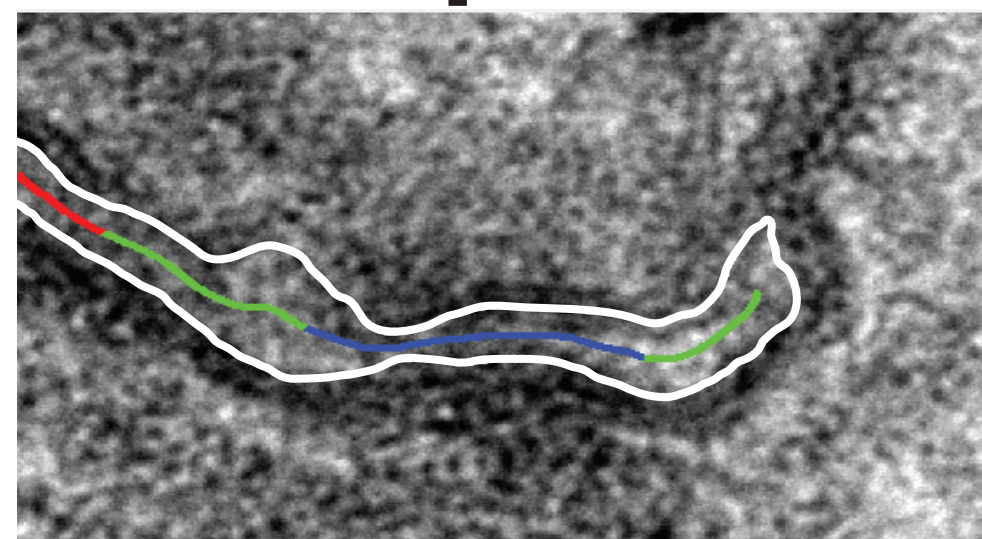
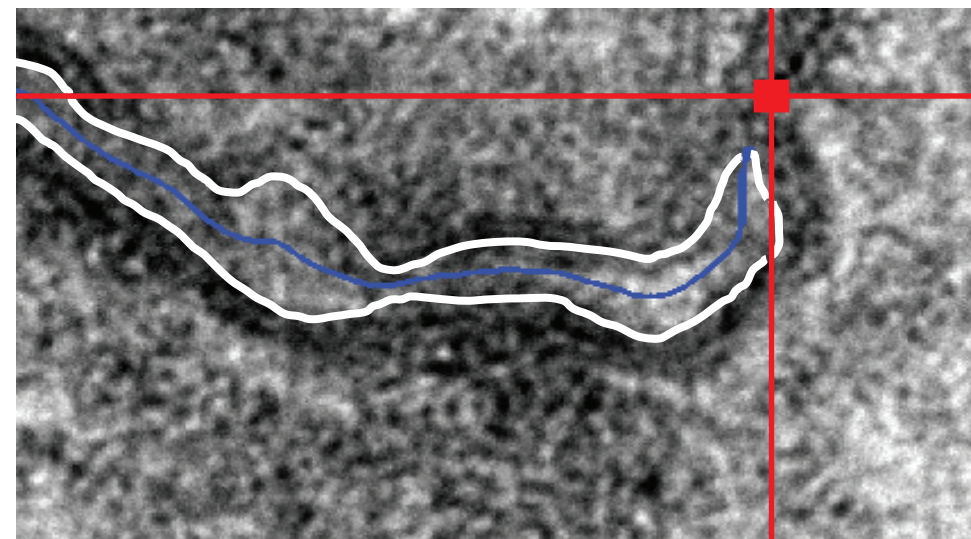
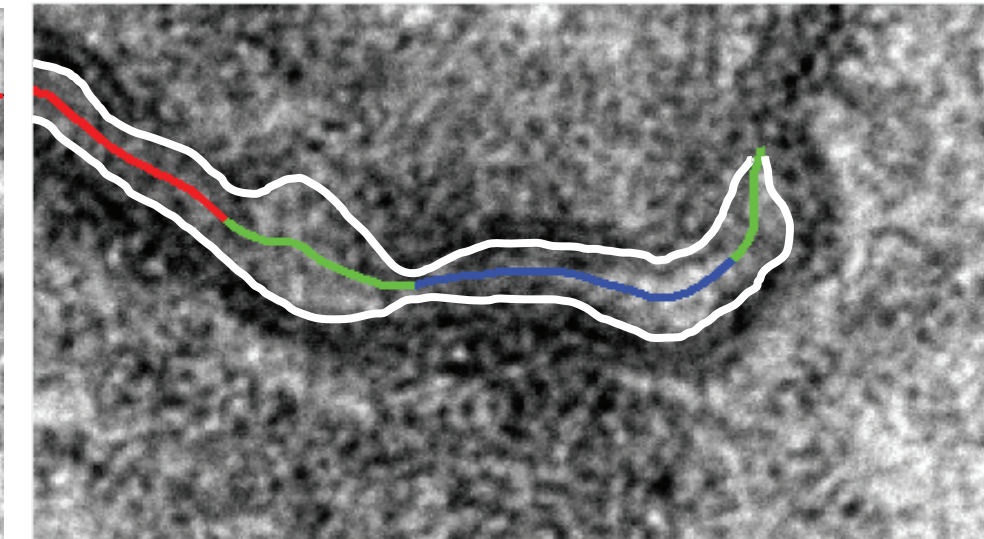
17. Lang, R.M., *et al.* Recommendations for cardiac chamber quantification by echocardiography in adults: an update from the American Society of Echocardiography and the European Association of Cardiovascular Imaging. *Journal of the American Society of Echocardiography* **28** (1), 1-39 e14 (2015).
18. Kawai, J., *et al.* Left ventricular volume and ejection fraction by the axis auto ejection fraction method: comparison with manual trace method and visual assessment of ejection fraction. *Journal of Cardiology* **49** (3), 125-34 (2007).
19. Frederiksen, C.A., *et al.* Clinical utility of semi-automated estimation of ejection fraction at the point-of-care. *Heart, Lung and Vessels* **7** (3), 208-16 (2015).
20. Foster, F.S., *et al.* A new ultrasound instrument for in vivo microimaging of mice. *Ultrasound in Medicine and Biology* **28** (9), 1165-72 (2002).
21. Moran, C.M., *et al.* A comparison of the imaging performance of high resolution ultrasound scanners for preclinical imaging. *Ultrasound in Medicine and Biology* **37** (3), 493-501 (2011).
22. Papademetris, X., *et al.* Estimation of 3D left ventricular deformation from echocardiography. *Medical Image Analysis* **5** (1), 17-28 (2001).
23. Hosny, A., *et al.* Unlocking vendor-specific tags: Three-dimensional printing of echocardiographic data sets. *Journal of Thoracic Cardiovascular Surgery* **155** (1), 143-145 e1 (2018).
24. Cretoi, D., *et al.* Human cardiac telocytes: 3D imaging by FIB-SEM tomography. *Journal of Cellular and Molecular Medicine* **18** (11), 2157-64 (2014).
25. Risi, C., *et al.* Ca(2+)-induced movement of tropomyosin on native cardiac thin filaments revealed by cryoelectron microscopy. *Proceedings of the National Academy of Sciences of the United States of America* **114** (26), 6782-6787 (2017).
26. Dhindwal, S., *et al.* A cryo-EM-based model of phosphorylation- and FKBP12.6-mediated allosterism of the cardiac ryanodine receptor. *Science Signaling* **10** (480) (2017).
27. Reddy, V.Y., *et al.* Integration of cardiac magnetic resonance imaging with three-dimensional electroanatomic mapping to guide left ventricular catheter manipulation: feasibility in a porcine model of healed myocardial infarction. *Journal of the American College of Cardiology* **44** (11), 2202-13 (2004).
28. van Heeswijk, R.B., *et al.* Three-Dimensional Self-Navigated T2 Mapping for the Detection of Acute Cellular Rejection After Orthotopic Heart Transplantation. *Transplant Direct* **3** (4), e149 (2017).
29. Valinoti, M., *et al.* 3D patient-specific models for left atrium characterization to support ablation in atrial fibrillation patients. *Magnetic Resonance Imaging* **45**, 51-57 (2018).

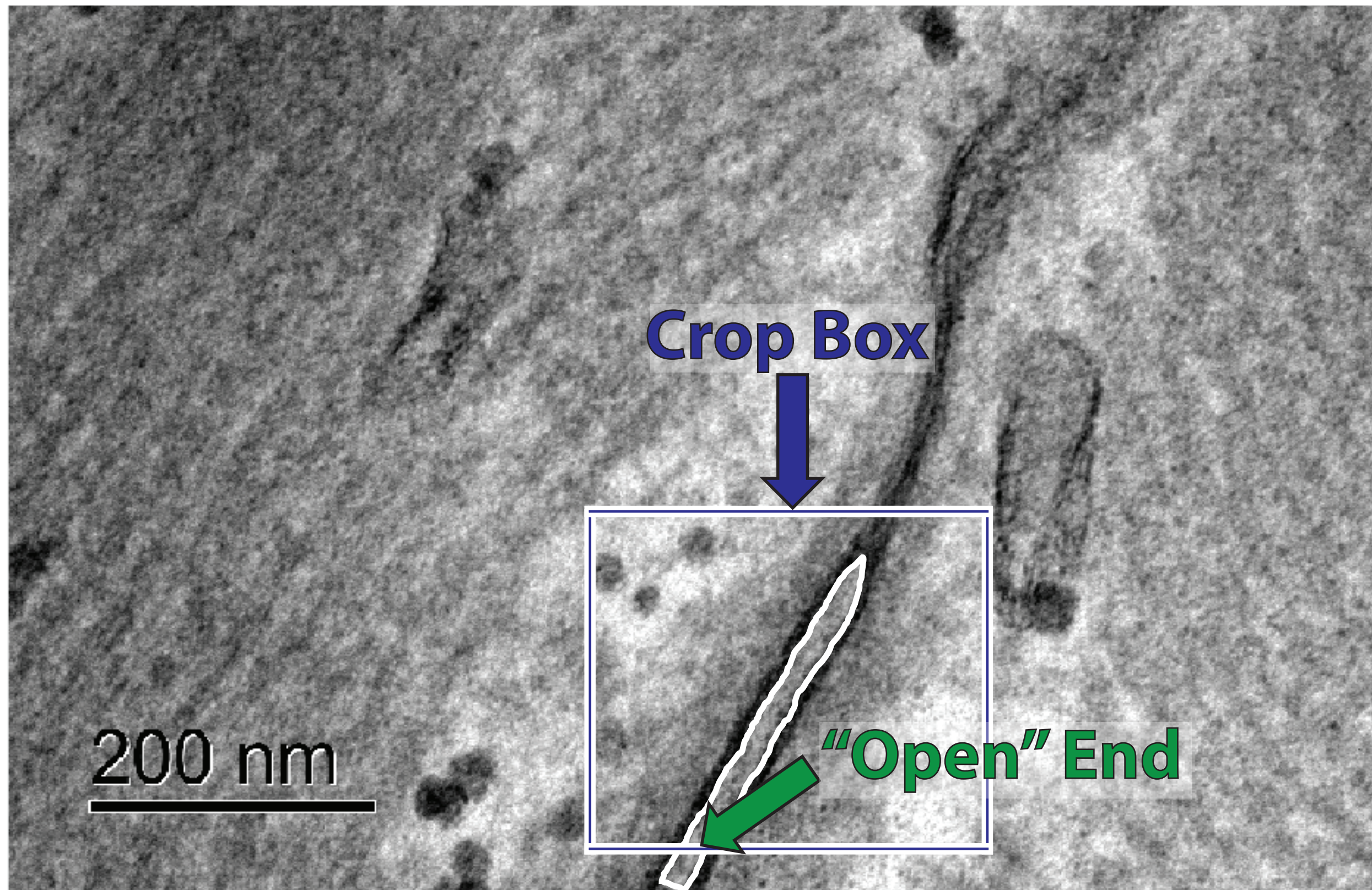
A Manual Segmentation



B Trace + Automatic



A: "Cropim"**B: "CLFinal"****C: "Gmag"****D: "Cropim"****E: "Cropim"****F: "Cropim"**



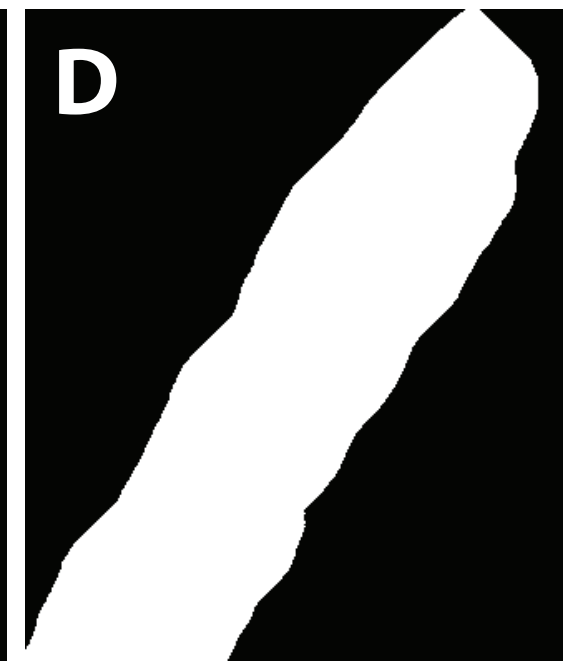
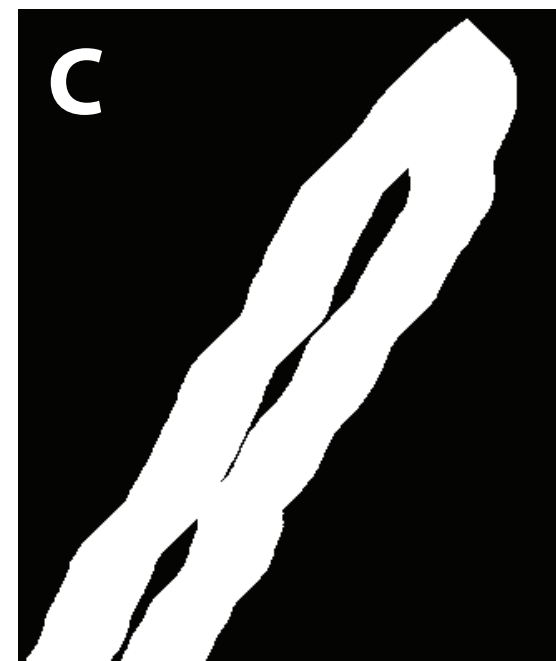
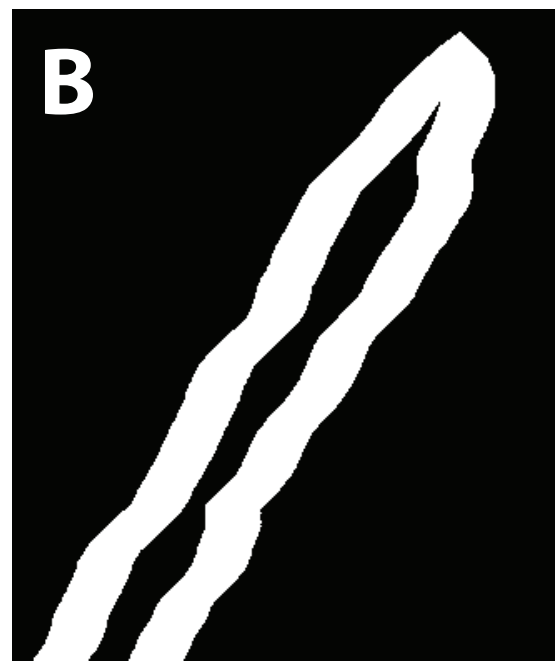
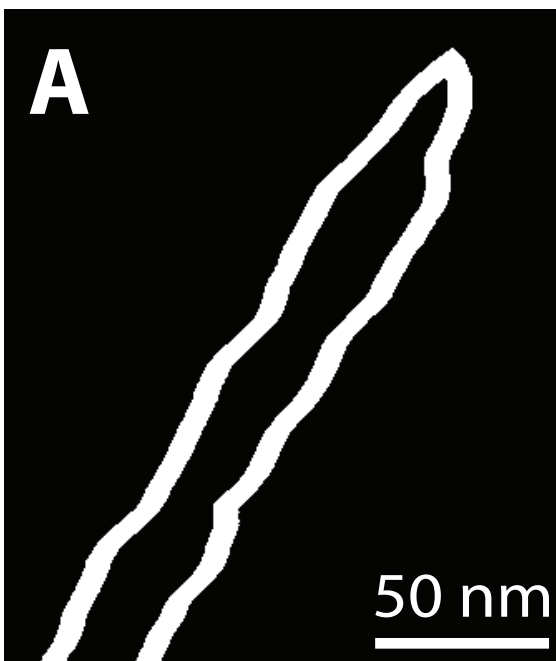
Binary

Dilation 3

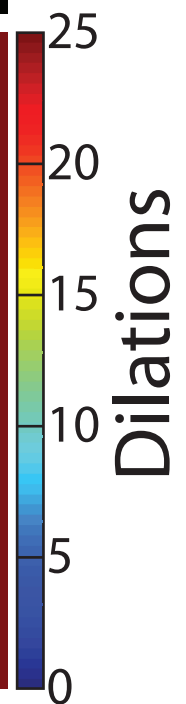
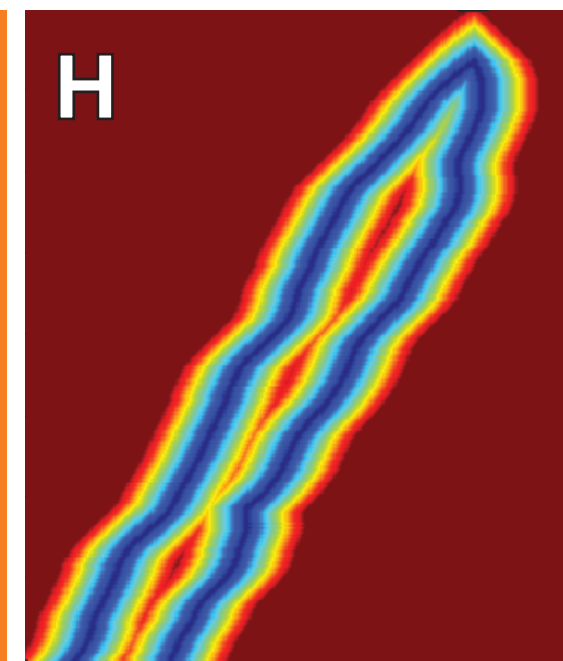
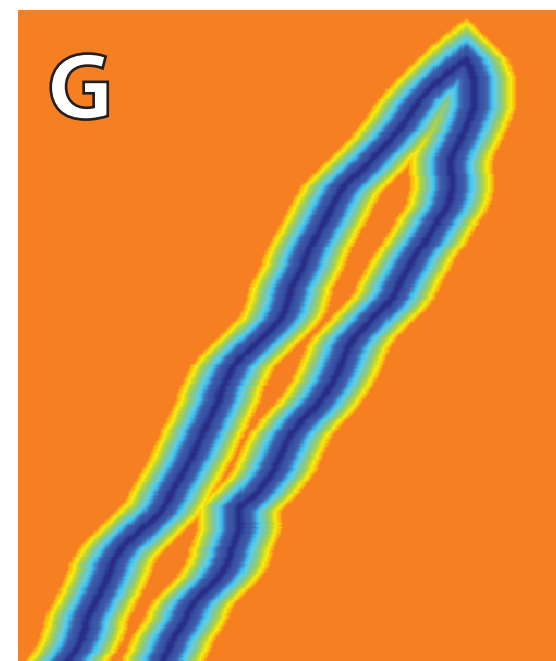
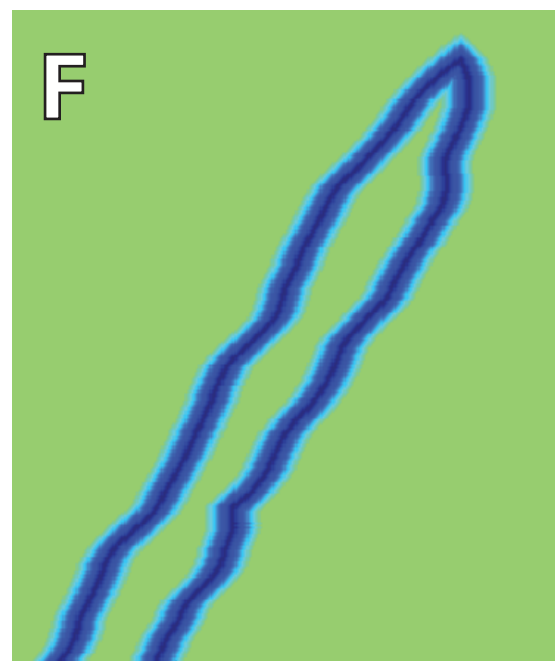
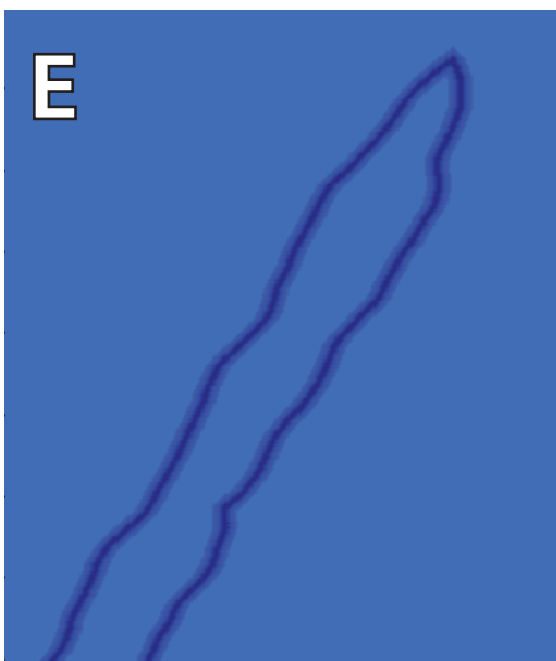
Dilation 10

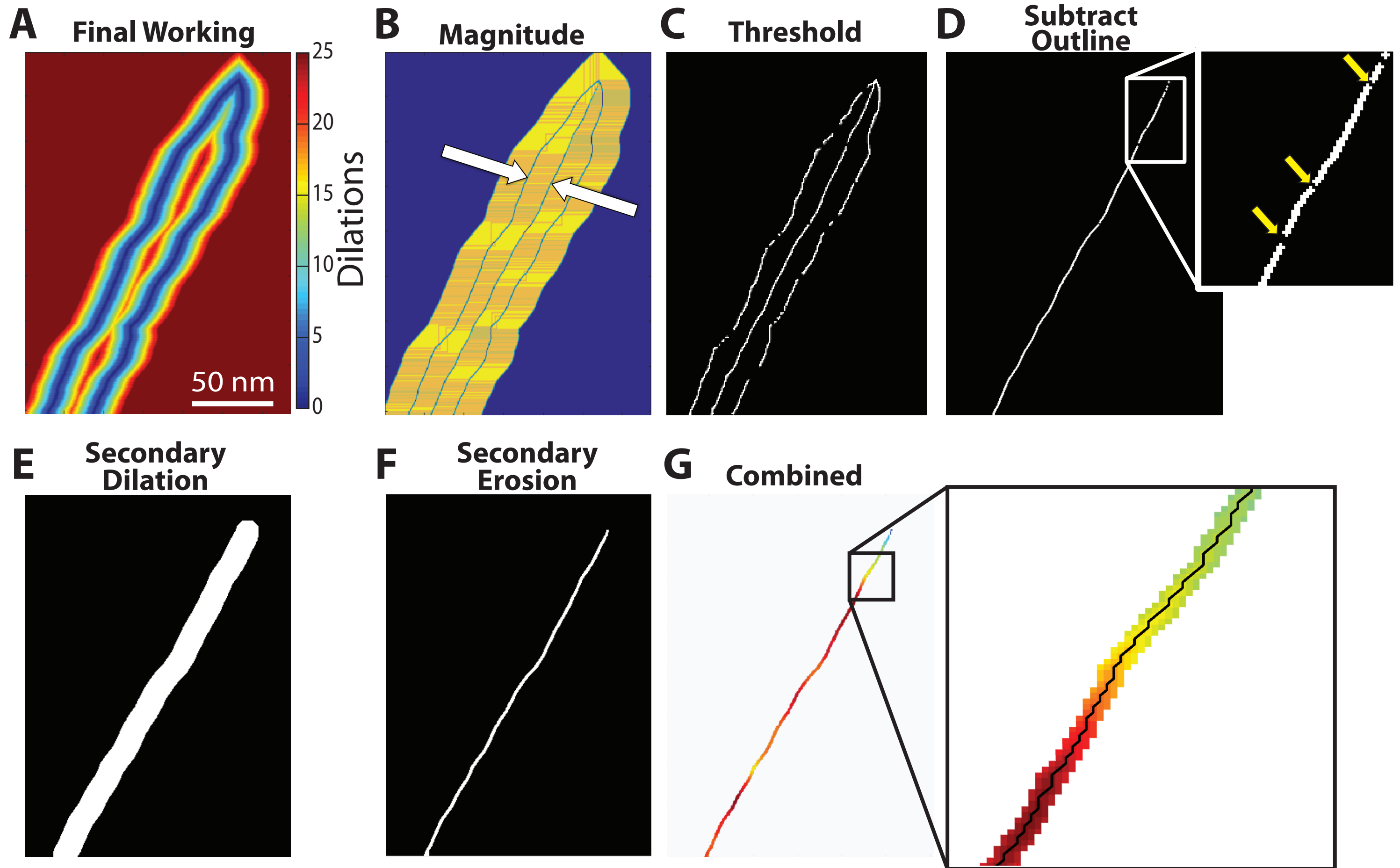
Dilation 17

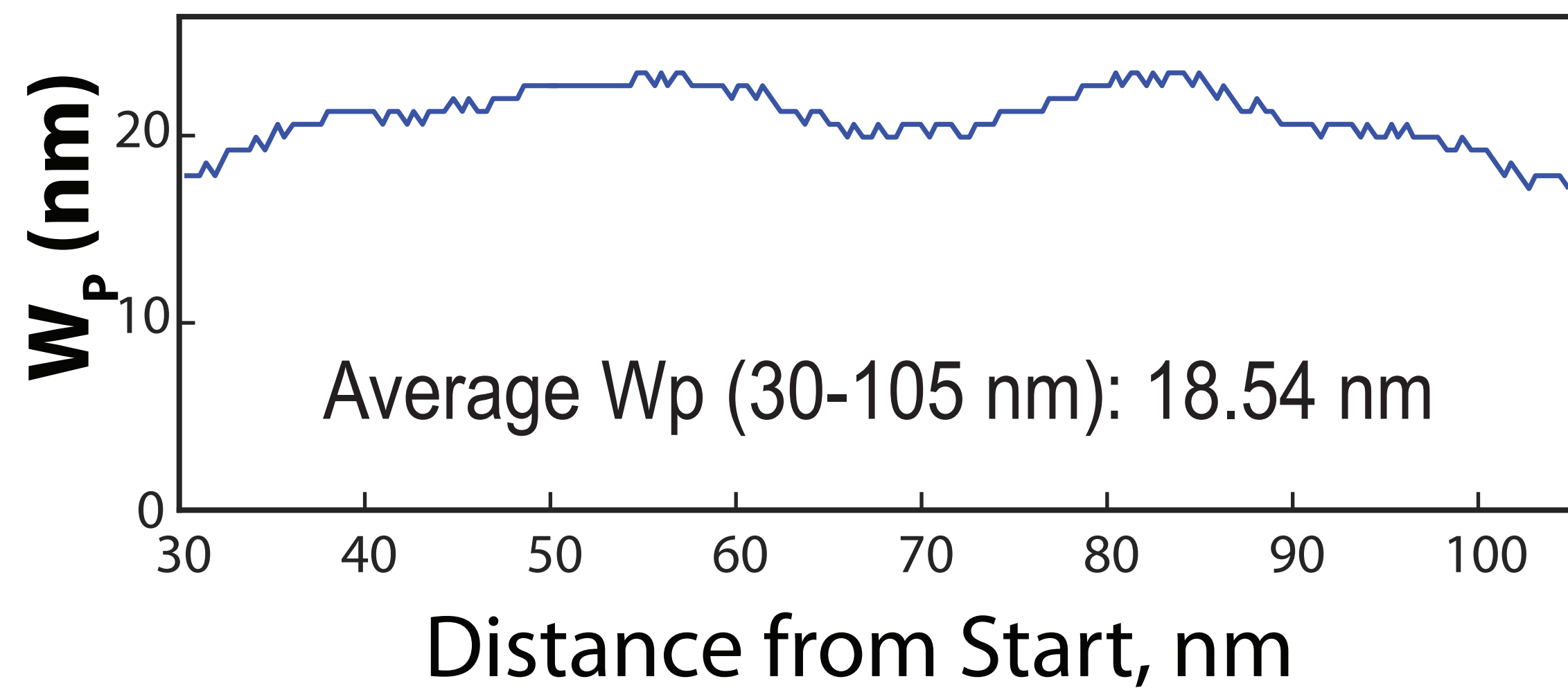
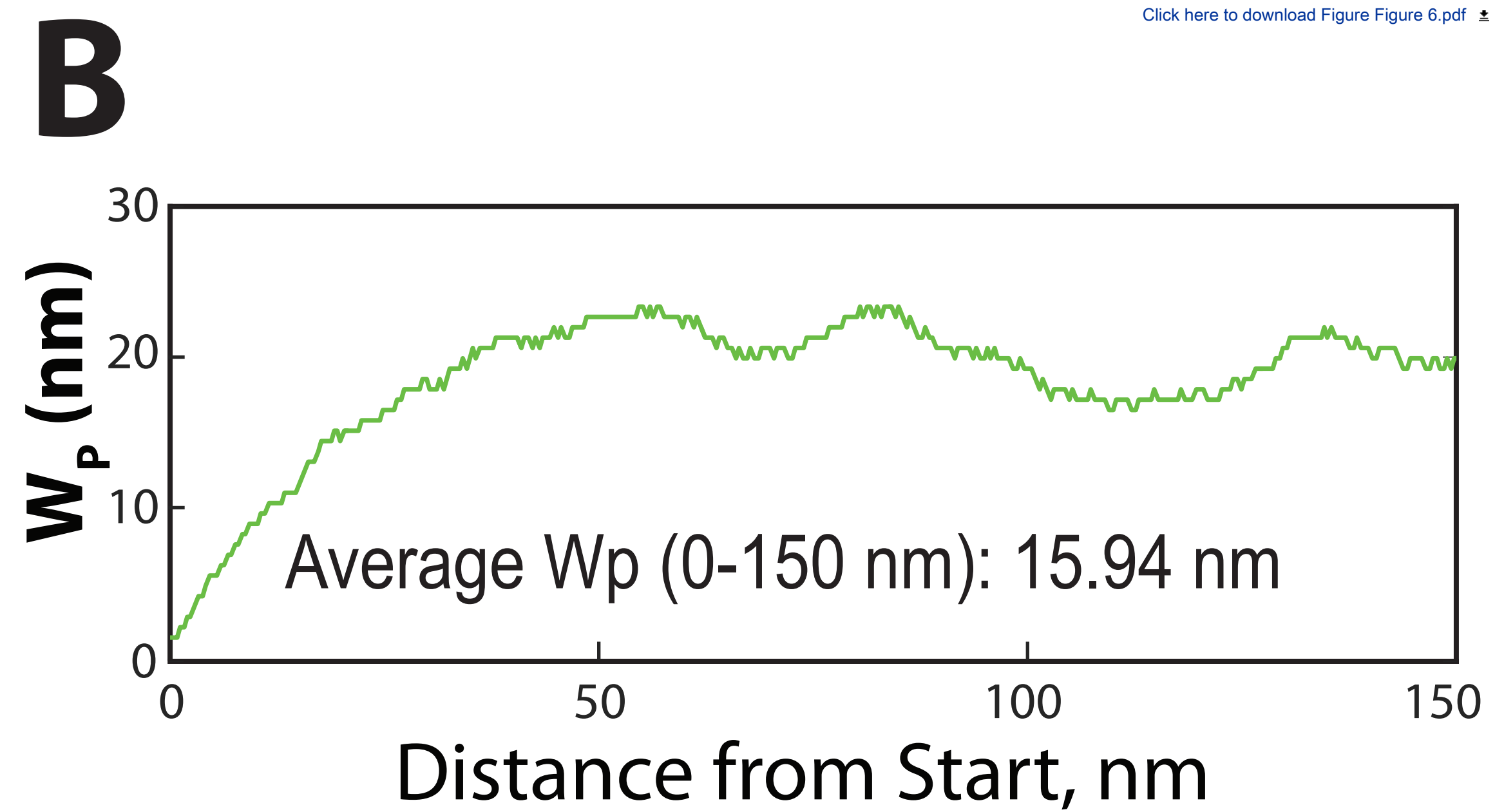
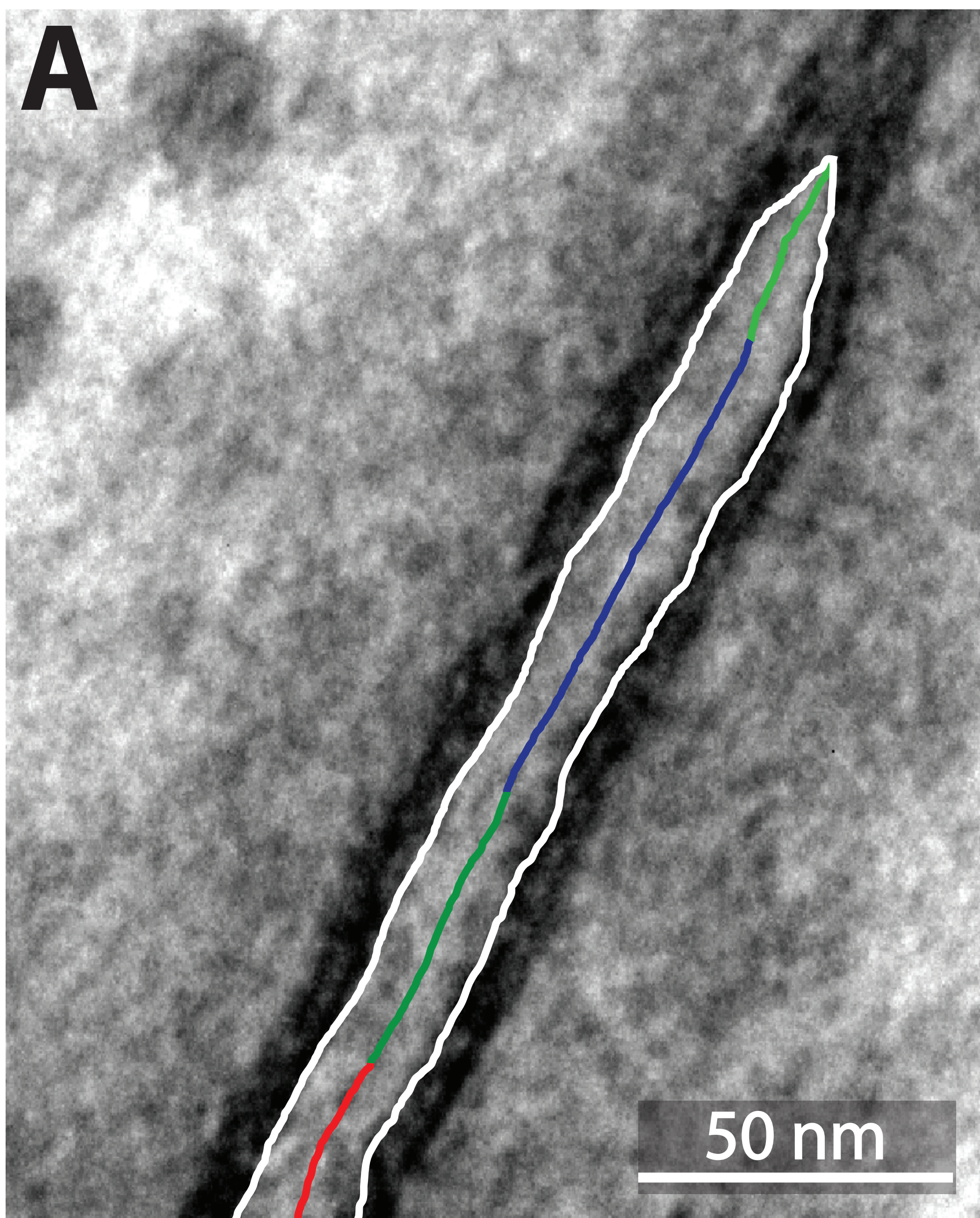
Dilation 24

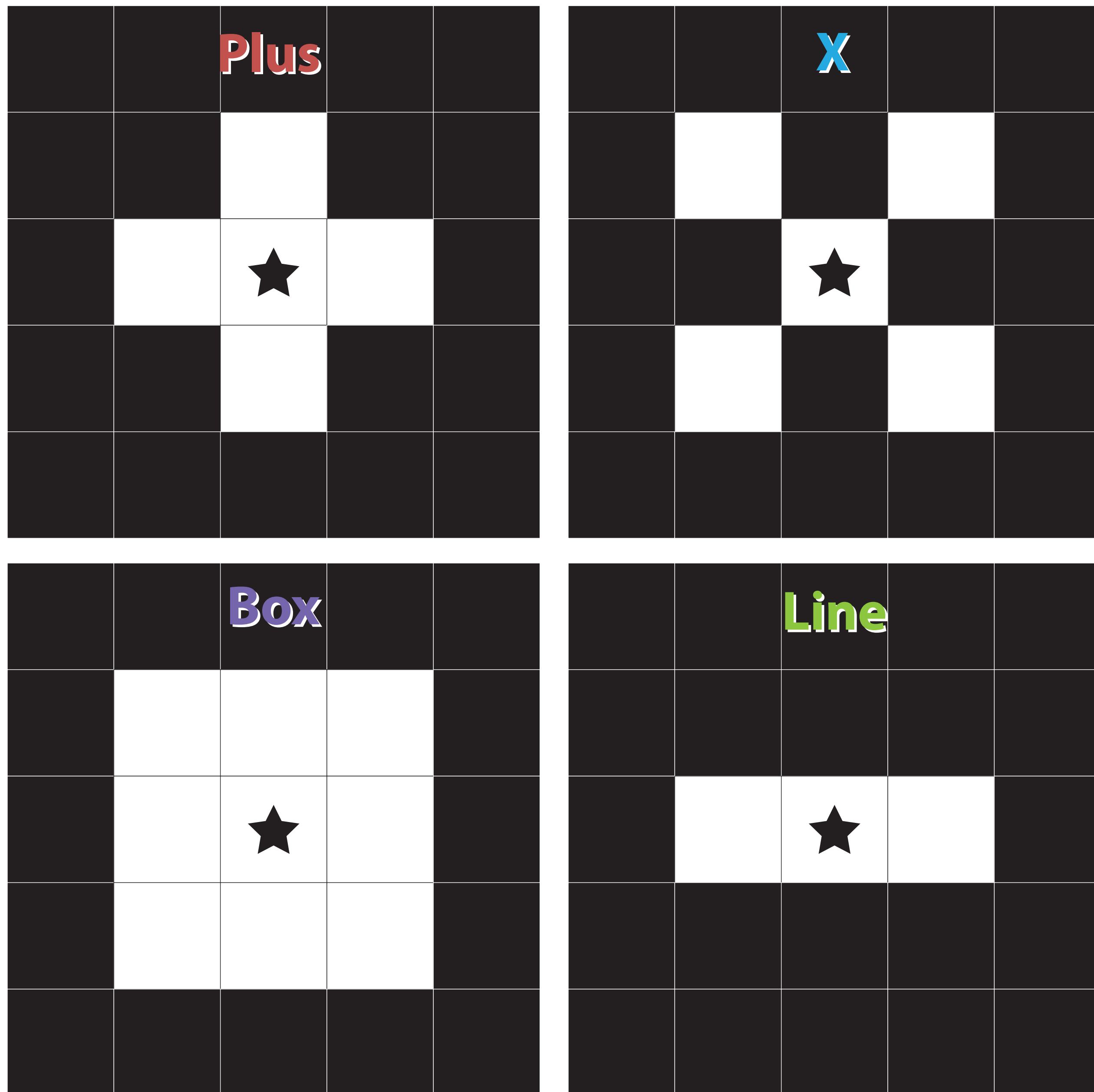
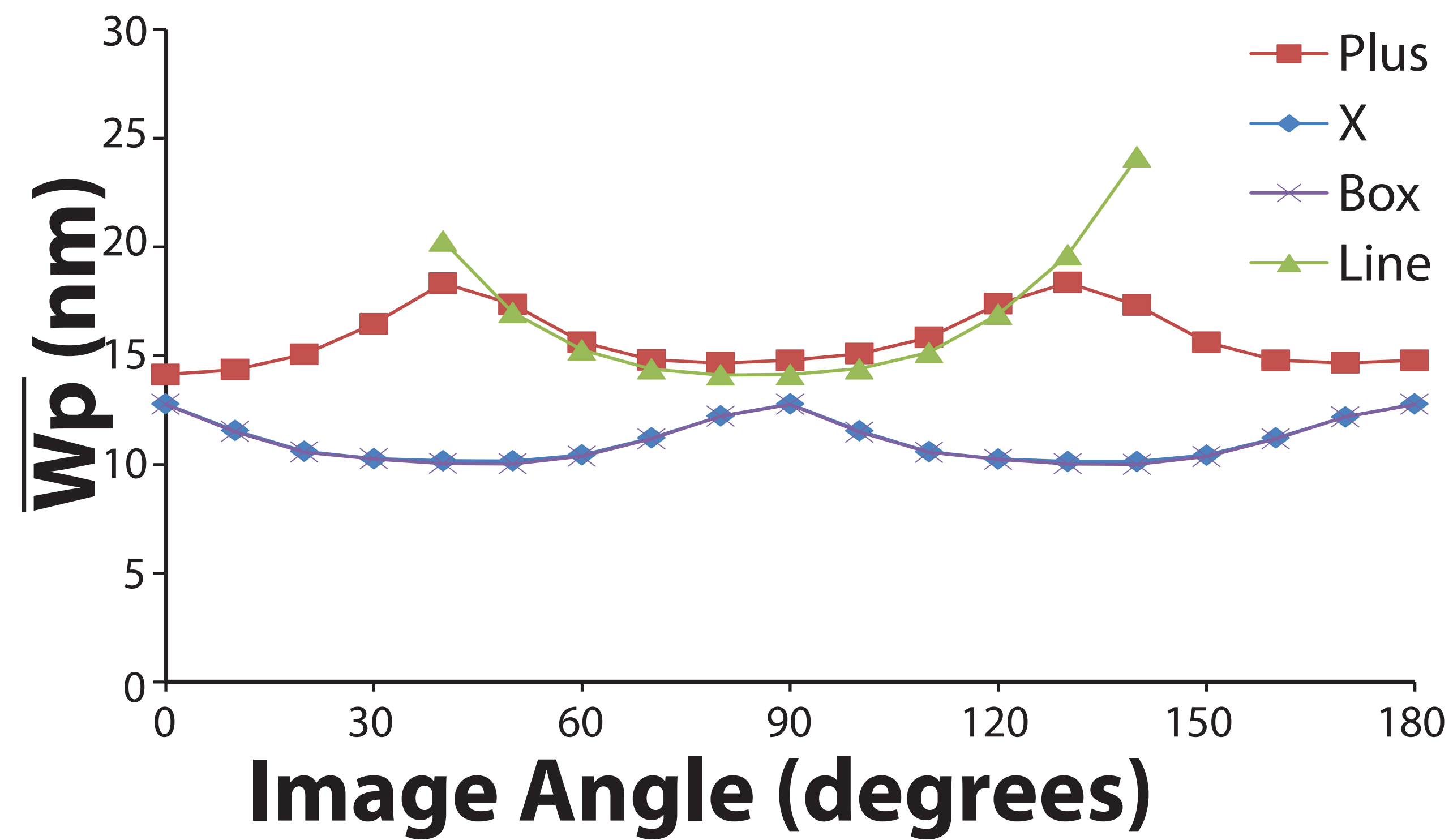
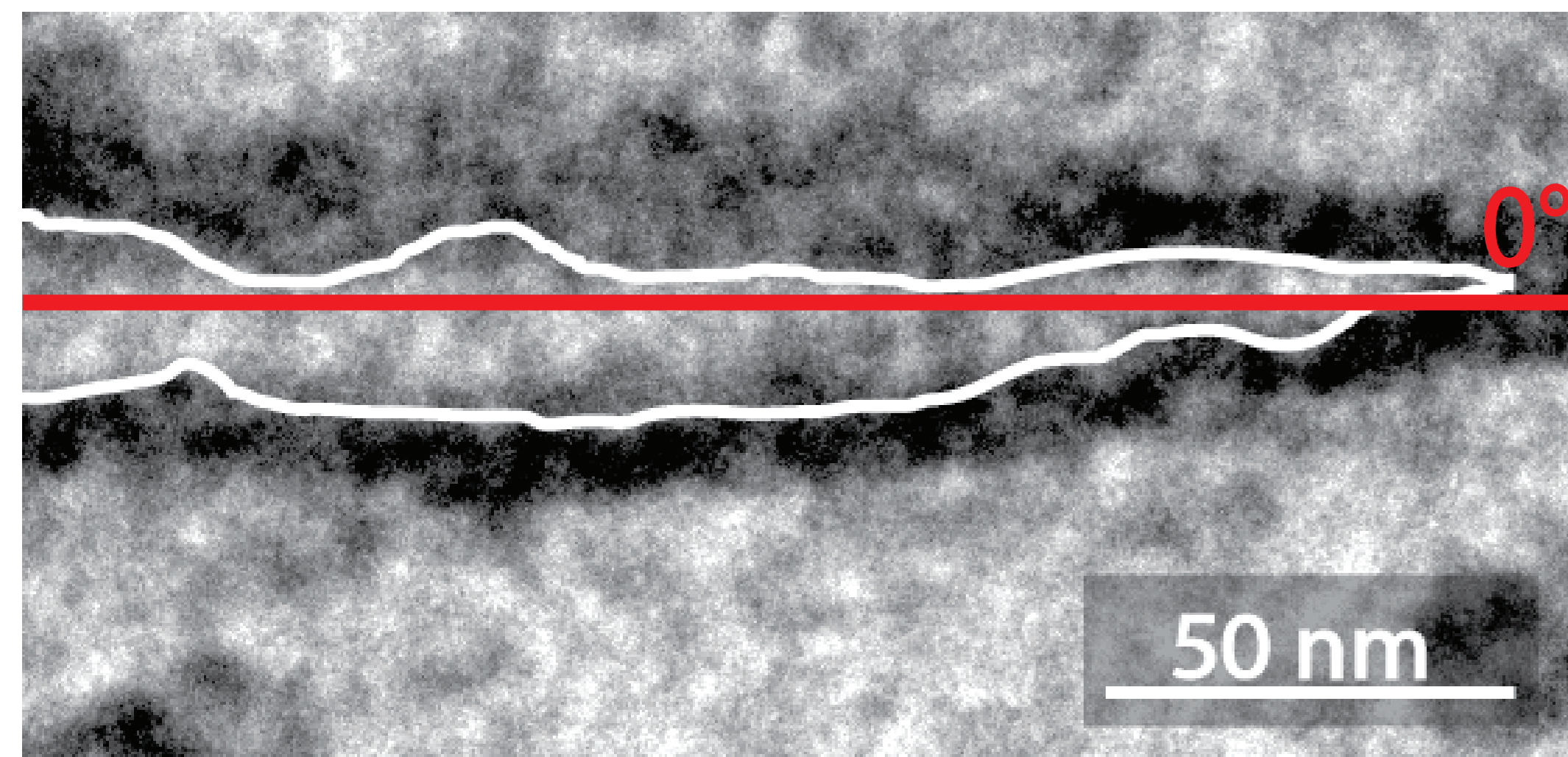


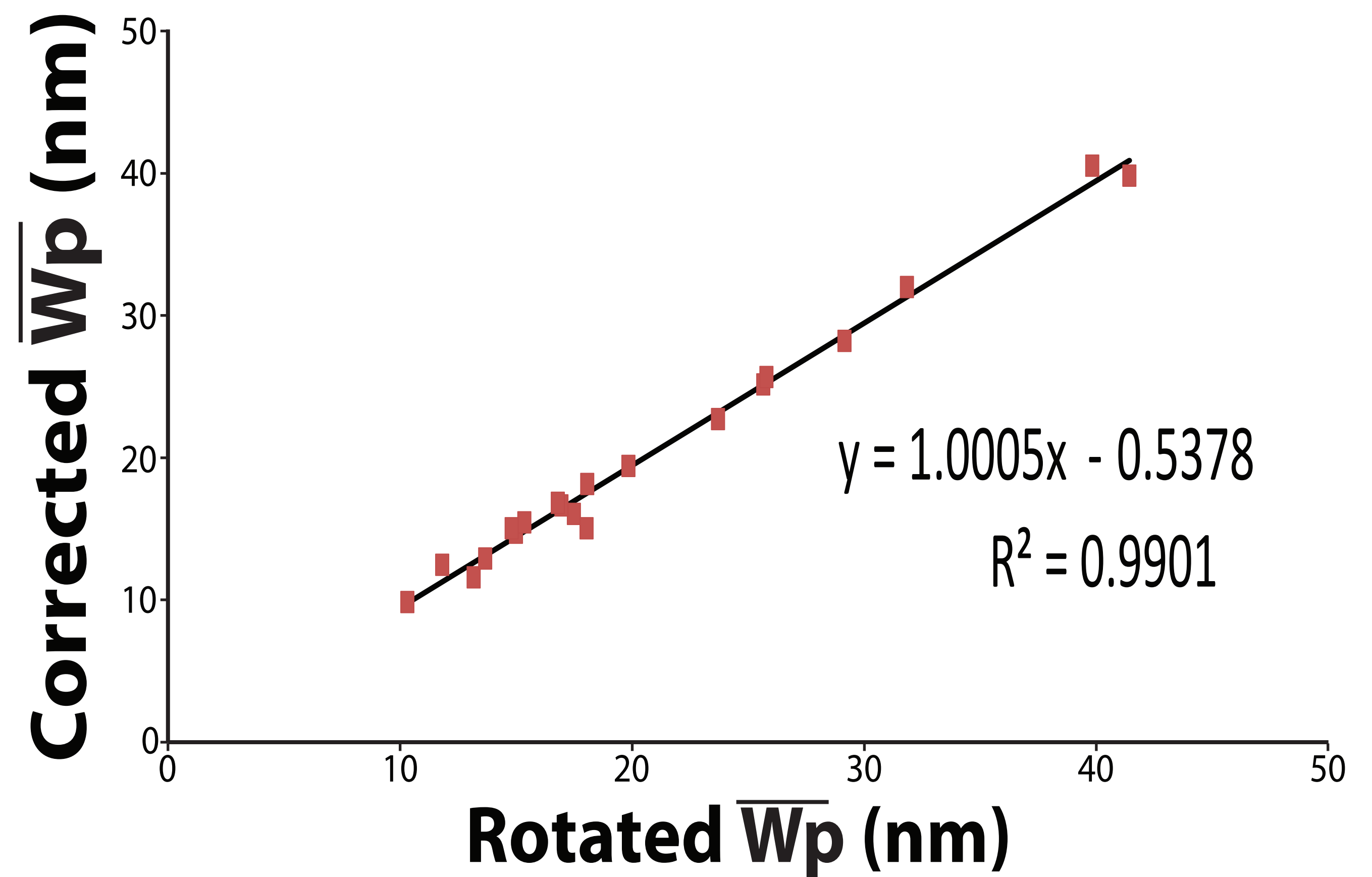
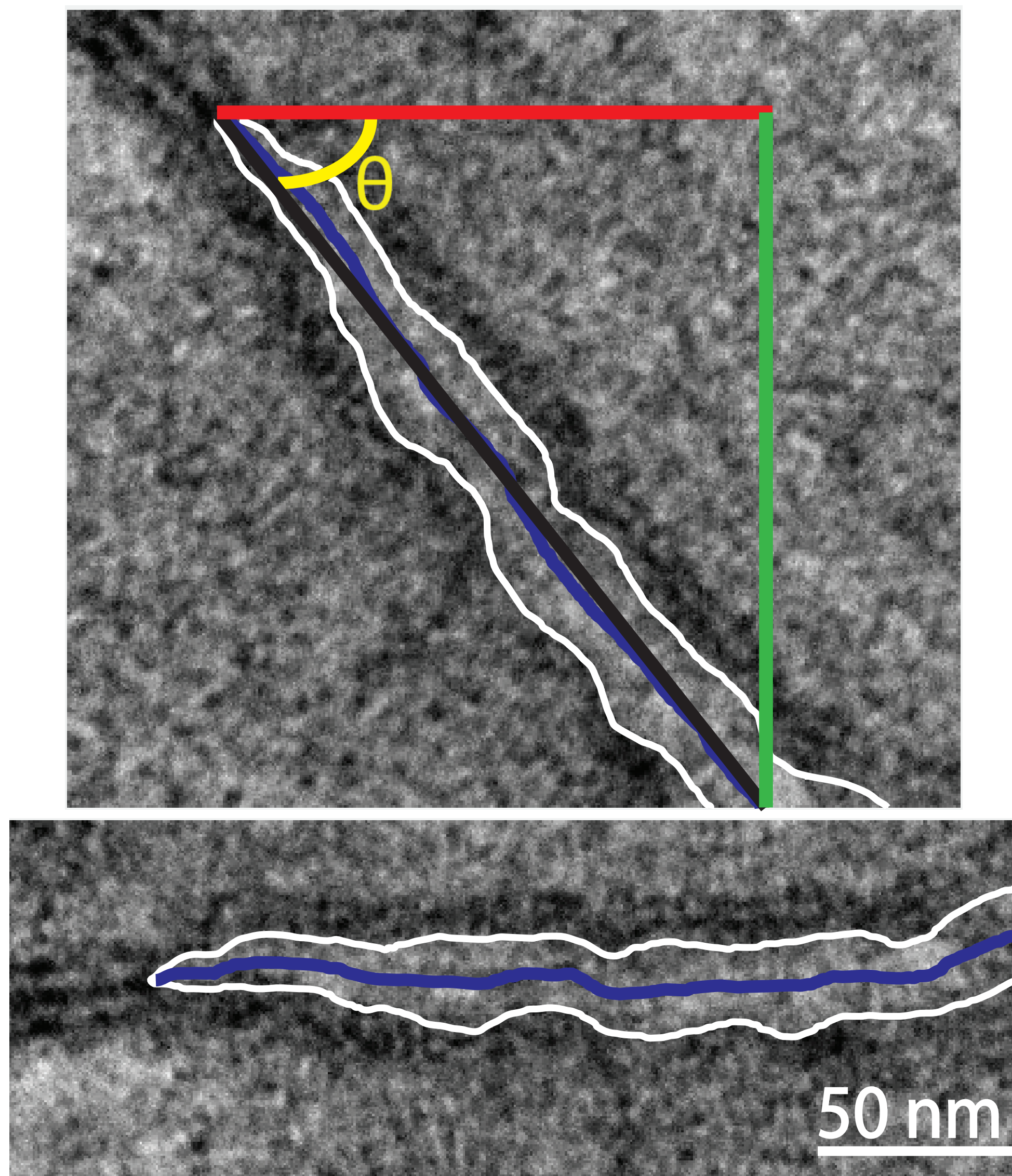
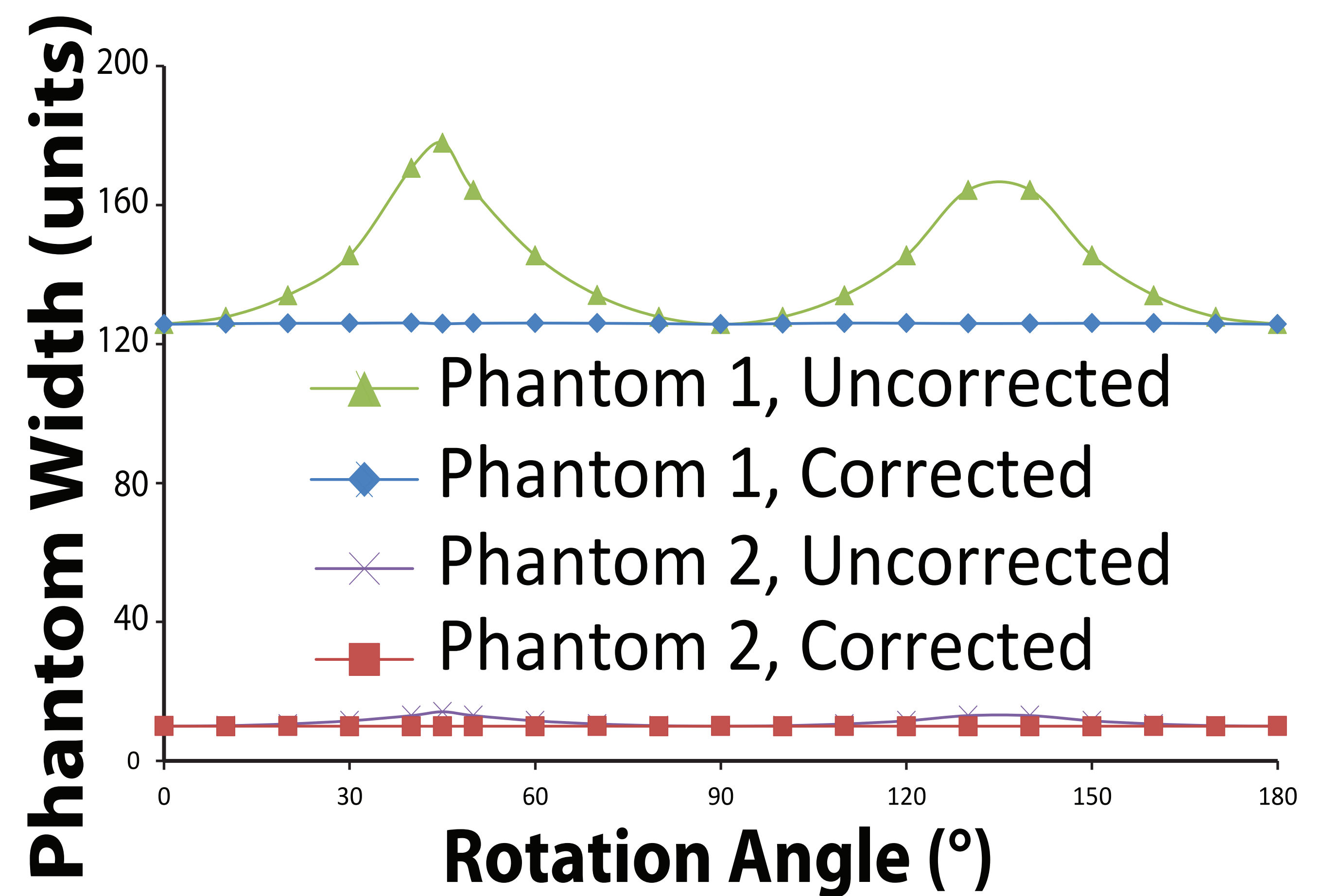
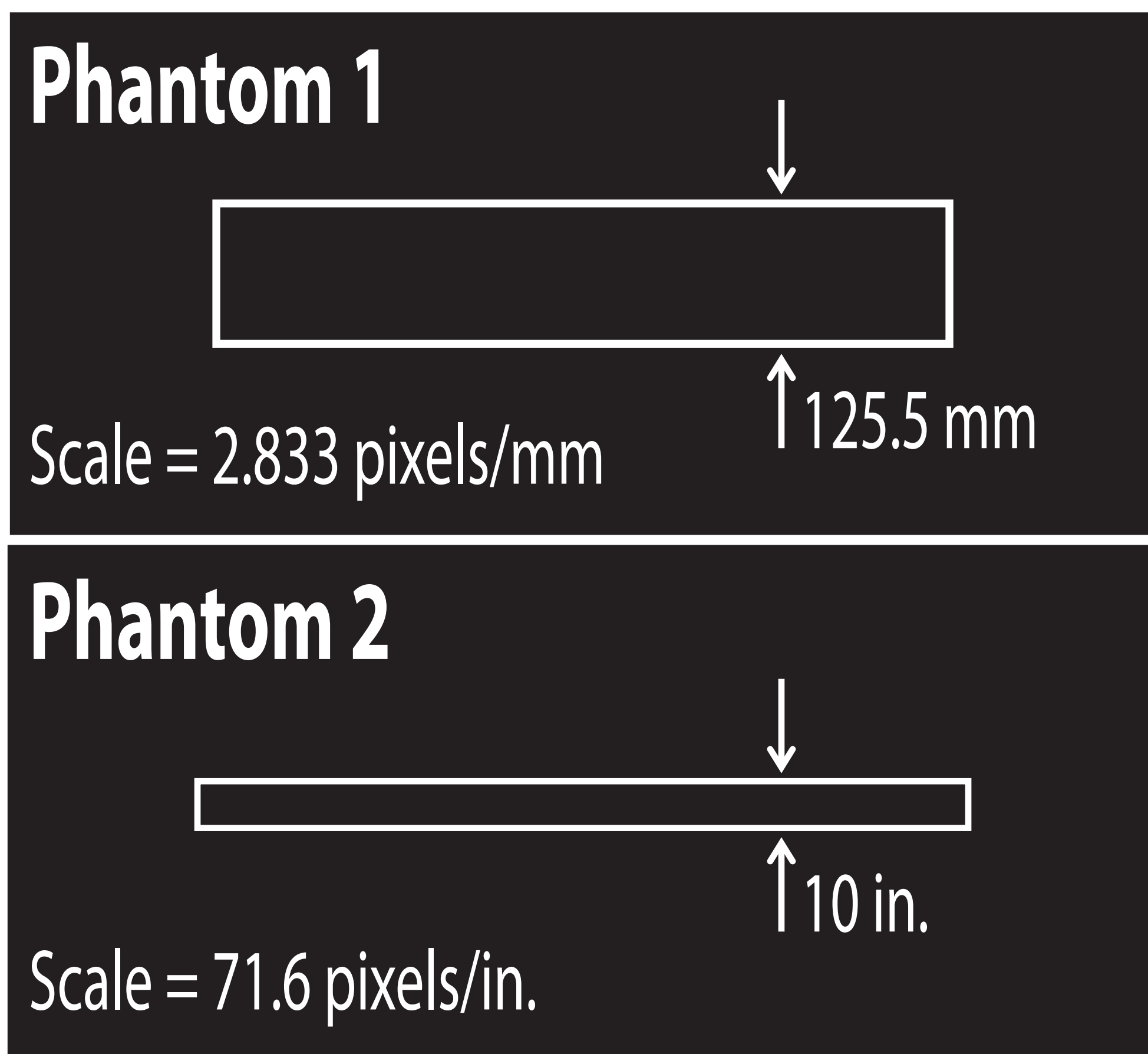
Working

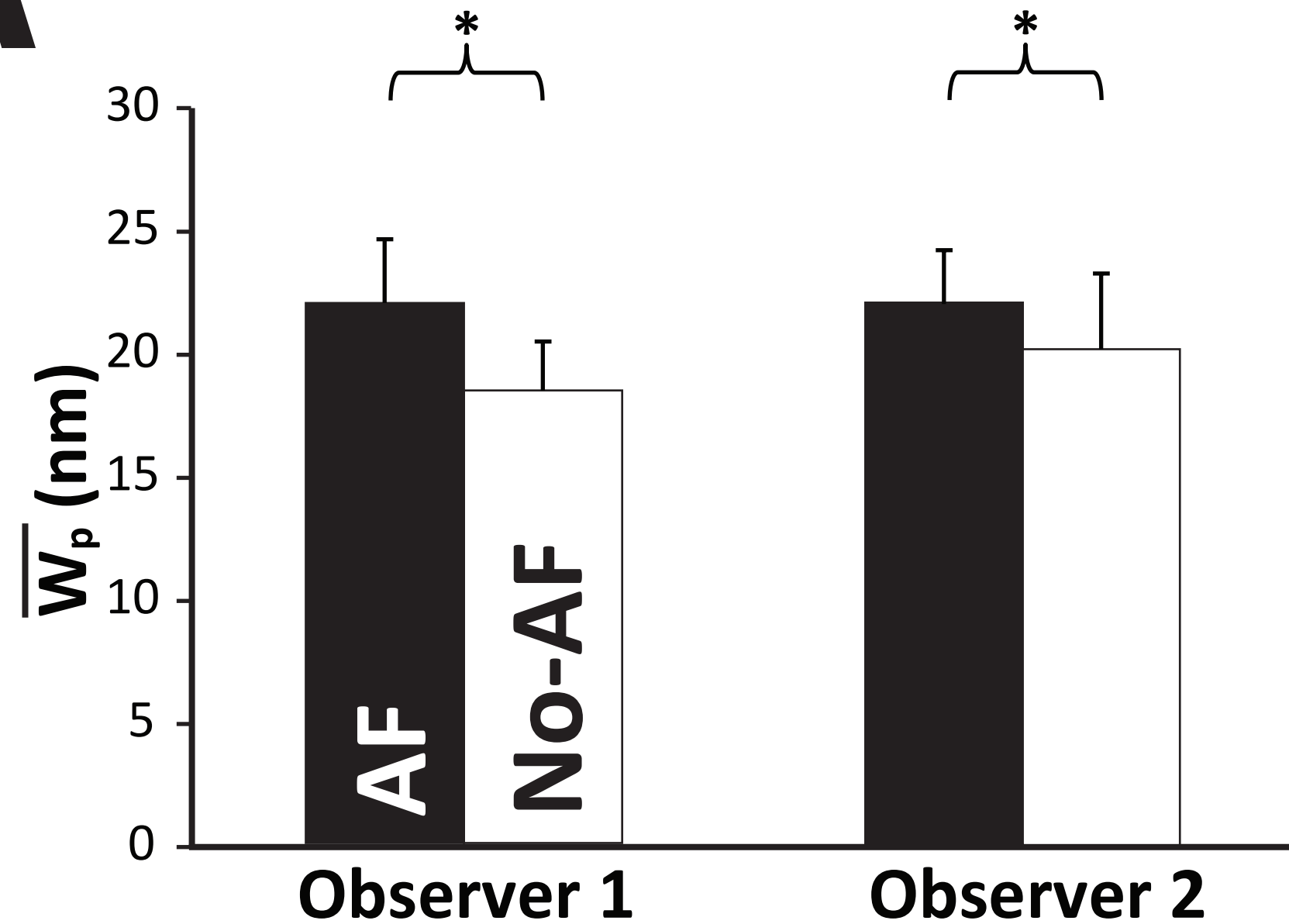
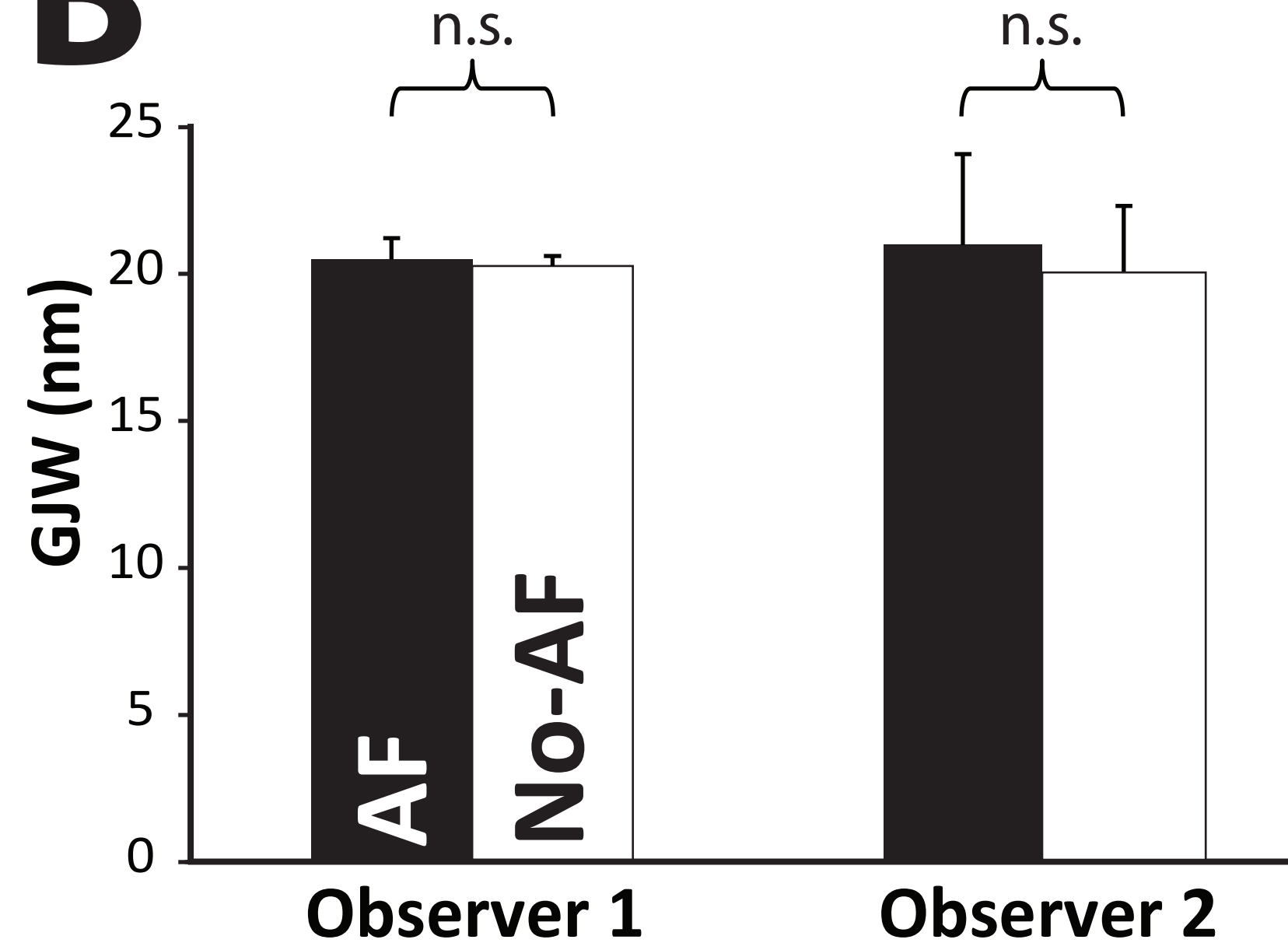






A**B**

A**B**

A**B**

	Manual	Automatic
Time - Obs. 1 (s)	205±11	44±14
Time - Obs. 2 (s)	248±18	30±5
Spatial Resolution (measurements/nm)	0.08	3.45

Name of Material/ Equipment	Company	Catalog Number
Touchscreen Monitor	Dell	S2240T
Desktop	Dell	Precision T1650
Operating System	Microsoft	Windows 7
Program platform	Mathworks	Matlab R2015b

Comments/Description

Needs soft-tipped stylus

8GB RAM

64-bit OS

Program may be incompatible with newer/older versions of Matlab



1 Alewife Center #200
 Cambridge, MA 02140
 tel. 617.945.9051
www.jove.com

ARTICLE AND VIDEO LICENSE AGREEMENT

Title of Article:

Quantifying Intermembrane Distances with Serial Image Dilations in Matlab

Author(s):

Tristan Raisch, Momina Khan, Steven Poelzing

Item 1 (check one box): The Author elects to have the Materials be made available (as described at <http://www.jove.com/author>) via: ☒ Standard Access ☐ Open Access

Item 2 (check one box):

☒

The Author is NOT a United States government employee.

☐

The Author is a United States government employee and the Materials were prepared in the course of his or her duties as a United States government employee.

☐

The Author is a United States government employee but the Materials were NOT prepared in the course of his or her duties as a United States government employee.

ARTICLE AND VIDEO LICENSE AGREEMENT

1. **Defined Terms.** As used in this Article and Video License Agreement, the following terms shall have the following meanings: “**Agreement**” means this Article and Video License Agreement; “**Article**” means the article specified on the last page of this Agreement, including any associated materials such as texts, figures, tables, artwork, abstracts, or summaries contained therein; “**Author**” means the author who is a signatory to this Agreement; “**Collective Work**” means a work, such as a periodical issue, anthology or encyclopedia, in which the Materials in their entirety in unmodified form, along with a number of other contributions, constituting separate and independent works in themselves, are assembled into a collective whole; “**CRC License**” means the Creative Commons Attribution-Non Commercial-No Derivs 3.0 Unported Agreement, the terms and conditions of which can be found at: <http://creativecommons.org/licenses/by-nc-nd/3.0/legalcode>; “**Derivative Work**” means a work based upon the Materials or upon the Materials and other pre-existing works, such as a translation, musical arrangement, dramatization, fictionalization, motion picture version, sound recording, art reproduction, abridgment, condensation, or any other form in which the Materials may be recast, transformed, or adapted; “**Institution**” means the institution, listed on the last page of this Agreement, by which the Author was employed at the time of the creation of the Materials; “**JoVE**” means MyJoVE Corporation, a Massachusetts corporation and the publisher of *The Journal of Visualized Experiments*; “**Materials**” means the Article and / or the Video; “**Parties**” means the Author and JoVE; “**Video**” means any video(s) made by the Author, alone or in conjunction with any other parties, or by JoVE or its affiliates or agents, individually or in collaboration with the Author or any other parties, incorporating all or any portion of the Article, and in which the Author may or may not appear.

2. **Background.** The Author, who is the author of the Article, in order to ensure the dissemination and protection of the Article, desires to have the JoVE publish the Article and create and transmit videos based on the Article. In furtherance of such goals, the Parties desire to memorialize in this Agreement the respective rights of each Party in and to the Article and the Video.

3. **Grant of Rights in Article.** In consideration of JoVE agreeing to publish the Article, the Author hereby grants to JoVE, subject to **Sections 4** and **7** below, the exclusive, royalty-free, perpetual (for the full term of copyright in the Article, including any extensions thereto) license (a) to publish, reproduce, distribute, display and store the Article in all forms, formats and media whether now known or hereafter developed (including without limitation in print, digital and electronic form) throughout the world, (b) to translate the Article into other languages, create adaptations, summaries or extracts of the Article or other Derivative Works (including, without limitation, the Video) or Collective Works based on all or any portion of the Article and exercise all of the rights set forth in (a) above in such translations, adaptations, summaries, extracts, Derivative Works or Collective Works and (c) to license others to do any or all of the above. The foregoing rights may be exercised in all media and formats, whether now known or hereafter devised, and include the right to make such modifications as are technically necessary to exercise the rights in other media and formats. If the “Open Access” box has been checked in **Item 1** above, JoVE and the Author hereby grant to the public all such rights in the Article as provided in, but subject to all limitations and requirements set forth in, the CRC License.

ARTICLE AND VIDEO LICENSE AGREEMENT

4. Retention of Rights in Article. Notwithstanding the exclusive license granted to JoVE in **Section 3** above, the Author shall, with respect to the Article, retain the non-exclusive right to use all or part of the Article for the non-commercial purpose of giving lectures, presentations or teaching classes, and to post a copy of the Article on the Institution's website or the Author's personal website, in each case provided that a link to the Article on the JoVE website is provided and notice of JoVE's copyright in the Article is included. All non-copyright intellectual property rights in and to the Article, such as patent rights, shall remain with the Author.

5. Grant of Rights in Video – Standard Access. This **Section 5** applies if the "Standard Access" box has been checked in **Item 1** above or if no box has been checked in **Item 1** above. In consideration of JoVE agreeing to produce, display or otherwise assist with the Video, the Author hereby acknowledges and agrees that, Subject to **Section 7** below, JoVE is and shall be the sole and exclusive owner of all rights of any nature, including, without limitation, all copyrights, in and to the Video. To the extent that, by law, the Author is deemed, now or at any time in the future, to have any rights of any nature in or to the Video, the Author hereby disclaims all such rights and transfers all such rights to JoVE.

6. Grant of Rights in Video – Open Access. This **Section 6** applies only if the "Open Access" box has been checked in **Item 1** above. In consideration of JoVE agreeing to produce, display or otherwise assist with the Video, the Author hereby grants to JoVE, subject to **Section 7** below, the exclusive, royalty-free, perpetual (for the full term of copyright in the Article, including any extensions thereto) license (a) to publish, reproduce, distribute, display and store the Video in all forms, formats and media whether now known or hereafter developed (including without limitation in print, digital and electronic form) throughout the world, (b) to translate the Video into other languages, create adaptations, summaries or extracts of the Video or other Derivative Works or Collective Works based on all or any portion of the Video and exercise all of the rights set forth in (a) above in such translations, adaptations, summaries, extracts, Derivative Works or Collective Works and (c) to license others to do any or all of the above. The foregoing rights may be exercised in all media and formats, whether now known or hereafter devised, and include the right to make such modifications as are technically necessary to exercise the rights in other media and formats. For any Video to which this Section 6 is applicable, JoVE and the Author hereby grant to the public all such rights in the Video as provided in, but subject to all limitations and requirements set forth in, the CRC License.

7. Government Employees. If the Author is a United States government employee and the Article was prepared in the course of his or her duties as a United States government employee, as indicated in **Item 2** above, and any of the licenses or grants granted by the Author hereunder exceed the scope of the 17 U.S.C. 403, then the rights granted hereunder shall be limited to the maximum rights permitted under such

statute. In such case, all provisions contained herein that are not in conflict with such statute shall remain in full force and effect, and all provisions contained herein that do so conflict shall be deemed to be amended so as to provide to JoVE the maximum rights permissible within such statute.

8. Likeness, Privacy, Personality. The Author hereby grants JoVE the right to use the Author's name, voice, likeness, picture, photograph, image, biography and performance in any way, commercial or otherwise, in connection with the Materials and the sale, promotion and distribution thereof. The Author hereby waives any and all rights he or she may have, relating to his or her appearance in the Video or otherwise relating to the Materials, under all applicable privacy, likeness, personality or similar laws.

9. Author Warranties. The Author represents and warrants that the Article is original, that it has not been published, that the copyright interest is owned by the Author (or, if more than one author is listed at the beginning of this Agreement, by such authors collectively) and has not been assigned, licensed, or otherwise transferred to any other party. The Author represents and warrants that the author(s) listed at the top of this Agreement are the only authors of the Materials. If more than one author is listed at the top of this Agreement and if any such author has not entered into a separate Article and Video License Agreement with JoVE relating to the Materials, the Author represents and warrants that the Author has been authorized by each of the other such authors to execute this Agreement on his or her behalf and to bind him or her with respect to the terms of this Agreement as if each of them had been a party hereto as an Author. The Author warrants that the use, reproduction, distribution, public or private performance or display, and/or modification of all or any portion of the Materials does not and will not violate, infringe and/or misappropriate the patent, trademark, intellectual property or other rights of any third party. The Author represents and warrants that it has and will continue to comply with all government, institutional and other regulations, including, without limitation all institutional, laboratory, hospital, ethical, human and animal treatment, privacy, and all other rules, regulations, laws, procedures or guidelines, applicable to the Materials, and that all research involving human and animal subjects has been approved by the Author's relevant institutional review board.

10. JoVE Discretion. If the Author requests the assistance of JoVE in producing the Video in the Author's facility, the Author shall ensure that the presence of JoVE employees, agents or independent contractors is in accordance with the relevant regulations of the Author's institution. If more than one author is listed at the beginning of this Agreement, JoVE may, in its sole discretion, elect not take any action with respect to the Article until such time as it has received complete, executed Article and Video License Agreements from each such author. JoVE reserves the right, in its absolute and sole discretion and without giving any reason therefore, to accept or decline any work submitted to JoVE. JoVE and its employees, agents and independent contractors shall have

ARTICLE AND VIDEO LICENSE AGREEMENT

full, unfettered access to the facilities of the Author or of the Author's institution as necessary to make the Video, whether actually published or not. JoVE has sole discretion as to the method of making and publishing the Materials, including, without limitation, to all decisions regarding editing, lighting, filming, timing of publication, if any, length, quality, content and the like.

11. **Indemnification.** The Author agrees to indemnify JoVE and/or its successors and assigns from and against any and all claims, costs, and expenses, including attorney's fees, arising out of any breach of any warranty or other representations contained herein. The Author further agrees to indemnify and hold harmless JoVE from and against any and all claims, costs, and expenses, including attorney's fees, resulting from the breach by the Author of any representation or warranty contained herein or from allegations or instances of violation of intellectual property rights, damage to the Author's or the Author's institution's facilities, fraud, libel, defamation, research, equipment, experiments, property damage, personal injury, violations of institutional, laboratory, hospital, ethical, human and animal treatment, privacy or other rules, regulations, laws, procedures or guidelines, liabilities and other losses or damages related in any way to the submission of work to JoVE, making of videos by JoVE, or publication in JoVE or elsewhere by JoVE. The Author shall be responsible for, and shall hold JoVE harmless from, damages caused by lack of sterilization, lack of cleanliness or by contamination due to the making of a video by JoVE its employees, agents or independent contractors. All sterilization, cleanliness or decontamination procedures shall be solely the responsibility of the Author and shall be undertaken at the Author's

expense. All indemnifications provided herein shall include JoVE's attorney's fees and costs related to said losses or damages. Such indemnification and holding harmless shall include such losses or damages incurred by, or in connection with, acts or omissions of JoVE, its employees, agents or independent contractors.

12. **Fees.** To cover the cost incurred for publication, JoVE must receive payment before production and publication the Materials. Payment is due in 21 days of invoice. Should the Materials not be published due to an editorial or production decision, these funds will be returned to the Author. Withdrawal by the Author of any submitted Materials after final peer review approval will result in a US\$1,200 fee to cover pre-production expenses incurred by JoVE. If payment is not received by the completion of filming, production and publication of the Materials will be suspended until payment is received.

13. **Transfer, Governing Law.** This Agreement may be assigned by JoVE and shall inure to the benefits of any of JoVE's successors and assignees. This Agreement shall be governed and construed by the internal laws of the Commonwealth of Massachusetts without giving effect to any conflict of law provision thereunder. This Agreement may be executed in counterparts, each of which shall be deemed an original, but all of which together shall be deemed to be one and the same agreement. A signed copy of this Agreement delivered by facsimile, e-mail or other means of electronic transmission shall be deemed to have the same legal effect as delivery of an original signed copy of this Agreement.

A signed copy of this document must be sent with all new submissions. Only one Agreement required per submission.

CORRESPONDING AUTHOR:

Name:

Steven Poelzing

Department:

Virginia Tech Carilion Research Institute and Biomedical Engineering and Mechanics

Institution:

Virginia Tech

Article Title:

Quantifying Intermembrane Distances with Serial Image Dilations in Matlab

Signature:



Date:

4/14/18

Please submit a signed and dated copy of this license by one of the following three methods:

- 1) Upload a scanned copy of the document as a pdf on the JoVE submission site;
- 2) Fax the document to +1.866.381.2236;
- 3) Mail the document to JoVE / Attn: JoVE Editorial / 1 Alewife Center #200 / Cambridge, MA 02139

For questions, please email submissions@jove.com or call +1.617.945.9051

Editorial Comments:

1. Please take this opportunity to thoroughly proofread the manuscript to ensure that there are no spelling or grammar issues.

Complete.

2. Figures: Please include a space between the numbers and their corresponding units (i.e., 50 nm). Please order the figures based on their appearance in the text.

Complete.

3. Figure 2: Please add the panel labels (A-H) in the figure.

Complete.

4. Please remove the embedded Table from the manuscript. All tables should be uploaded separately to your Editorial Manager account in the form of an .xls or .xlsx file.

Complete.

5. Please provide an email address for each author.

Complete.

6. Please revise the Introduction to include all of the following:

a) A clear statement of the overall goal of this method

Lines 34-35

b) The rationale behind the development and/or use of this technique

Lines 37-40

c) The advantages over alternative techniques with applicable references to previous studies

Lines 50-53

d) A description of the context of the technique in the wider body of literature

Lines 60-62

e) Information to help readers to determine whether the method is appropriate for their application

Line 62

7. Please include a space between all numbers and their corresponding units: 15 mL, 37 °C, 60 s; etc.

Complete.

8. Please revise the protocol to contain only action items that direct the reader to do something. The actions should be described in the imperative tense in complete sentences wherever possible. Avoid usage of phrases such as “could be,” “should be,” and “would be” throughout the Protocol. Any text that cannot be written in the imperative tense may be added as a “Note.”

Complete.

9. 3.1, 3.2, 3.3, 3.4, 3.6, 3.7, 3.8, 3.9: Please consider providing software screenshots as supplementary files to match each step.

Added supplemental file S2.

10. Please ensure that the references appear as the following: [Lastname, F.I., LastName, F.I., LastName, F.I. Article Title. Source. Volume (Issue), FirstPage – LastPage (YEAR).] For more than 6 authors, list only the first author then et al.

Complete.

11. References: Please do not abbreviate journal titles. Please include volume and issue numbers for all references.
Complete.

12. Please note that Standard Access is checked in the uploaded ALA, while in the Questionnaire Responses Open Access is selected. Please be consistent.
Corrected.

Reviewer #1:

1) In principle, image processing algorithms should not be sensitive to rotation. This is essential in order to decrease the error coming from the manual intervention of the user and to facilitate the task of image analysis. Thus, I praise the authors for having evaluated the effect of rotating the analyzed images, because ideally, the computed perinexal space width should remain the same.

As correctly observed by the authors, the strong dependence on rotation is an artefact of the dilation procedure due to the small size (3x3 pixels) of the used structural elements (dilation kernel shapes). The authors proposed a formula (line 248) to compensate for this effect. However, a motivation and a rigorous validation of this formula are missing. What is the rationale for this formula? Is it empirical or does it have some mathematical foundation? It would be desirable (e.g., in Fig. 5) to validate this formula (and its accuracy) by drawing parallel lines with a known separating distance and analyzing the image upon different rotations, rather than by processing an electron microscope image of an irregularly shaped perinexus as done in Fig. 5.

Authors: We appreciate the reviewer's recognition of our efforts and constructive feedback on the rotation artifact correction. In the process of preparing the requested figures, we noticed an error in our formula, which, though empirically derived and validated, only functioned properly when applied to images of a certain spatial resolution. A full explanation of the new formula has been provided on lines 260-284 and Figure 8 has been updated as requested.

R1: 2) Morphological operations are very sensitive to contrast, blurred edges and to the manner images are preprocessed or recorded. This implies that if the preprocessing of the microscopy images is not standardized, false detection (in this case the manual outlining of the two membranes) may occur. The choice of the structure element (dilation kernel shape) might also depend on the contrast of the image. This should be assessed by artificially blurring the images or altering their contrast. This aspect is important because the membrane must be accurately outlined by the user.

Authors: The reviewer astutely identifies a key challenge with our method in that the original outline is user-generated. We have included clarification of gap junction and perinexus identification in the Protocol Section 2. We recognize that a limitation of the program is the reliance on the observer accurately identifying the relevant structure and a desirable and natural next step is to remove the human input and solve challenges including edge sharpness, contrast and signal-to-noise ratio as the reviewer has noted. In its current state, the described method is robust enough to identify relative differences between groups, even if absolute values are observer-dependent, as seen previously (reference 6).

R1: 3) A similar comment applies to the spatial resolution of the images. Would the algorithm give the same result if the images are taken at a higher or at a lower resolution? This should be ascertained by

analyzing resampled images (up- and down-sampled), or, better, by analyzing microscopy images acquired at different magnifications.

Authors: The reviewer raises an intriguing question and we have included an additional low-resolution supplemental image (S6) and a brief addition to the discussion section, lines 440-442, to address differences in spatial resolution. The phantoms included in Figure 8 should also provide confidence that the results are valid for any spatial resolution, as the figures and supplement together span at least two orders of magnitude of potential spatial resolutions.

R1: 4) The algorithm presupposes that the section plane is perpendicular to the two membranes. How was this condition guaranteed? Was the section angle measured? The measured width will be overestimated if the section and membrane planes deviate from being perpendicular. If α denotes the angle of the deviation from perpendicularity, the measured width will be overestimated by a factor $1/\cos(\alpha)$. For $\alpha = 30$ degrees, the width will be overestimated by 15% which is already substantial; for a very oblique section with $\alpha = 60$ degrees, the width will be severely overestimated by a factor 2.

Authors: We appreciate the reviewer's concern, as this is one of our greatest challenges with acquiring electron micrographs. We used the measurement of connexin gap junctions (GJW on page 7) to confirm that our sections are generally perpendicular to the structures we measure. Had they been substantially out of plane, we would have significantly overestimated their widths, as the reviewer noted. Still, it is difficult to say definitively that complex, and wider perinexal structures will stay in-plane even over the course of 200nm, and it is therefore critical that sufficiently large sample sizes are collected and that results are interpreted with a degree of caution. We would like to emphasize that perinexal values should not be interpreted to reflect in vivo spaces, but that our approach measures mean differences in perinexal width relative to some intervention. These points have been articulated in the discussion on lines 460-467.

R1: 5) If I understand correctly, the "centerline" is the locus of points for which the (ideally Euclidean) distance from the two membranes is equal. Assume P a point on the centerline and call A and B the closest points located on the respective membranes. Then, the distances PA and PB are equal, and the algorithm will return PA+PB as a result. However, if the two membranes are (locally) not exactly parallel, the points A, P and B will not be aligned, and the distance between A and B will be smaller than PA+PB because of the triangle inequality. This may lead to a further overestimation of the width of the intercellular space.

Authors: We appreciate the reviewer's thorough analysis of our methodology. Of course one of the limitations of this algorithm is that as the membranes become less-parallel, it may over- or – underestimate the distance between them. However, due to the high spatial sampling frequency, small local variations have not been shown to affect the overall measurement and any differences resulting from such occurrences are smaller than our threshold for detecting differences between experimental groups. As we demonstrated in our published study using the manual technique (Reference 6), individual observers may measure different absolute values, but relative differences will still be detected.

Reviewer #2:

It is a technical report, but it is way too long and very hard to follow. It can be simplified much further.

Authors: We thank the reviewer for noting that the verbal description of the algorithm is long, complex, and at time tedious. In accordance with the JOVE vision, the written document should serve as a highly detailed source to explain concepts that were not clearly conveyed in the video, which for many users will be the first interaction with the material.

Reviewer #3:

One of few minor issues is that this Matlab-based pixel dilation method has been previously used for defining and calculating area/distance/border in biological images to achieve high precision and efficiency in image quantification in several publications (i.e. Sild et al. Neural Plast. 2013:853727; Yan et al. PLoS One. 2014, 8;9(8):e104357, and Papari et al. IEEE Trans Image Process. 2008 Oct; 17(10): 1950-62). This reviewer highly encourages the authors to cite these previous publications.

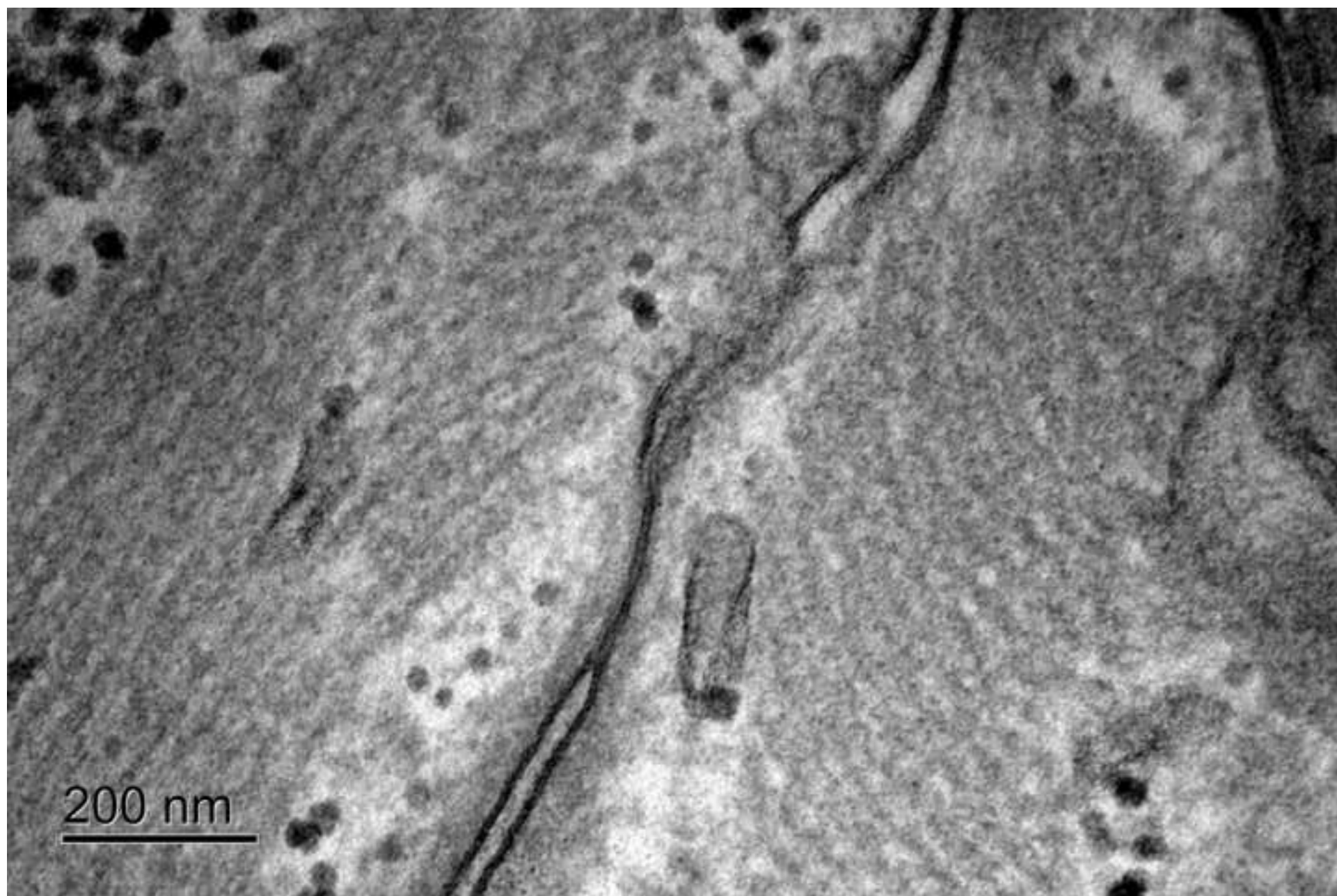
Authors: We appreciate the reviewer bringing these intriguing studies to our attention. However, we still have not found any methodology that utilizes serial image dilations to count the pixels between opposing edges. We do use a secondary dilation similar to Sild *et al.* to close gaps in our final image, and that citation has been included in the discussion. The other citations have been included in the introduction (Line 45) as they utilize image dilations for contour/edge detection but not in this particular application.

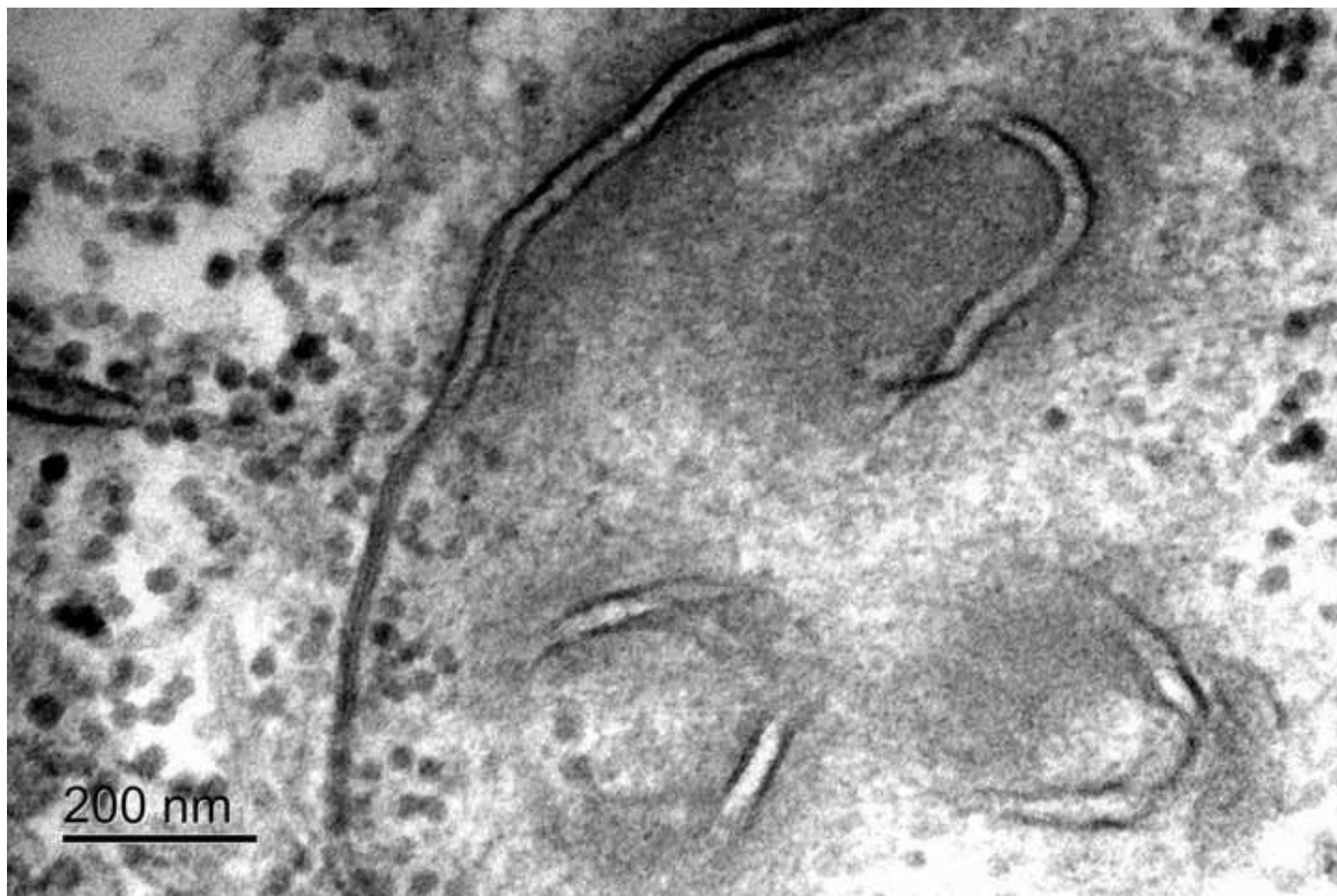
R3: Also, please provide some details about how to use morphological landmarks to identify perinexus and gap junction.

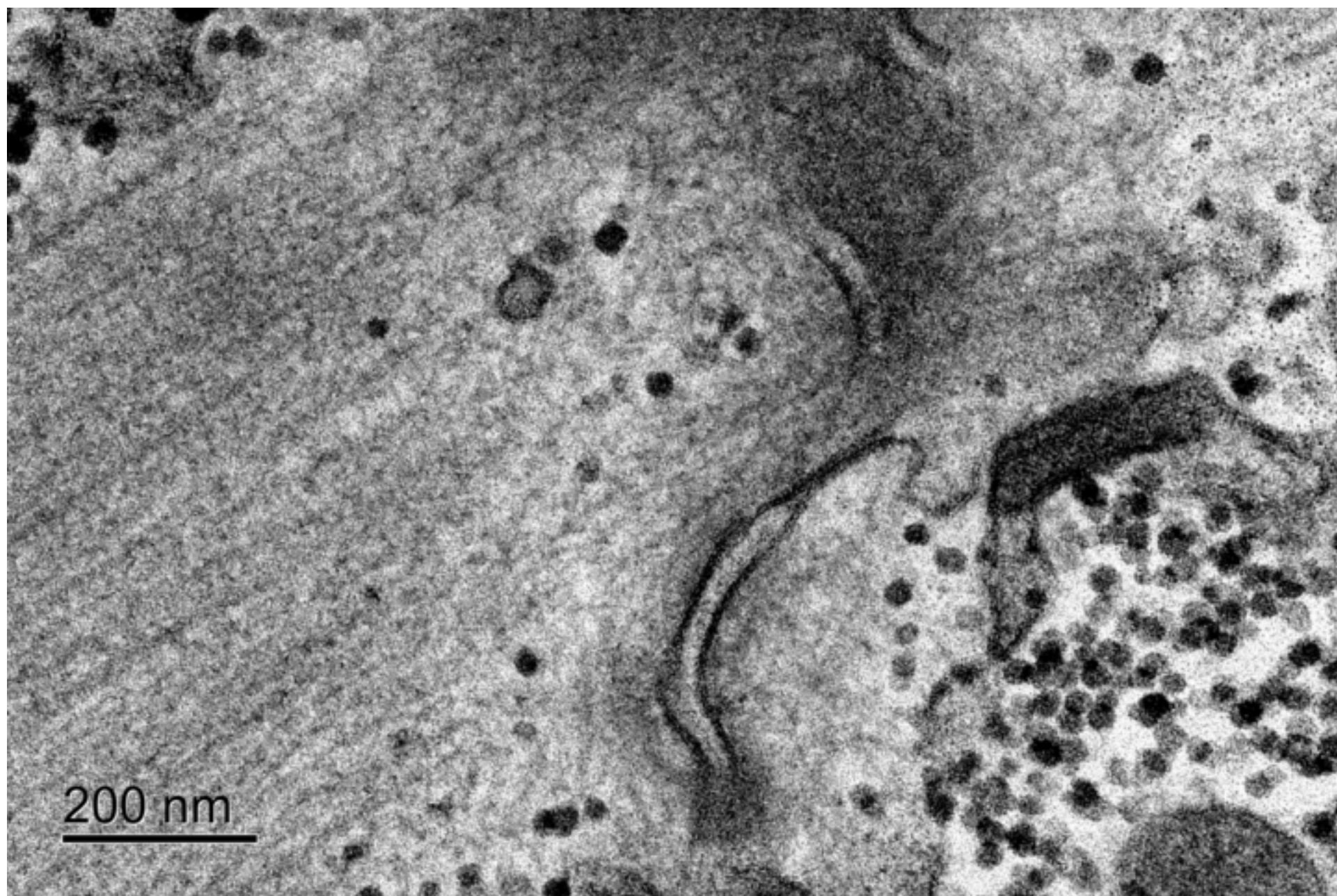
Authors: We appreciate the reviewer's suggestion and have clarified the identification of the perinexus and gap junction in the Protocol Section 2.

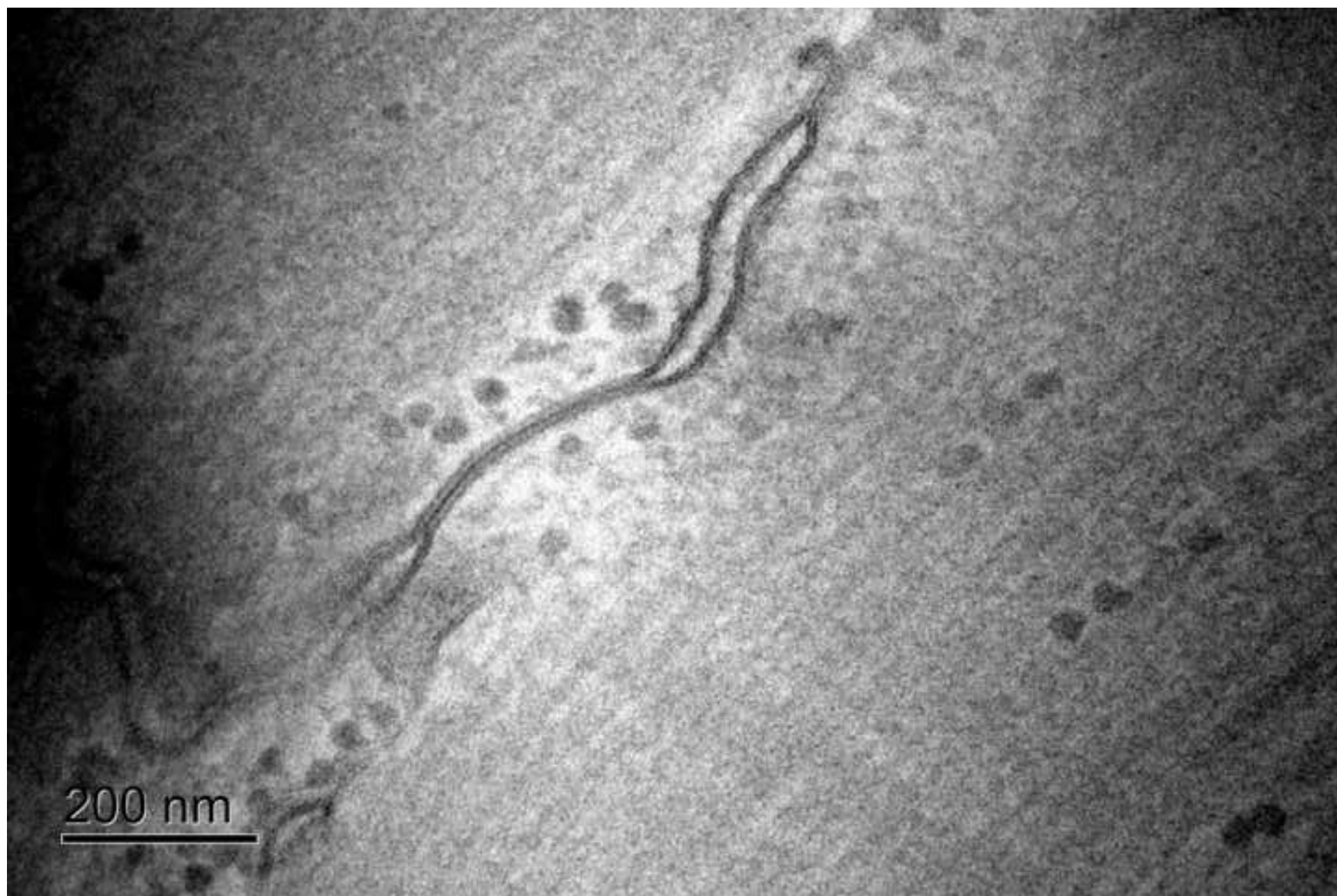
R3: In addition, geometrically-diverse perinexi do appear in TEM images, such as the one in Fig 9C. Please provide an example to demonstrate the pixel dilation step-by-step for those perinexi with complicated morphology.

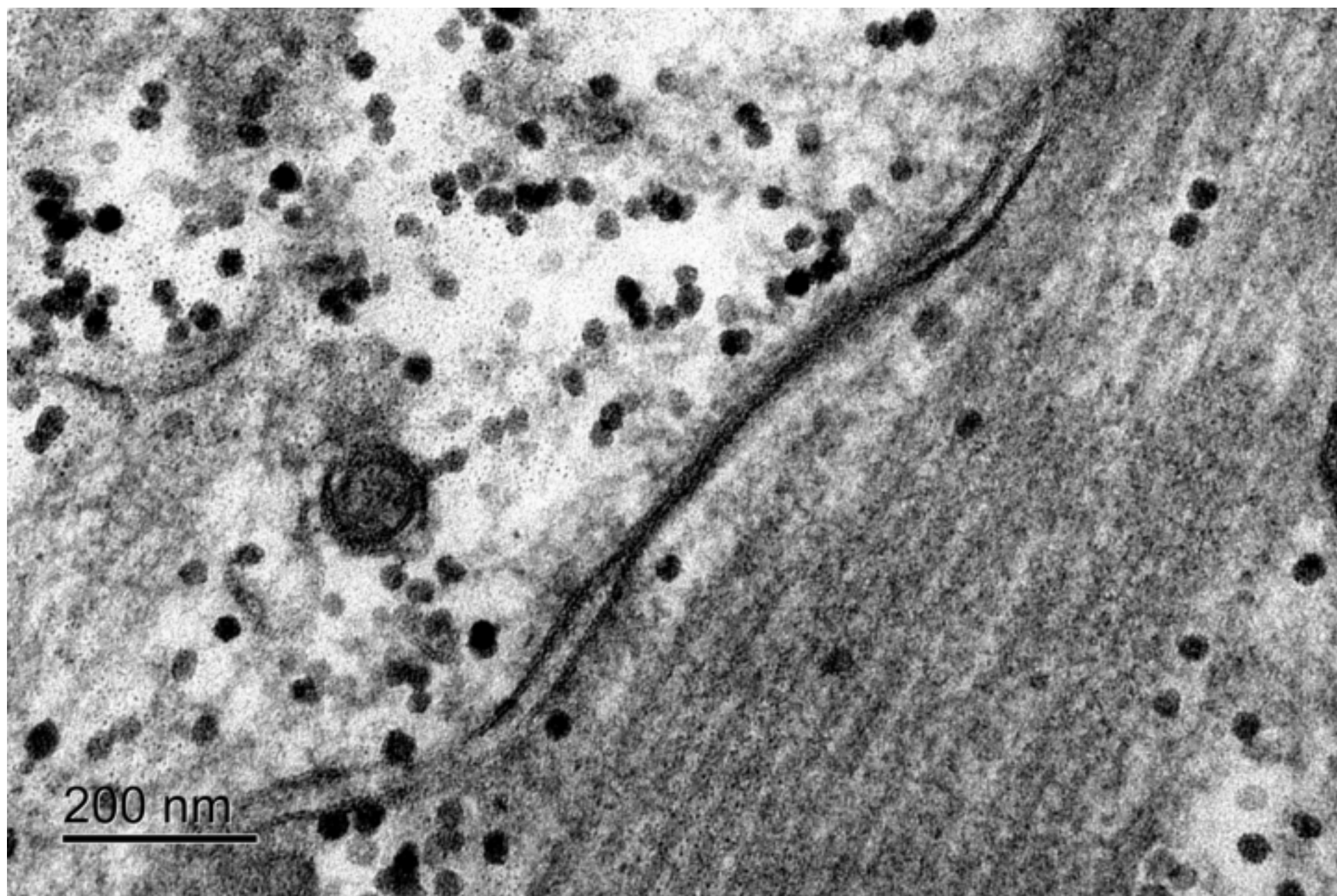
Authors: We agree the inclusion of dilation steps for more irregularly-shaped perinexi could be useful for the reader. For the sake of conciseness we have included a second example in the supplement S3 but defer to the reviewer if they would prefer additional examples.

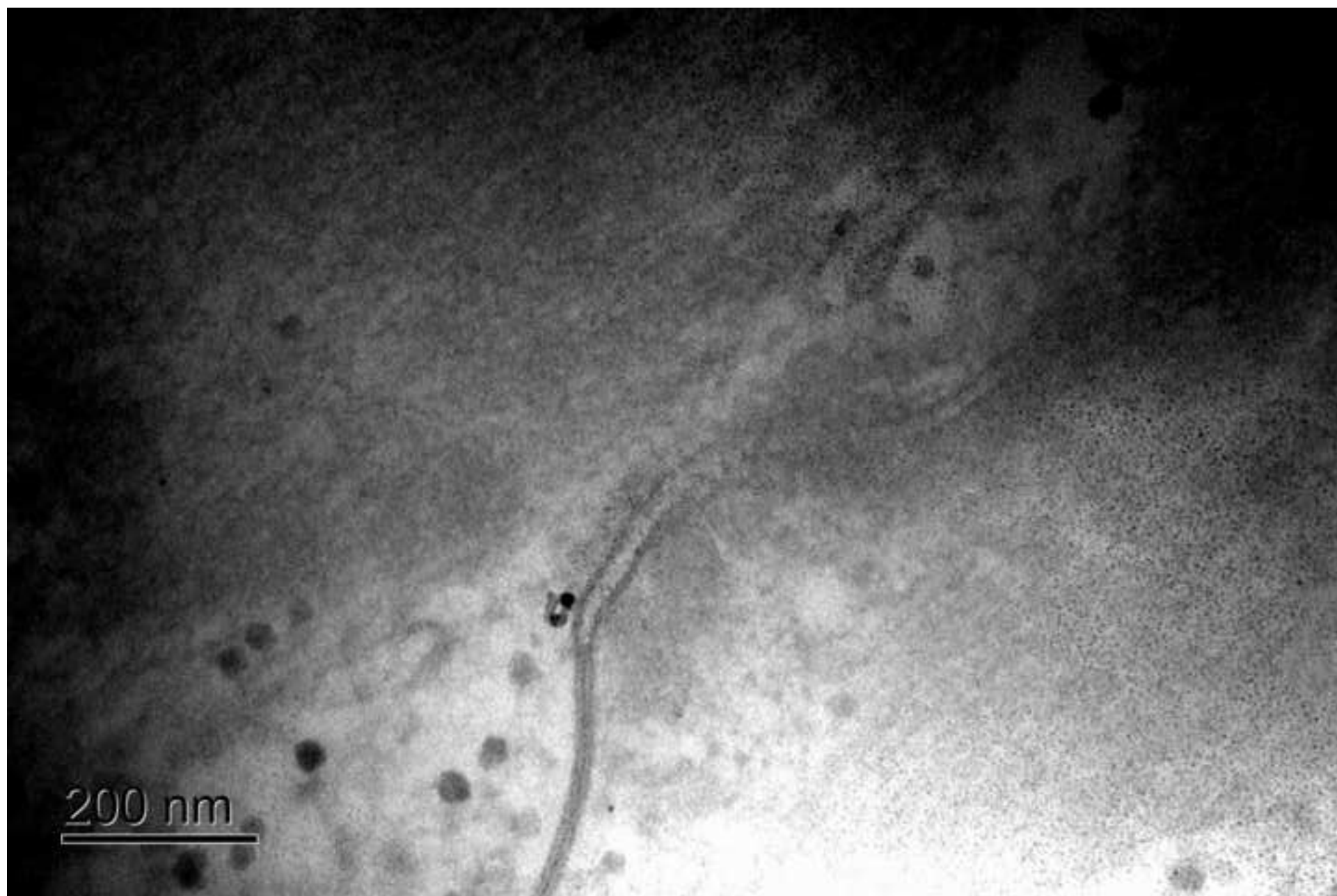


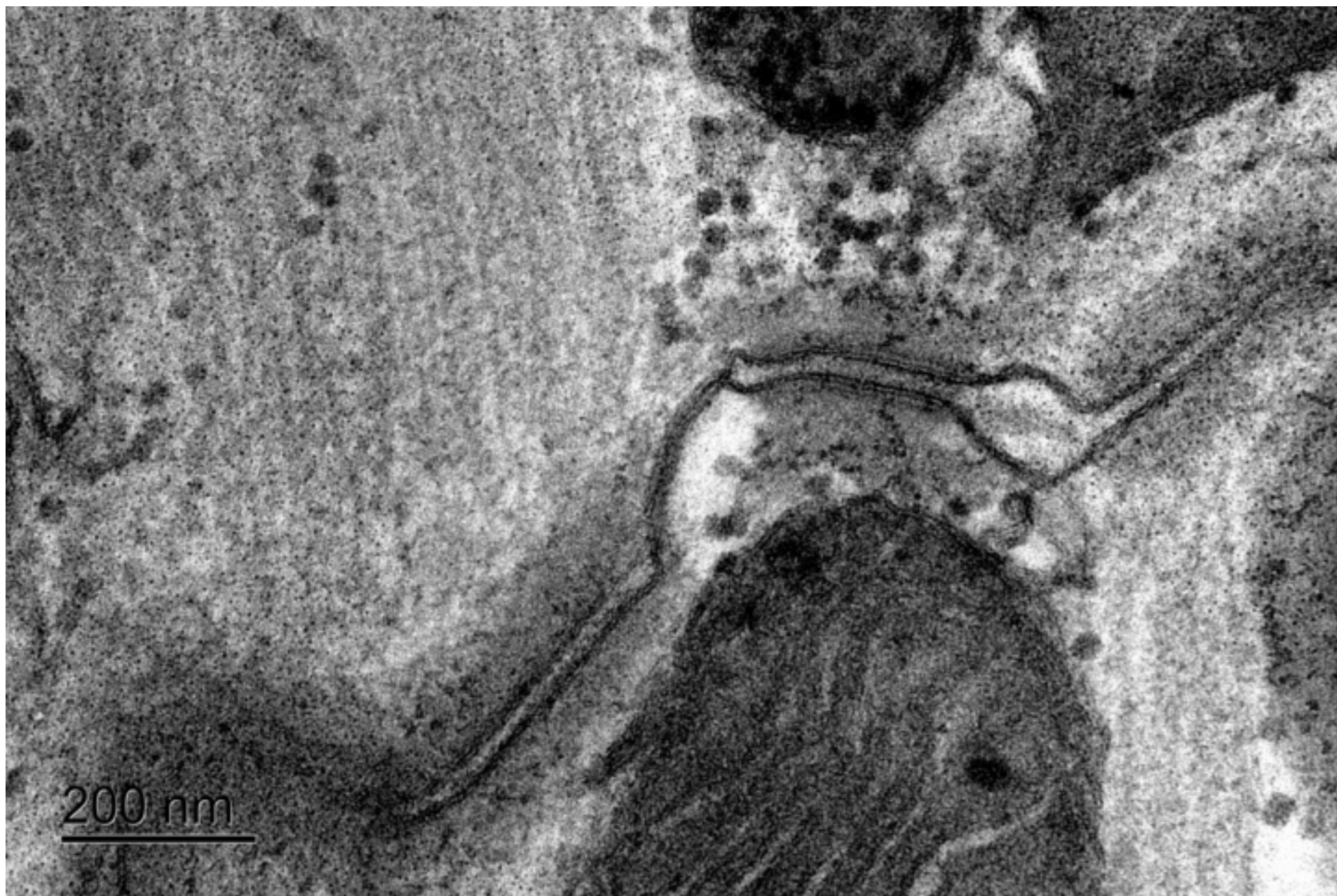




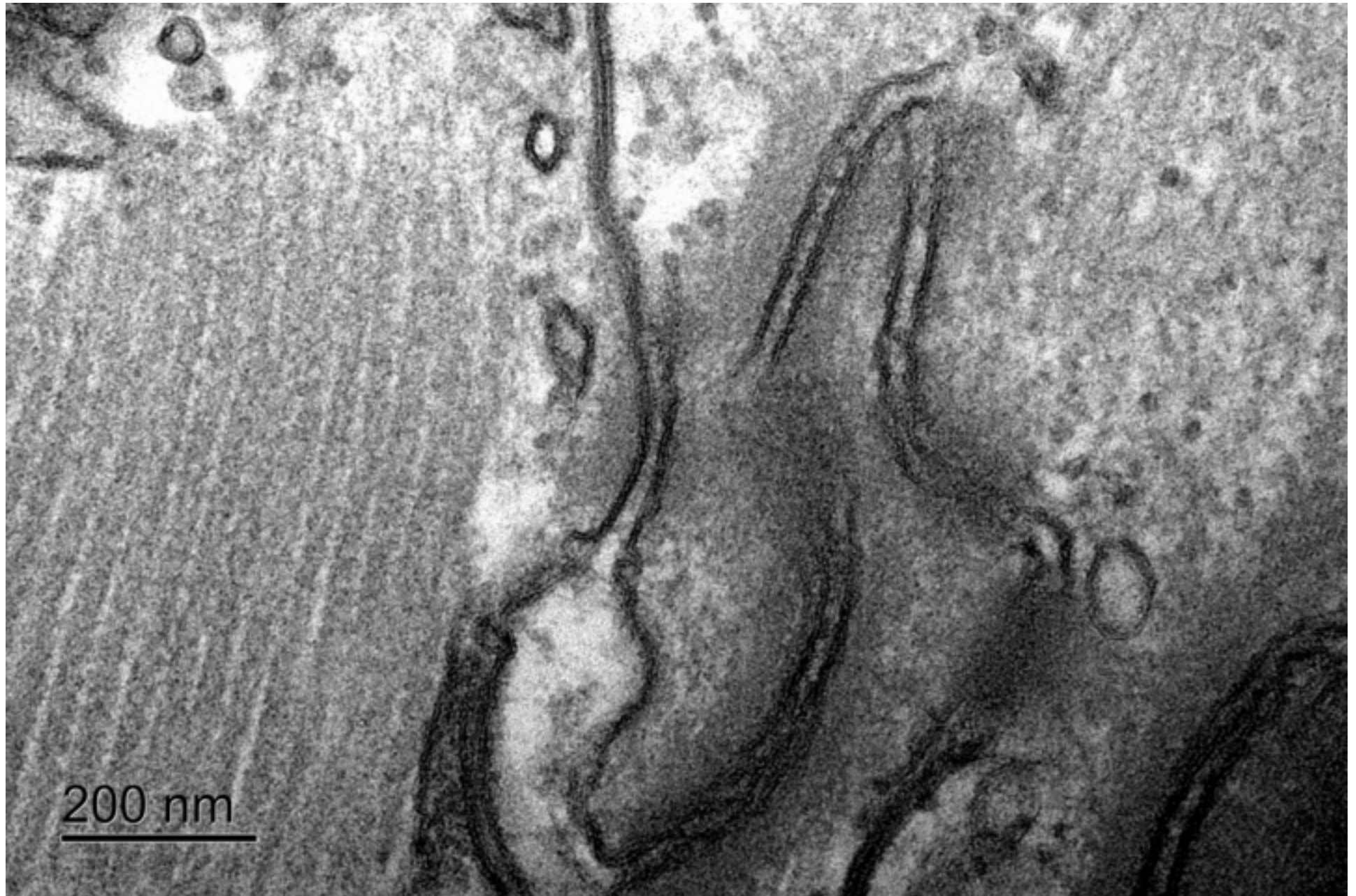


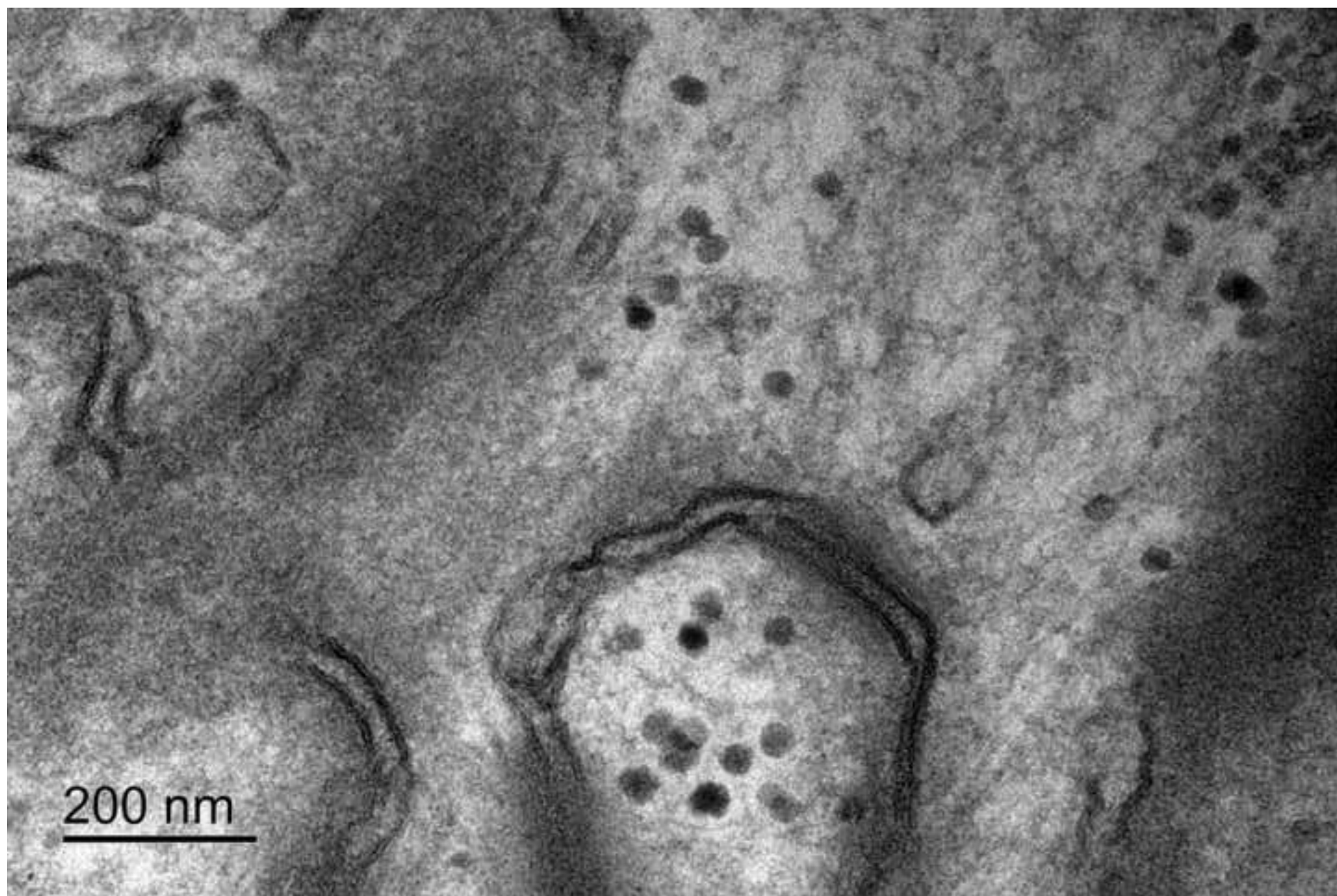


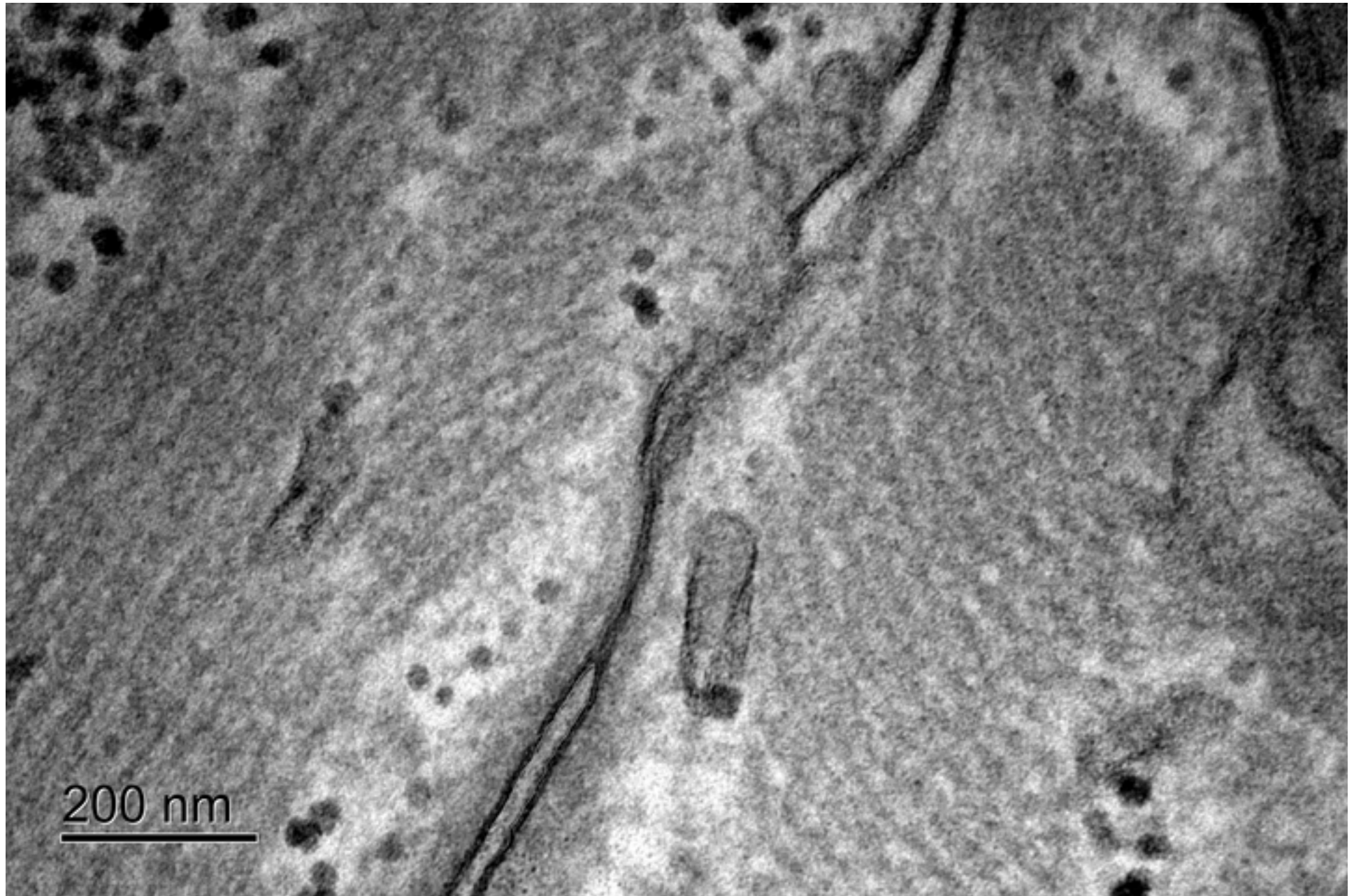


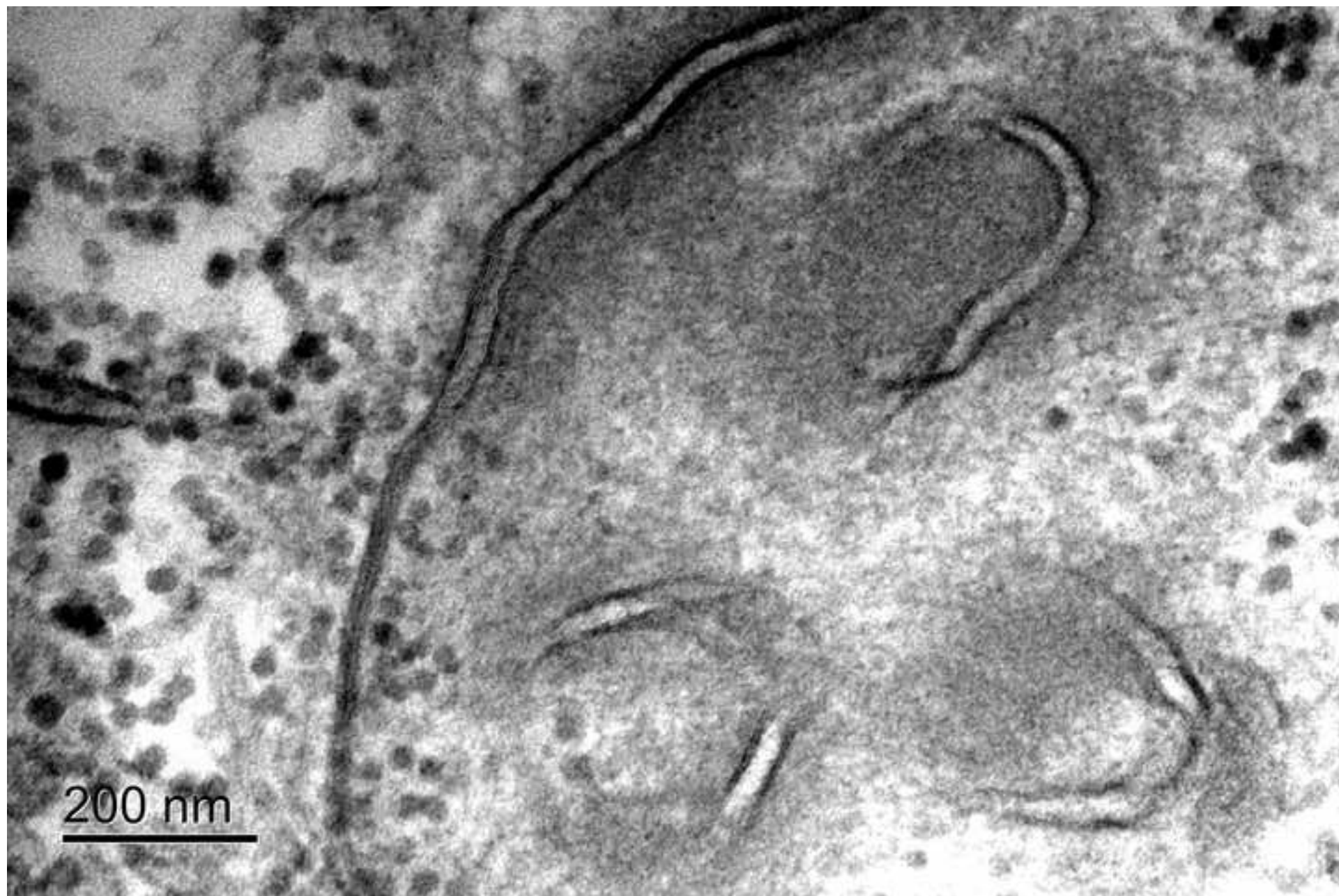


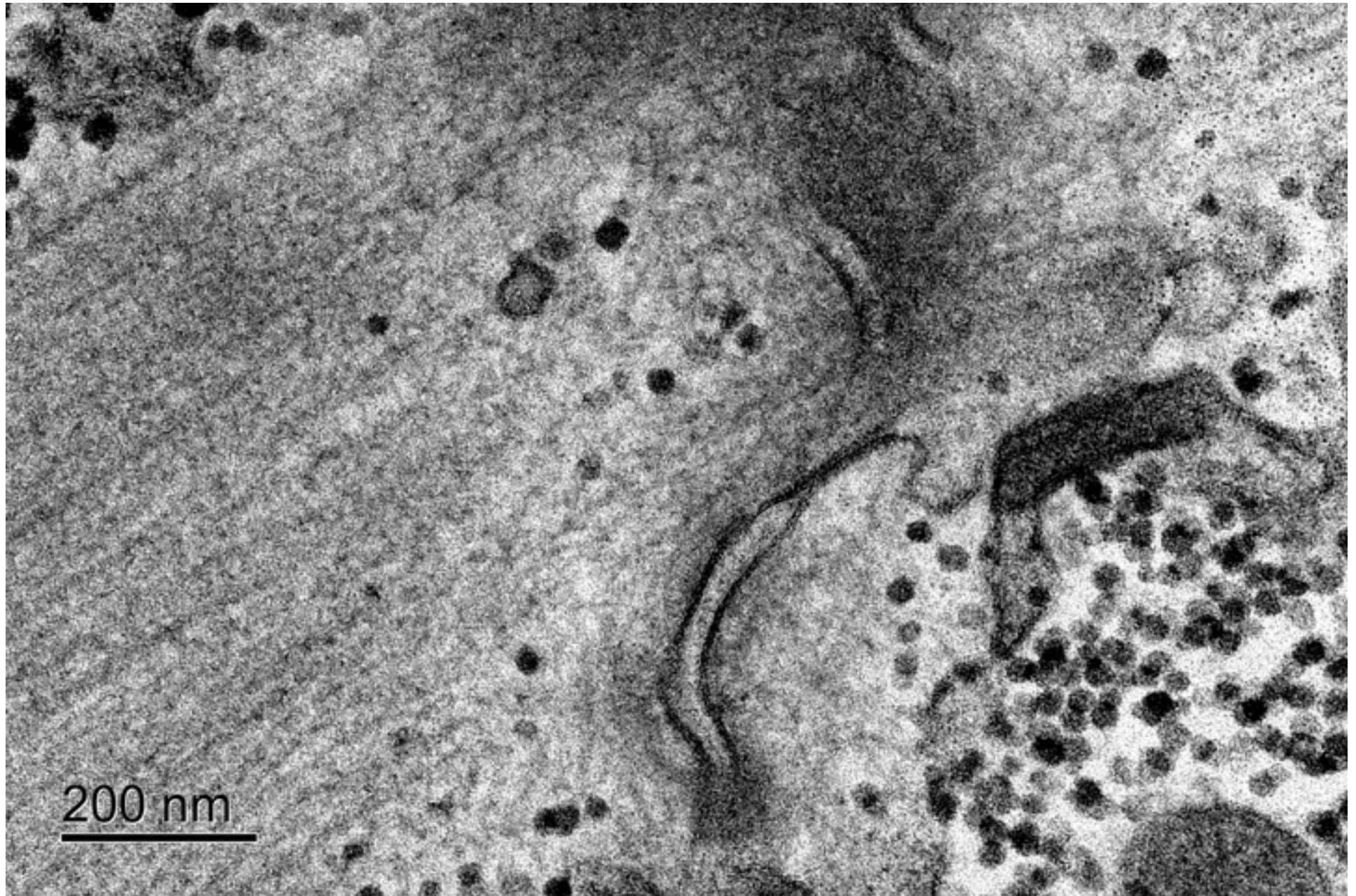


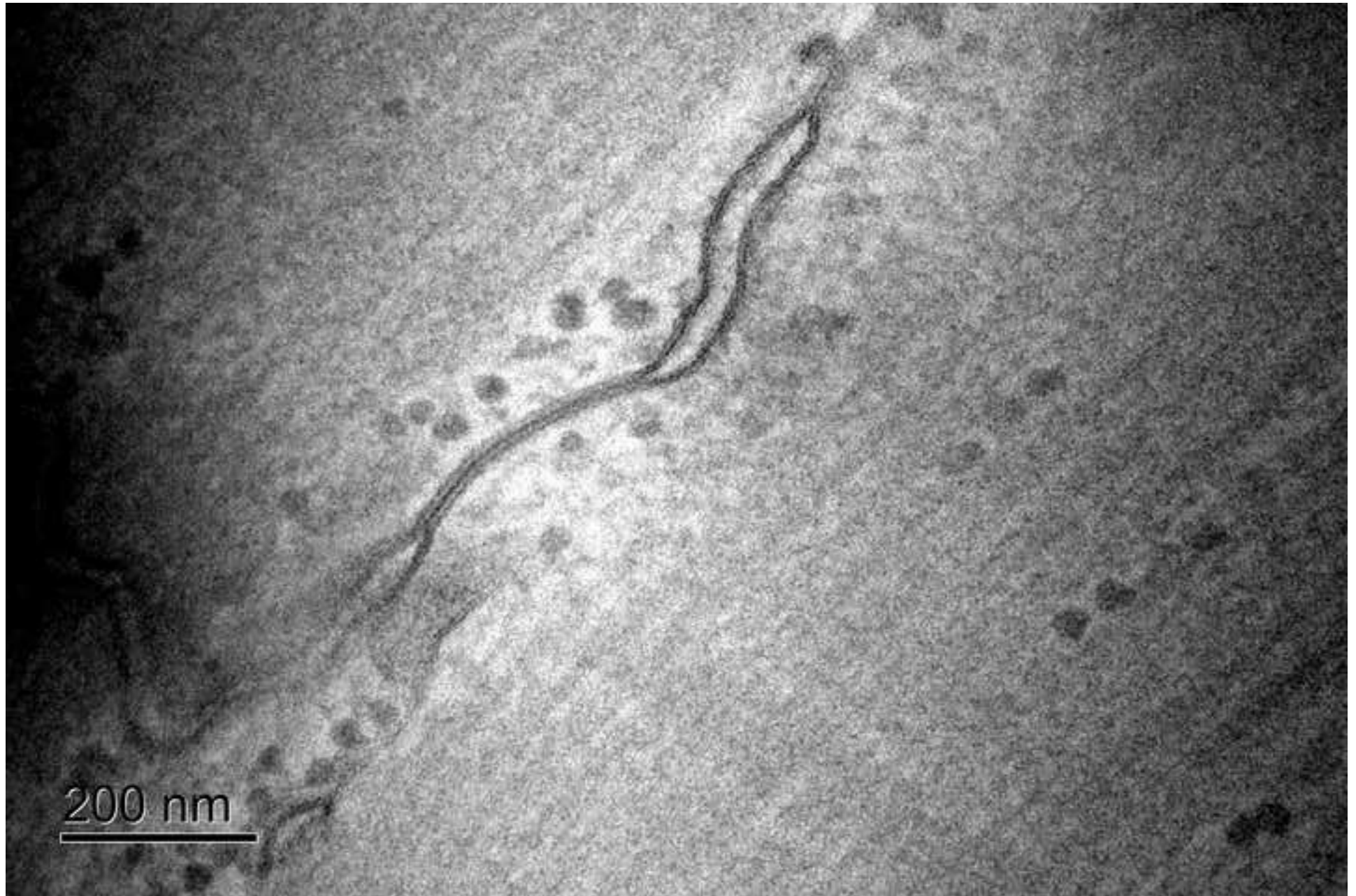


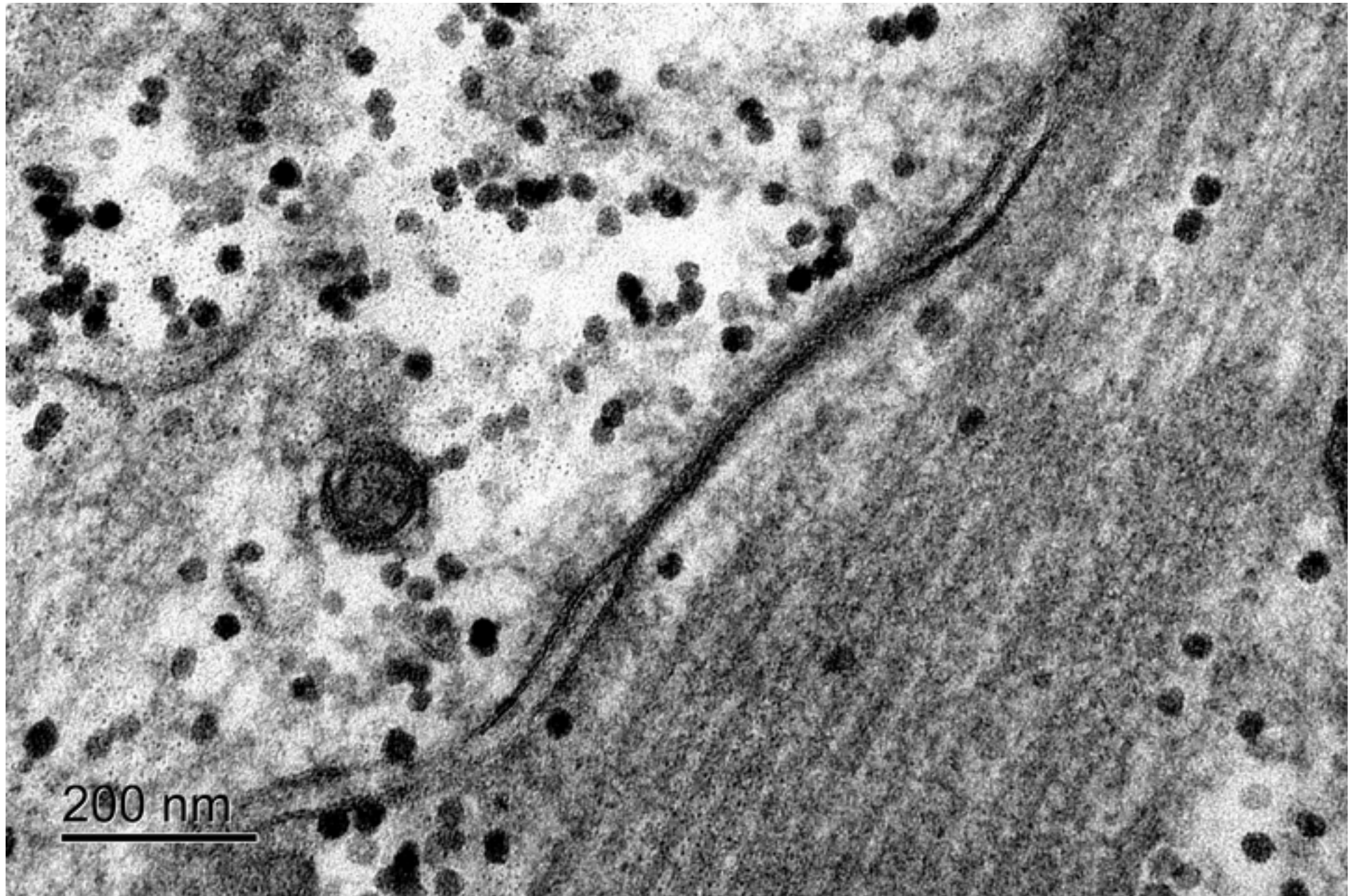


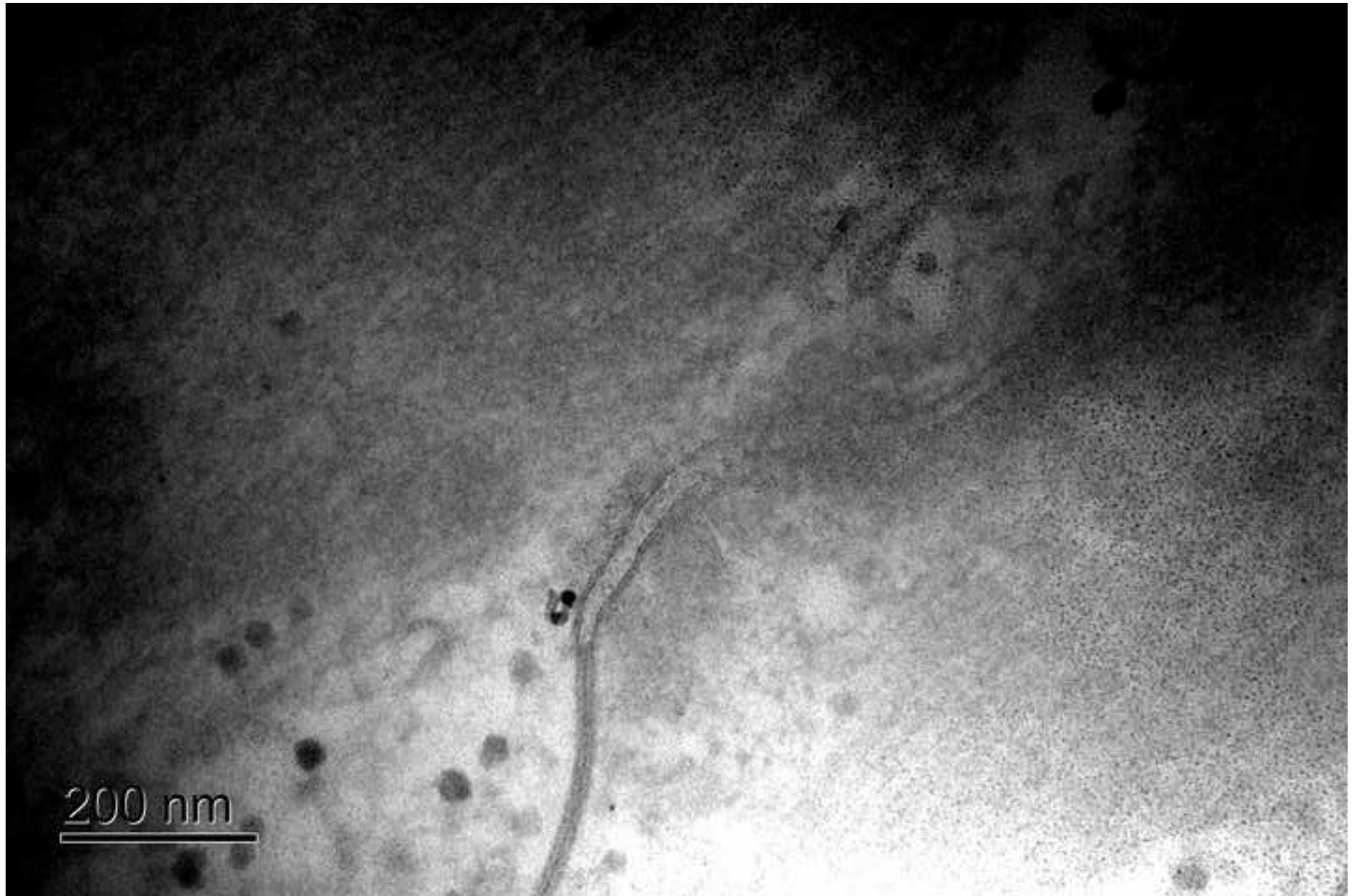


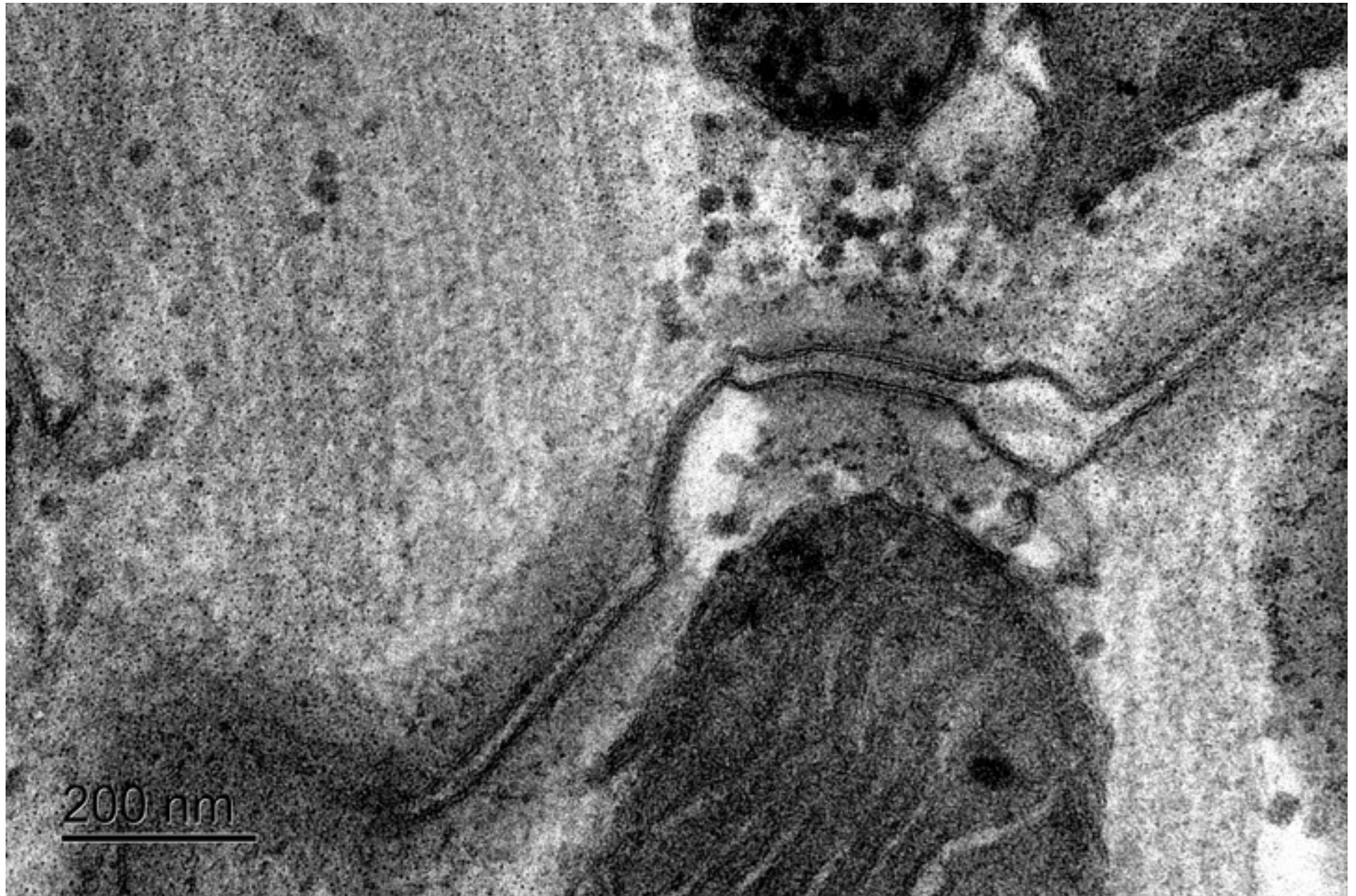


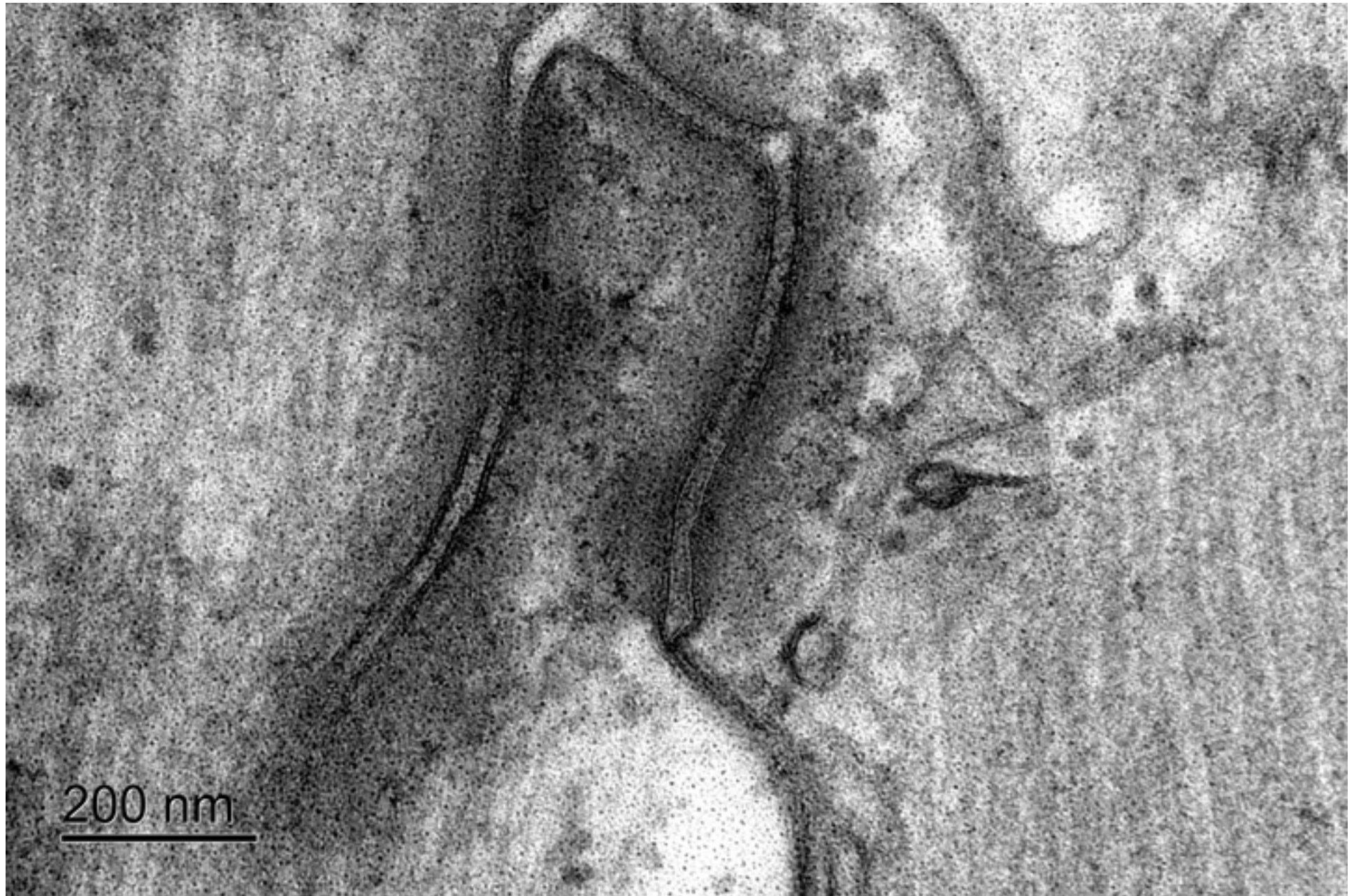


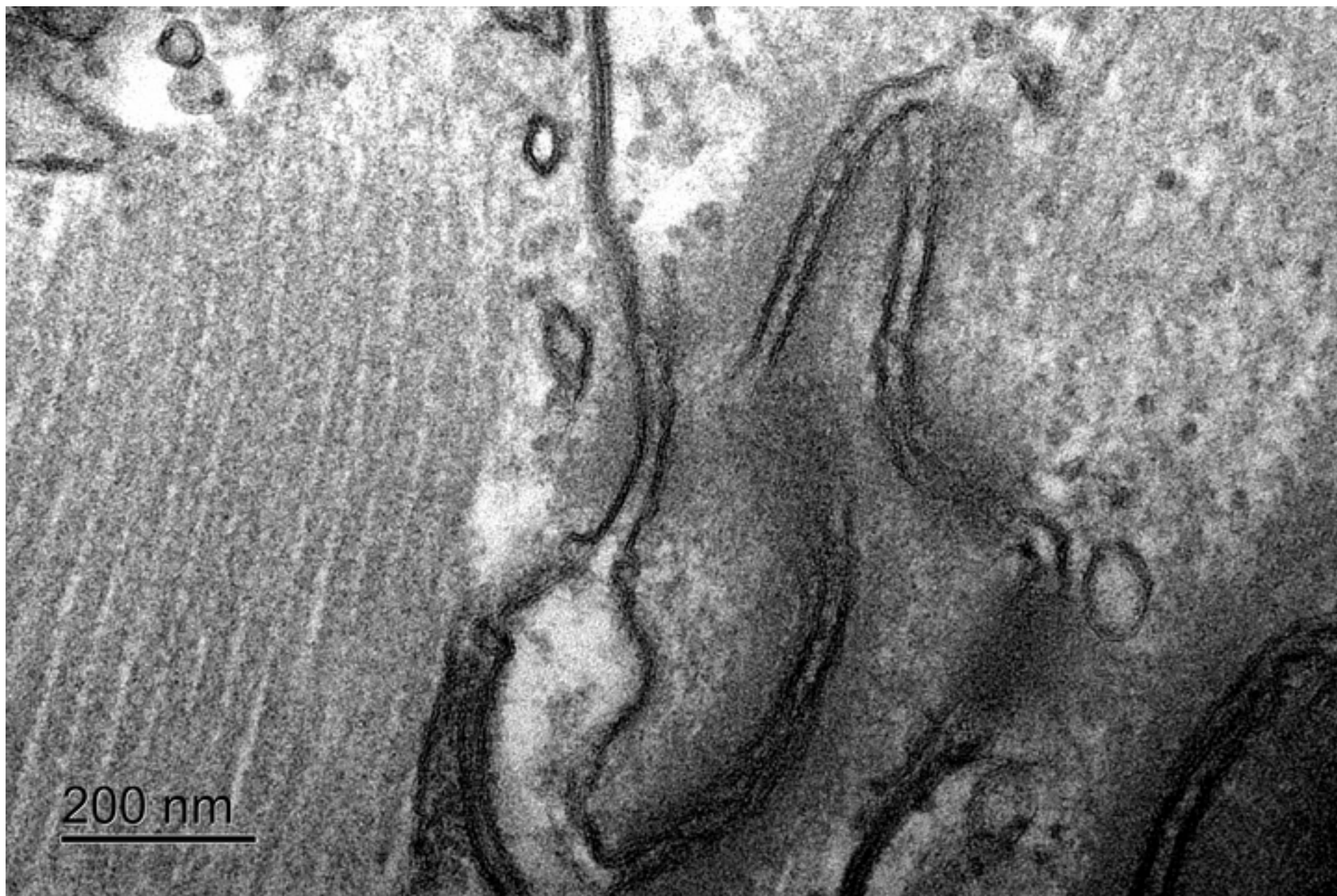


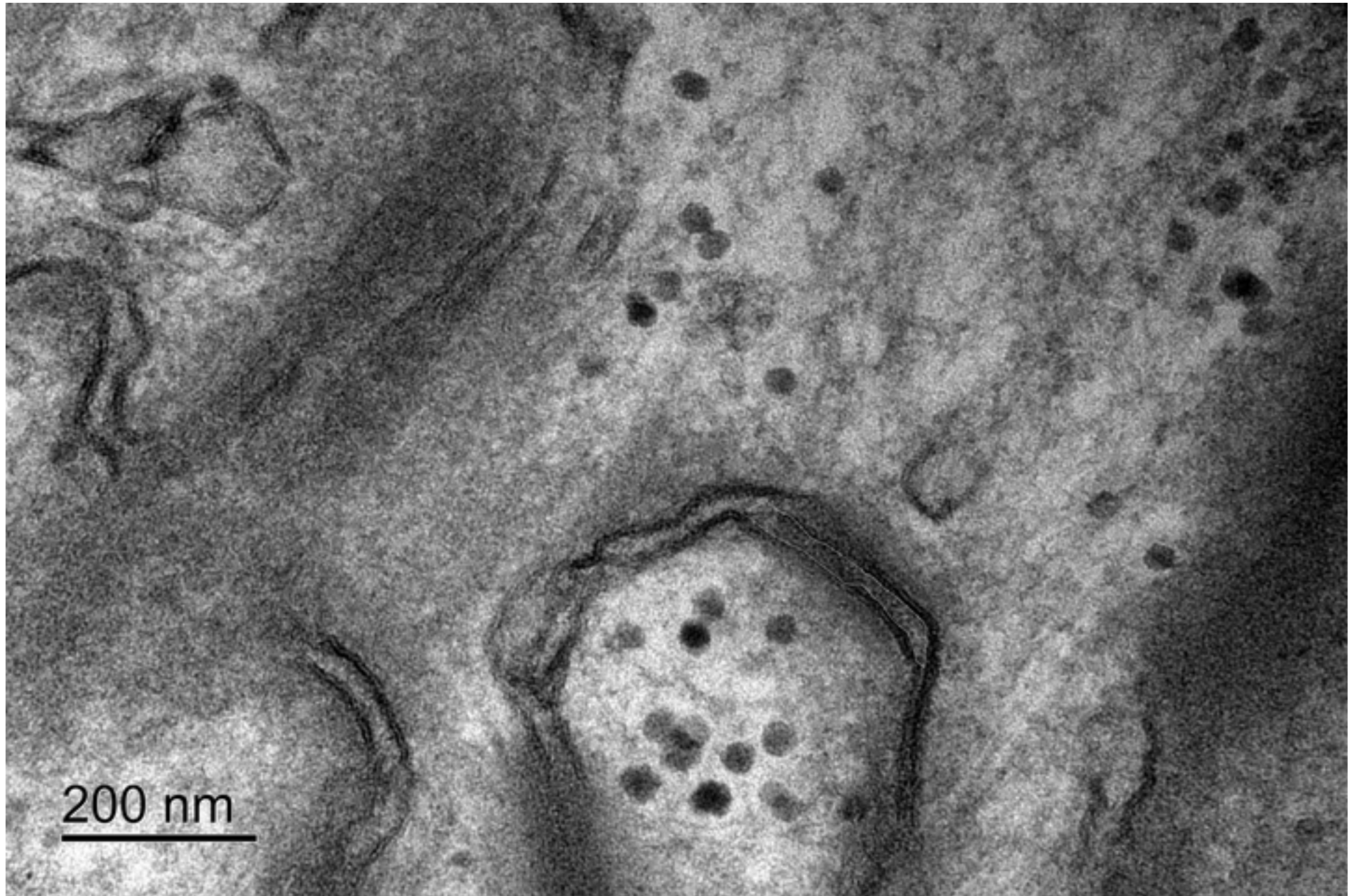












MembraneSepDist Training Set Readme

The raw images must be processed first using the ImageSub m-file in folder S2. Then the processed images can be analyzed using the MembraneSepDist m-file.

The images in the Outlined folder have been outlined by an experienced user and are provided for reference. Note how the *inner* membrane is carefully followed. It is also perfectly acceptable to outline further from the gap junction, as the end of the perinexal outline will be cropped out in later processing steps.

The measurements of the outlined images are provided in the attached Excel file. It is strongly recommended that a new user be able to produce measurements that closely match (within ~1nm) the experienced user's measurements in the training file before moving on to analyzing new data.

File	Wp (0-150)	Wp(35-105)
A	17.22	19.32
B	18.08	19.75
C	20.19	24.04
D	19.55	22.78
E	18.67	20.36
F	13.26	15.25
G	15.85	14.98
H	17.53	19.11
I	15.72	17.65
J	13.38	15.36

```
39 %% Save Data Files
40 %If you want to save the data in a mat file, copy and past the following
41 %line into the command window and save it. Then uncomment the next load
42 %line (line 38).
43 %WpData = [cellstr(filename ), cellstr( Ave150 ), cellstr( AveROI ), cellstr( Total Elapsed Time ), cellstr( User Input Time)];
44 % load WpData %Load data file for storing Wp and time data
45
46 % Set the directory to save the list of Wp by distance from GJ edge
47 - savefile = ['',file_name, '.mat'];
48
49 %% Figure Save Locations
50 - savestringDC = ['',file_name]; %Directory for final working image figure:
51 - file_name1 = [file_name, 'A'];
52 - savestringOCL = ['',file_name1]; %Directory for original image w/ centerline overlay:
53 - savestringWPMP = ['',file_name]; %Directory for Wp/distance-from-GJ plot:
416 % save(savefile, 'WpList')
417 %
418 %
419 % % If you are using the WpData file from the top of the code, uncomment the
420 % %following lines to save relevant data and figures.
421 %
422 % %Save data - [File name, 0-150nm Wp, ROIWp, total time, user input time]
423 % % WpData = [WpData;cellstr(file_name), num2cell(Ave150), num2cell(aveROI), num2cell(eltime), num2cell(userinputtime)];
424 % % save ('WpData','WpData');
425 % % %Save final working image figure
426 % % savestringDC = ['',file_name]; %Insert save location
427 % saveas(figure(6),savestringDC)
428 % % %Save original image w/ centerline overlay
429 % % savestringOCL = ['',file_name]; %Insert save location
430 % saveas(figure(7),savestringOCL)
431 % % %Save Wp/distance from GJ plot
432 % % savestringWPMP = ['',file_name]; %Insert save location
433 % saveas(figure(9),savestringWPMP)
```

3.3

```
8 %% Set Parameters
9 % The following are the default parameters. The user will adjust if
10 % desired in the input box (Line 19)
11 - GthreshDef = 4.5; %Default hreshold to isolate outline and centerline. Typically between 5 and 8. Higher threshold leads to m
12 - scaleDef = 2.912; %Default scale in pixels/nm (200nm scale bar, VetMed scope)
13 - ROIminDef = 30; %Identify Region of Interest (30-105nm is standard for perinexus, 10-90 standard for gap junction width)
14 - ROImaxDef = 105;
```

3.4

```
6 %% Set File Select Location
7 - selected_file = ('');
```

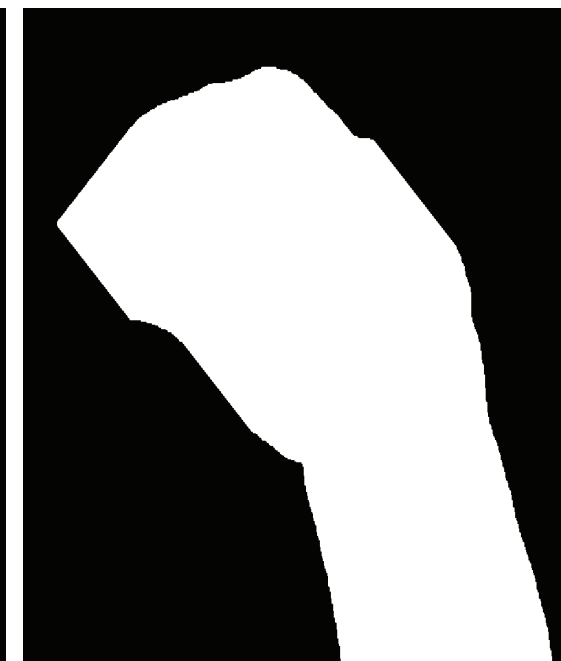
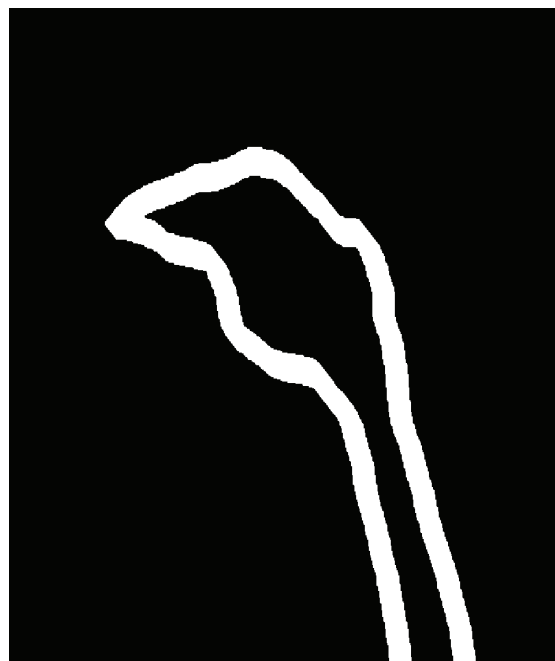
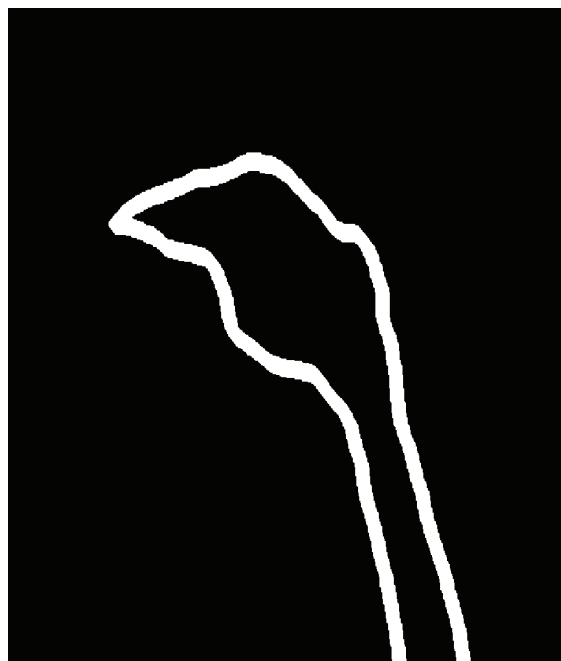

Dilation 3

Dilation 9

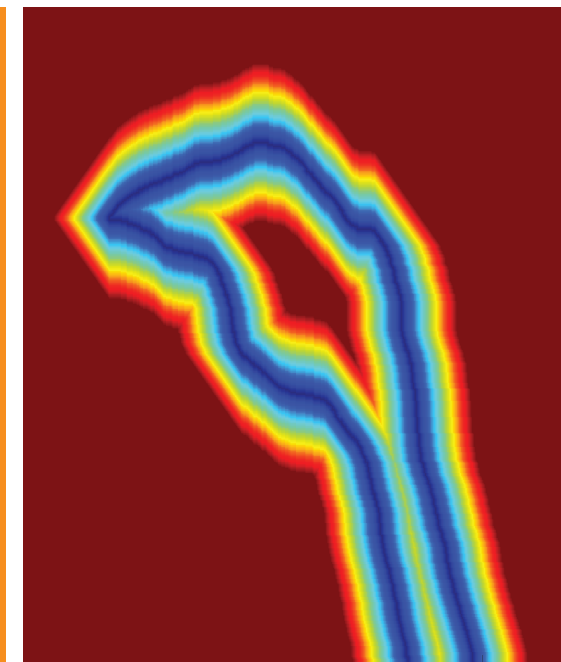
Dilation 35

Dilation 60

Binary

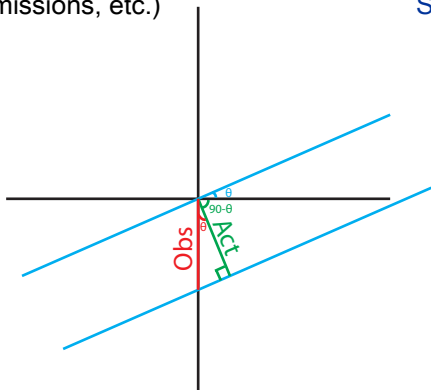


Working



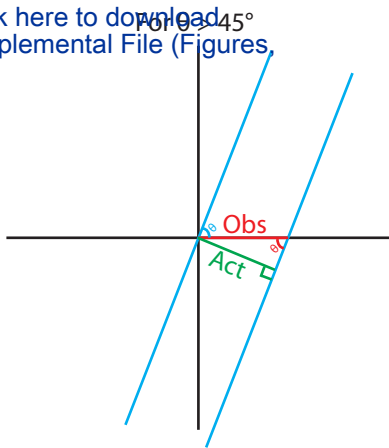
60
50
40
30
20
10
0

Dilations



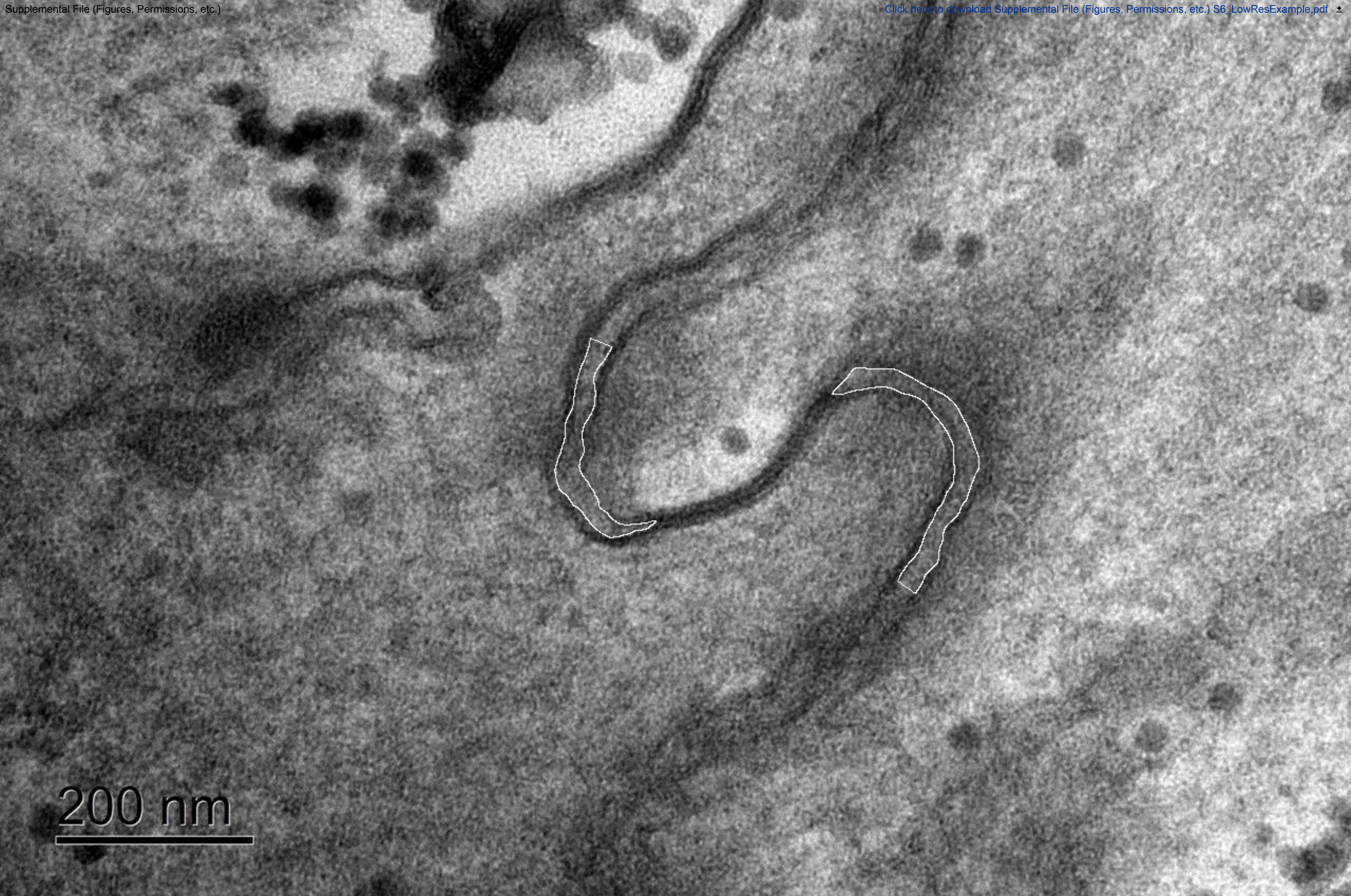
$$\cos(\theta) = \frac{\text{Act}}{\text{Obs}}$$

$$\text{Act} = \text{Obs} * \cos(\theta)$$




$$\sin(\theta) = \frac{\text{Act}}{\text{Obs}}$$

$$\text{Act} = \text{Obs} * \sin(\theta)$$

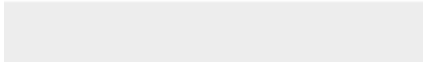



200 nm

The scale of this image is 0.928 pixels/nm, roughly 3 times lower-resolution than the other TEM images analyzed in this study. The calculated widths for the two perinexi shown are 21.84 nm and 14.23 nm. Both values are similar to manual measurements of the same perinexi and to measurements of other perinexi from the same tissue sample.

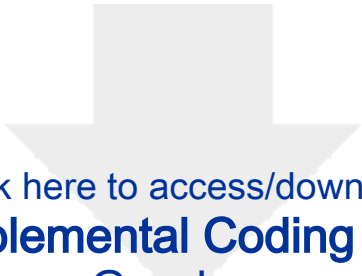


Click here to access/download
Supplemental Coding Files
AutoGraph.m

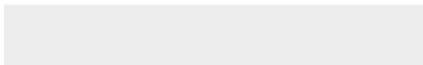
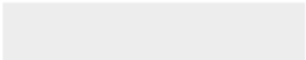





Click here to access/download
Supplemental Coding Files
Edge.m

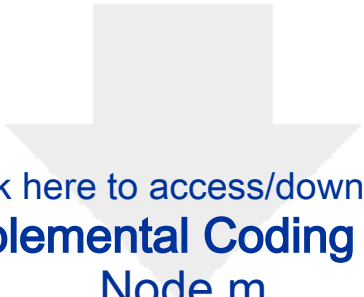


Click here to access/download
Supplemental Coding Files
Graph.m

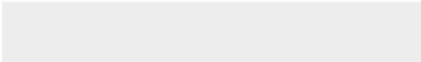





Click here to access/download
Supplemental Coding Files
ImageSub.m



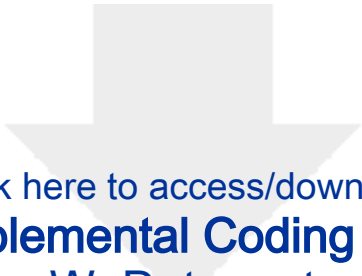
Click here to access/download
Supplemental Coding Files
Node.m



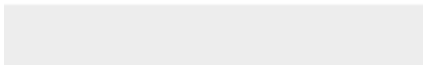
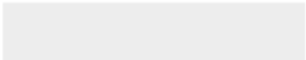


Click here to access/download
Supplemental Coding Files
Pathfinding.m





Click here to access/download
Supplemental Coding Files
WpData.mat





Click here to access/download
Supplemental Coding Files
MembraneSepDist.m.m

